GEOLOGY, MORPHOLOGY AND ACOUSTIC SIDESCAN (SeaMARC II) CHARACTERISTICS OF PACIFIC SEAMOUNTS: ORIGIN AND EVOLUTION OF LANDFORMS AND REMOTE SENSING GROUND TRUTH

A THESIS SUBMITTED TO THE GRADUATE DIVISION OF THE UNIVERSITY OF HAWAII IN PARTIAL FULFILLMENT OF THE REQUIREMENTS FOR THE DEGREE OF

MASTER OF SCIENCE

IN GEOLOGY AND GEOPHYSICS

MAY 1992

By

Wendy Celeste Zayac

Thesis Committee:

Rodey Batiza, Chairman
Alexander Malahoff
Alexander Shor
Thomas B. Reed IV

We certify that we have read this thesis and that, in our opinion, it is satisfactory in scope and quality as a thesis for the degree of Master of Science in Geology and Geophysics.

THESIS COMMITTEE

Chairman

DEDICATION

This thesis is dedicated to

Christopher John Bellaire Zayac

The memory of my brother, Chris, was the source of my strength and persistence in completing my degree after having been ready to give up. He was gifted with a sharp and surprising wit that could turn my blackest mood into a laughing fit, and I would instantly feel better. He helped me learn some important lessons of life: that things are never quite as bad as they seem and that even the most tragic situation can be a source of great inspiration if you choose to make it so.

I found the following quote by Ralph Waldo Emerson hung in Chris' room. It was obviously important to him.

> "To laugh often and love much; to win the respect of intelligent persons and the affection of children; to earn the approbation of honest citizens and endure the betrayal of false friends; to appreciate beauty; to find the best in others; to give of one's self; to leave the world a bit better, whether by a healthy child, a garden patch or a redeemed social condition; to have played and laughed with enthusiasm and sung with exultation; to know even one life has breathed easier because you have lived - this is to have succeeded."

Chris, I dedicate this work to you, your garden patch and where it is forever Spring.

ACKNOWLEDGEMENTS

It has been a long, arduous and oftimes painful journey to reach this point, and there have been many good folk along the way that helped me to arrive. I would be a poor human being indeed, if I went without thanking them here.

Many thanks and exhaustive amounts of praise to Rodey Batiza, advisor, principal investigator, friend and ally, renaissance man. His guidance and support both financial and mental have made me what I am today: a much relieved Master of Science. (It sounds so exhalted, does it not?)

I would also like to thank my committee members Alex Malahoff, Sandy Shor and Tom Reed for their invaluable assistance. Thanks, Tom, for your patience and tirelessness in educating me in the wonderful world of computer technology. Also, thanks to Karen Sender for imparting SeaMARC wisdom (among other gems), to Terri Duennebier for introducing me to the mystique that is the Penthouse, and to Pat Townsend who may now believe that computers are capable of holding a grudge. I also want to thank Marilyn, my favorite librarian. Some day, Marilyn, they'll write a song for you, too.

Boundless (we're talking beyond the furthest reaches of our universe) gratitude to the many friends I have been fortunate enough to have gathered while on my quest, for all the support (moral and emotional), advice, good memories and laugh attacks they have given me along the

way. Thanks to all you Zoo-ites (Devi, Jill, Paul, Fernando, Mary, Rick, Bruce) who ever stopped to help with the perpetual problems that arise whenever a Zayac sits in front of a computer terminal. Most especially I would thank Anne, El Kirbo, Kris, Beth, Ron, Janice, Nancy, Mike, Kathy, Kirk, the kids, Jill, Sylvia, Bill, and Diane for helping me through Life's low moments of grief and unemployment. Stories of your kindness and generosity always make my mother cry. I never would have made it without you guys. Special accolades to Nancy, an amazing officemate who showed such remarkable restraint in not killing me. If one is truly judged by the quality of one's friends...boy, am I in trouble! But seriously, I just want to know one thing: Slobodnik, do wild wartpigs really live in Aiea?

My greatest thanks, of course, goes to my family for all their love and support and without whom I would not be here today. Mom, Dad, Marc, Steve, Chris, Gram, thank you for making me laugh more than a body has the right to, annoying me more than one deserves, putting up with my charming (HA!) demeanor in good times and bad and for keeping me going. Bozena, welcome to my family, where there is never a dull moment. Chuckles, woof. Also, great thanks to Aunt Pauline, wherever you are; you knew I'd make it. I only wish you could have seen it. It was glorious!

This study was funded by ONR grants N00014-88-K-0031 and N00014-90-J-1633.

TABLE OF CONTENTS

LIST OF TABLES

LIST OF FIGURES

CHAPTER 1

INTRODUCTION

This thesis consists of two related studies which are presented in the following chapters. Chapter 2 serves as a general background source of information about elevations on the seafloor, known as seamounts. It provides a synthesis of information on how environmental and geological processes affect the morphology of seamounts. The chapter is divided into specific subsections pertaining to the process being reviewed.

Chapter 3 makes up the second major portion of this thesis. This is a study to determine the effectiveness of SeaMARC II, a long-range, high-resolution seafloor mapping system, as a geologic mapping tool. The ability of SeaMARC II to distinguish different lithologies was ascertained by correlating ground truth data from ALVIN dive observations, ANGUS towed camera films and rock samples with features derived from the backscattered energy used to produce SeaMARC II images. Chapter 3 describes the methodology and results obtained from the data from Seamount 6, a well-surveyed seamount located near the East Pacific Rise at about 12^{o} N and 102^{o} W.

CHAPTER 2

PROCESSES AFFECTING SEAMOUNT MORPHOLOGY

INTRODUCTION

The morphology of seamounts is a function of a variety of processes. Some are primary controls, such as volcanic processes, tectonics and bathymetry. Other controls are secondary, affecting the shape after the main edifice has formed. These controls include sedimentation and sediment transport, current action, erosion and mass wasting and reef cap growth. In this paper, I will examine how these processes influence the morphology of seamounts.

Guyots, atolls and volcanic islands are included in this discussion since they are subject to the same controls. In general, terms are defined as follows. Seamounts are local, steep-sided bathymetric highs. For our purposes, we are only interested in structures formed by volcanism. Not all seamounts have a volcanic origin; some have formed by serpentinite diapirism in the Mariana fore-arc [Fryer and Fryer, 1987]. Guyots are drowned, ancient islands with flat tops. The flat summits are considered to be the result of wave truncation. Atolls are volcanic islands which have subsided or are subsiding, and are capped with coral reef crowns. Volcanic islands are, of course, edifices which rise above sea level.

Volcanoes in the south and west Pacific Ocean are found predominantly in large, linear island and seamount chains (Figure 1). Most likely, these are of hotspot origin [Batiza, 1989]. In the east Pacific, most seamounts are clustered and isolated (Figures 2 and 3) [Menard, 1964]. Most of these seamounts are probably not hotspot related but are linked to mid-ocean ridge volcanism [Batiza, 1989]. Non-linear volcanoes form where conditions for melt generation and eruption exist. Some forming near the East Pacific Rise are fed by the ridge [Hekinian et al., 1983]. Others result from excess volcanism at ridge crest offsets. Batiza and Vanko [1985] showed seamounts may be produced at the intersections of failed spreading centers and at failed transform faults. It was shown by Batiza et al. [1989a] that non-hotspot volcanoes in the Atlantic Ocean and near the Mid-Atlantic Ridge (Figure 4) are similar in distribution, abundance, morphology and origin to those in the Pacific Ocean.

SIZES AND SHAPES

Seamounts come in a wide range of sizes and shapes. Batiza and Vanko [1983] and Fornari et al. [1987] described the morphology with increasing size, as follows: 1) tiny conical and dome-shaped lava piles (Figure 5), 2) irregular or polygonal shapes in seamounts up to 1 km high or less (Figure 6), 3) circular overturned soupbowl shapes, and 4)

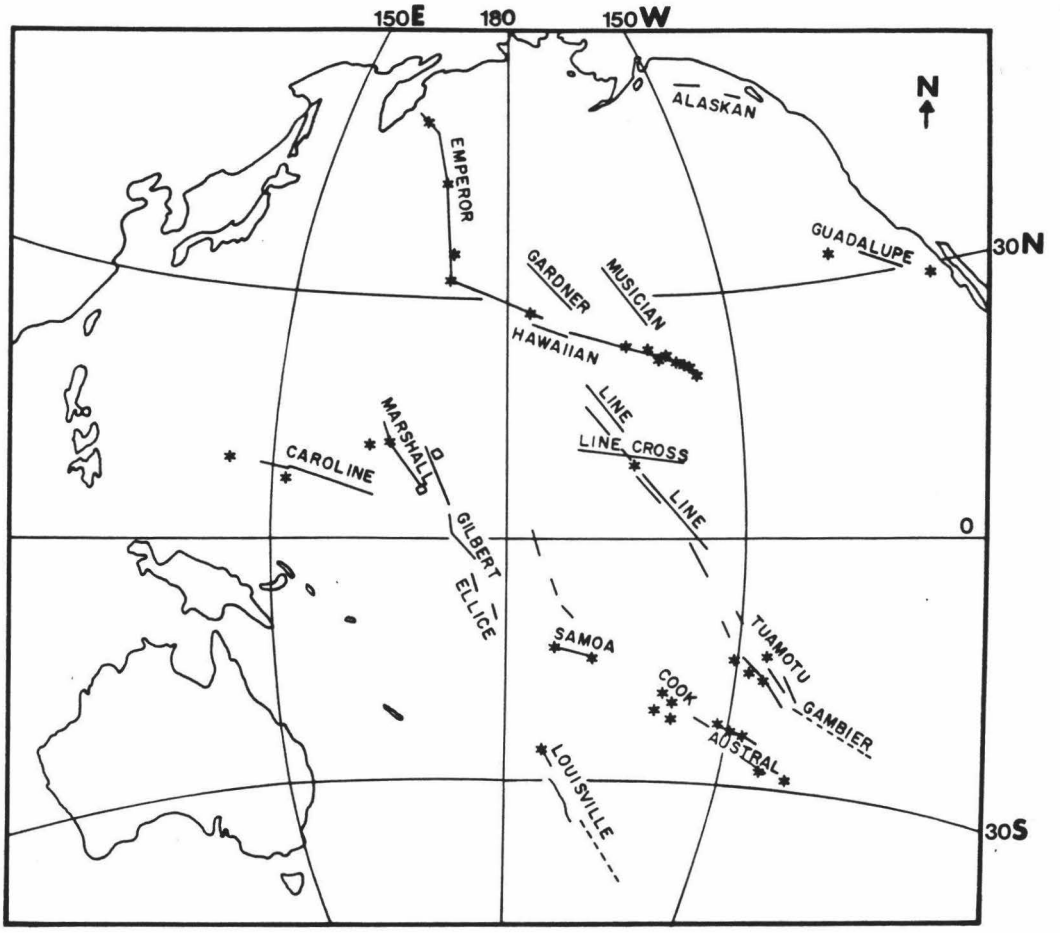

FIGURE 1. Linear island chains in the Pacific from Clague and Jarrard [1973].

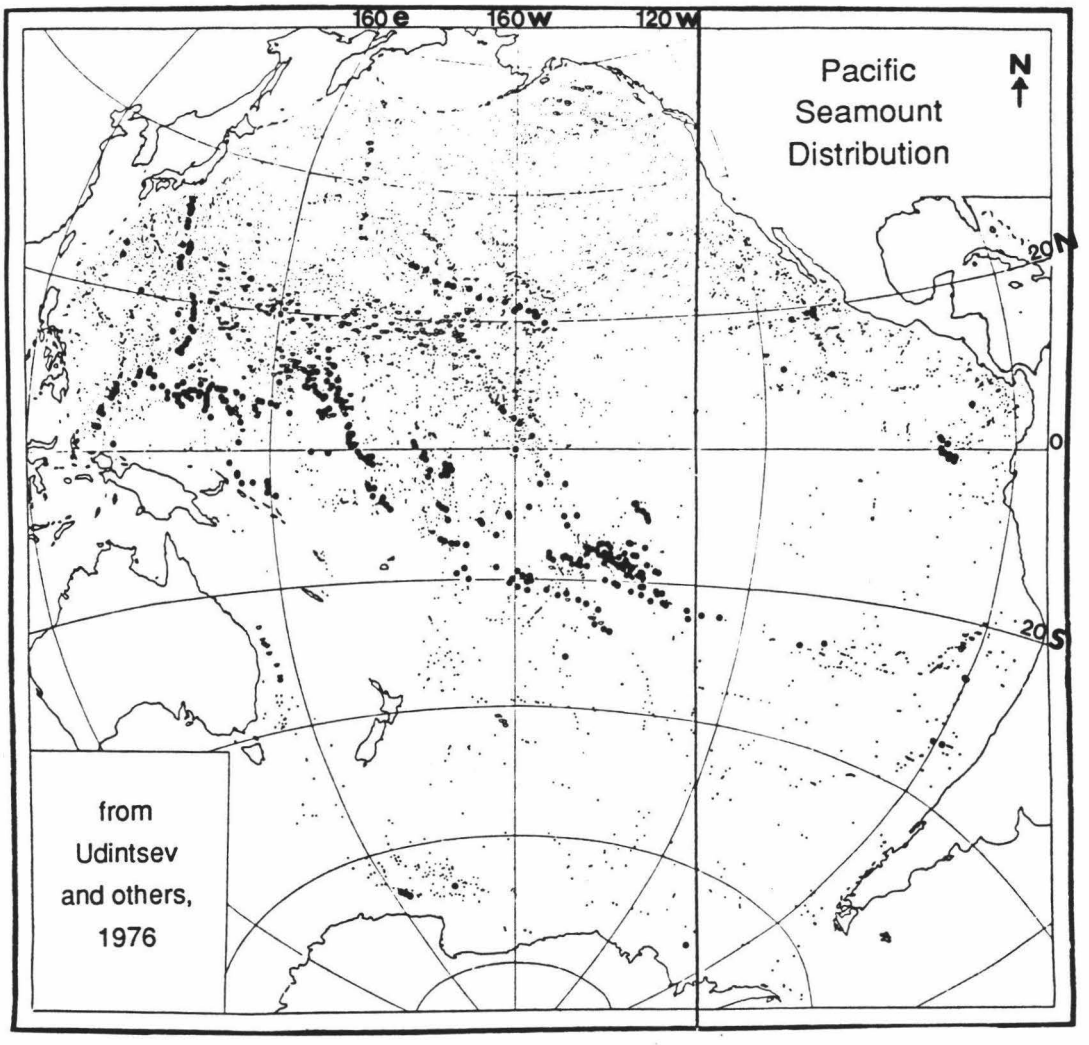

FIGURE 2. Map of the Pacific from Udinstsev et al. [1976] showing the location of known volcanoes. The sizes of the dots indicate relative volcano volume.

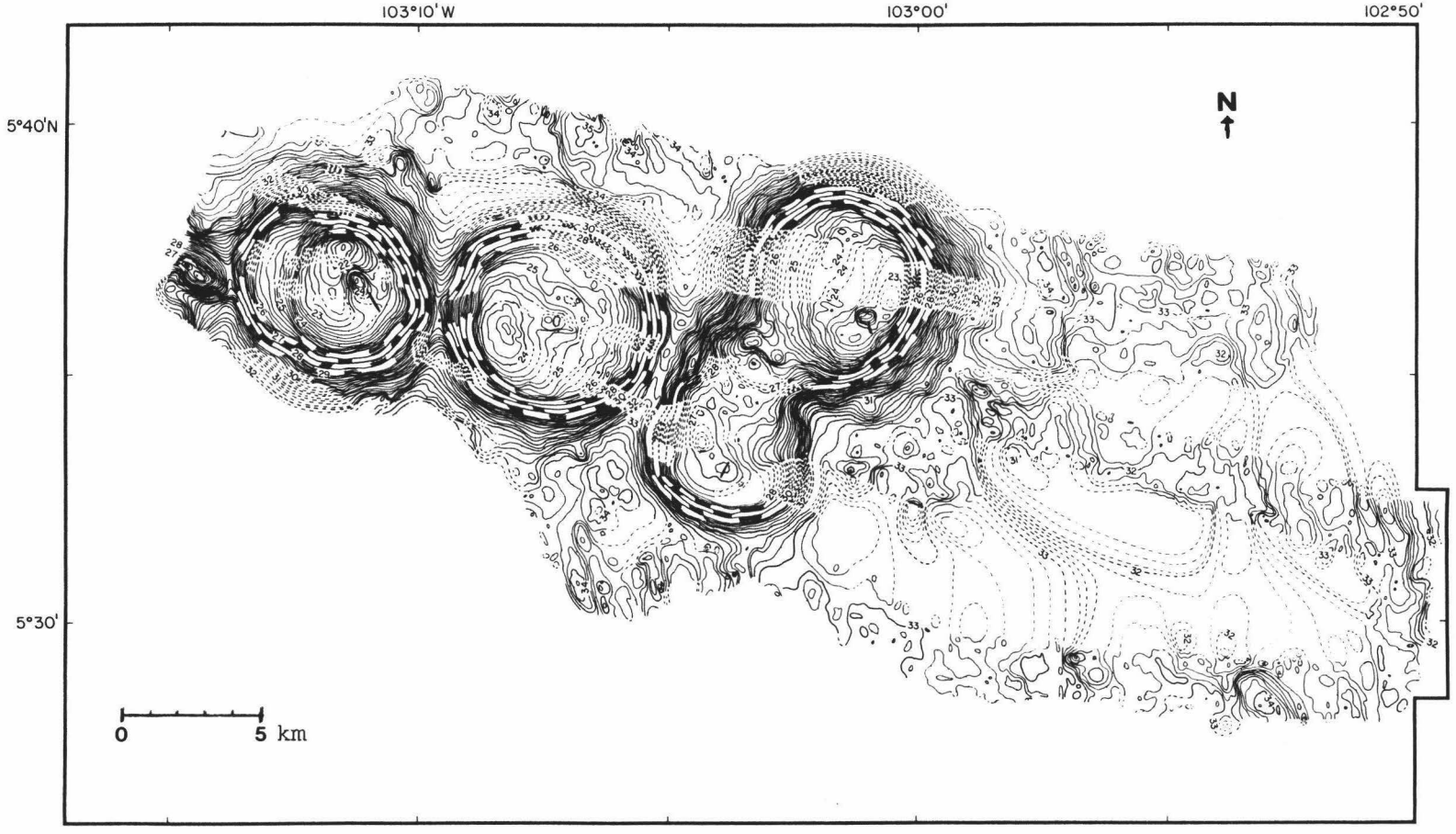

FIGURE 3. Bathymetric map of a typical cluster of seamounts generated near the East Pacific Rise. Notice the characteristic circular shapes, steep outer flanks and the broad, flattish summit regions.

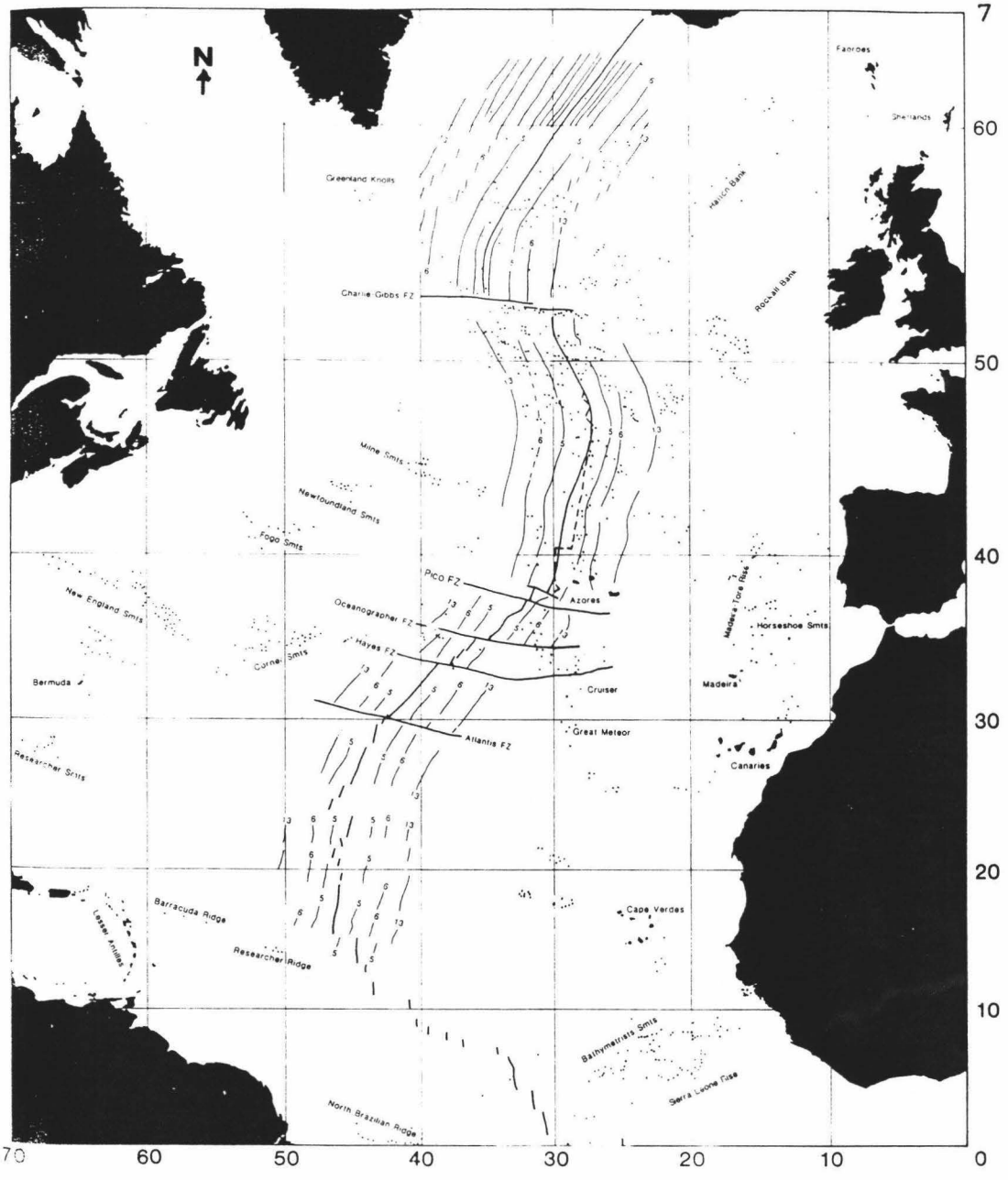

FIGURE 4. The locations of seamounts in the North Atlantic with heights greater than 50 fathoms (shown as dots). Magnetic lineations are from S. Cande (Pers. Comm. to Epp and Smoot). The dashed line shows the location of the topographic high between the Charlie-Gibbs fracture zone and the East Azores fracture zone; it does not correspond to anomaly zero [from Epp and Smoot, 1989].

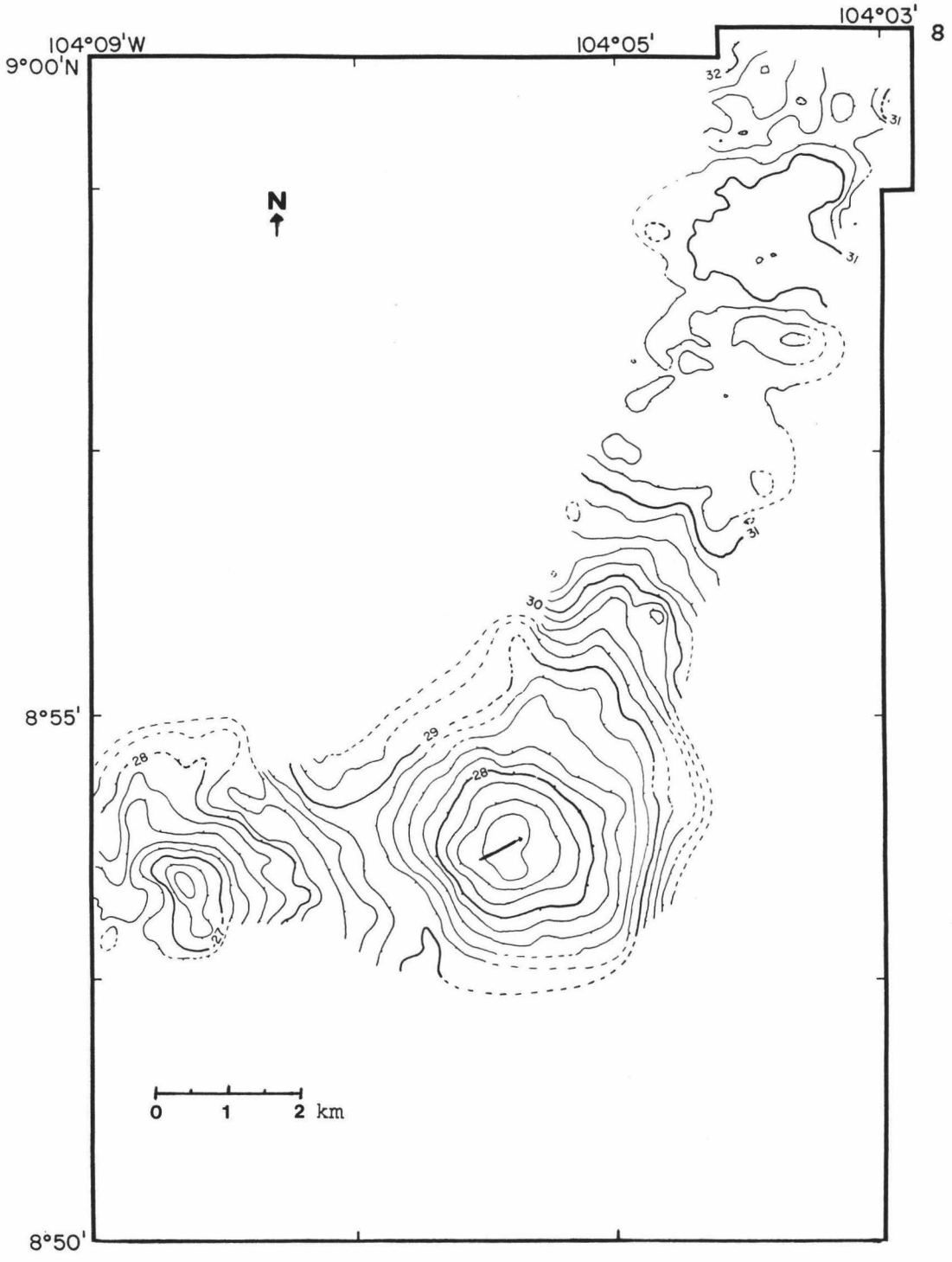

FIGURE 5. Bathymetric map of a small, conical seamount generated near the East Pacific Rise. In the early stages of its evolutionary growth, it displays the common morphology of many young seamounts.

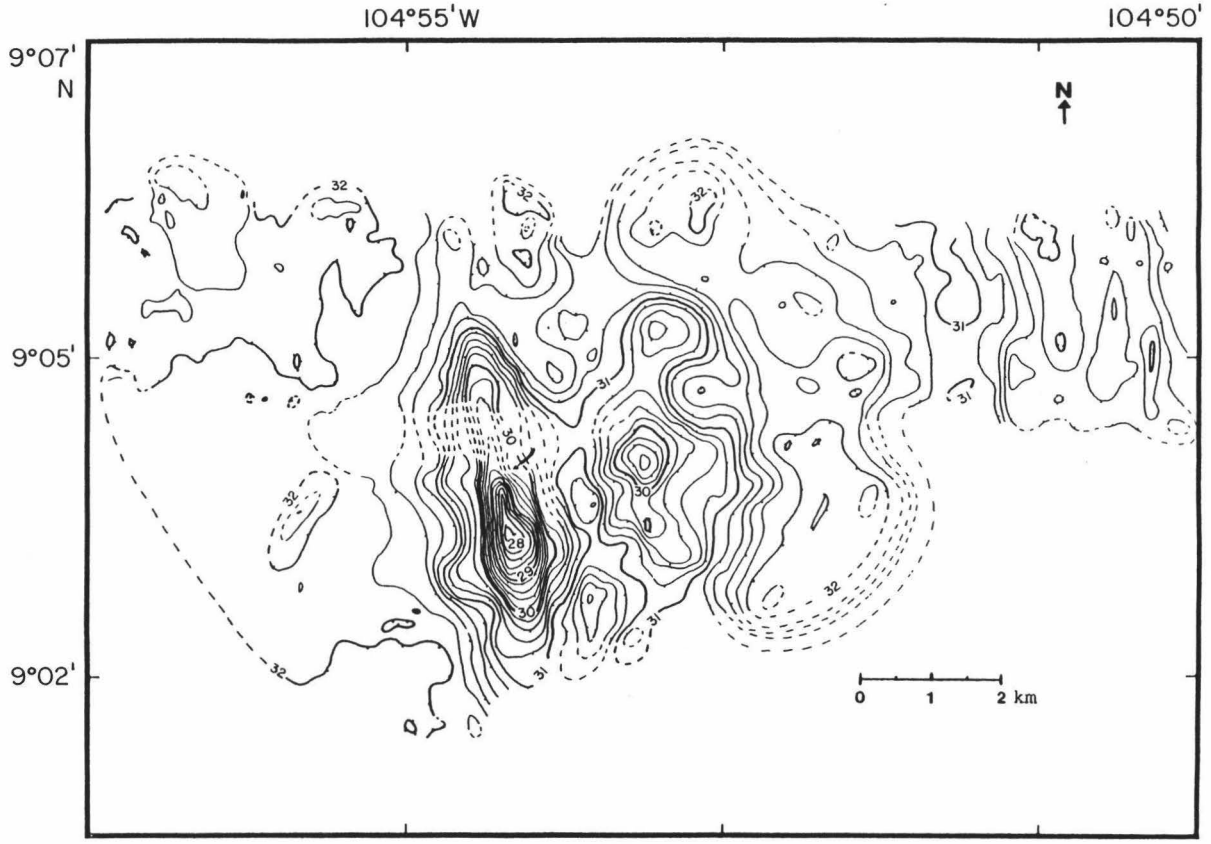

FIGURE 6. This irregularly shaped "H" seamount may have formed by erupting from parallel fractures. Note the western edge of the "H" is much more developed than the eastern edge, which resembles an earlier evolutionary stage-the conical lava pile. The location is near the East Pacific Rise.

larger seamounts are either simply conical edifices or rift-dominated starfish shapes (Figure 7) [Vogt and Smoot, 1984]. Depending on the size of the seamount, the following features may occur: calderas or summit craters (Figure 8), broad flat summit regions (Figure 9), arcuate summit benches (Figure 10), surrounding satellite cones (Figure 11) and small lateral rift zones [Lonsdale and Spiess, 1979; Batiza et al., 1984; Fornari et al., 1984; Lonsdale and Batiza, 1980]. For instance, medium sized seamounts (1-2 km high) commonly have calderas and craters on their flat summits (Figure 12), and in many cases these are nested and/or breached [Fornari et al., 1987]; flank rift zones are usually absent or poorly developed. Oceanic volcanoes generally retain steep (18^{o}-20^{o}) average slopes until they reach volumes of about 5000 km^3 [Vogt and Smoot, 1984]. Beyond this, slopes tend to diminish toward the low values of large shields (8^{o}-10^{o}). Figure 13 shows this decrease in slope angle with an increase in volume.

The smallest Pacific seamounts (50-300 m high cones) tend to be roughly circular or elliptical with steep outer flanks and usually have flat tops (Figure 14) [Fornari et al., 1987; Lonsdale, 1983]. Seamounts generated near the East Pacific Rise (EPR) (Figure 15) are generally < 1-2 km high. Larger volcanoes (up to 1-2 km high) have more complex shapes and cratered summits (Figure 16). The summit calderas (i.e., diameters > 1 km) or central craters are typically several kilometers wide and several hundred

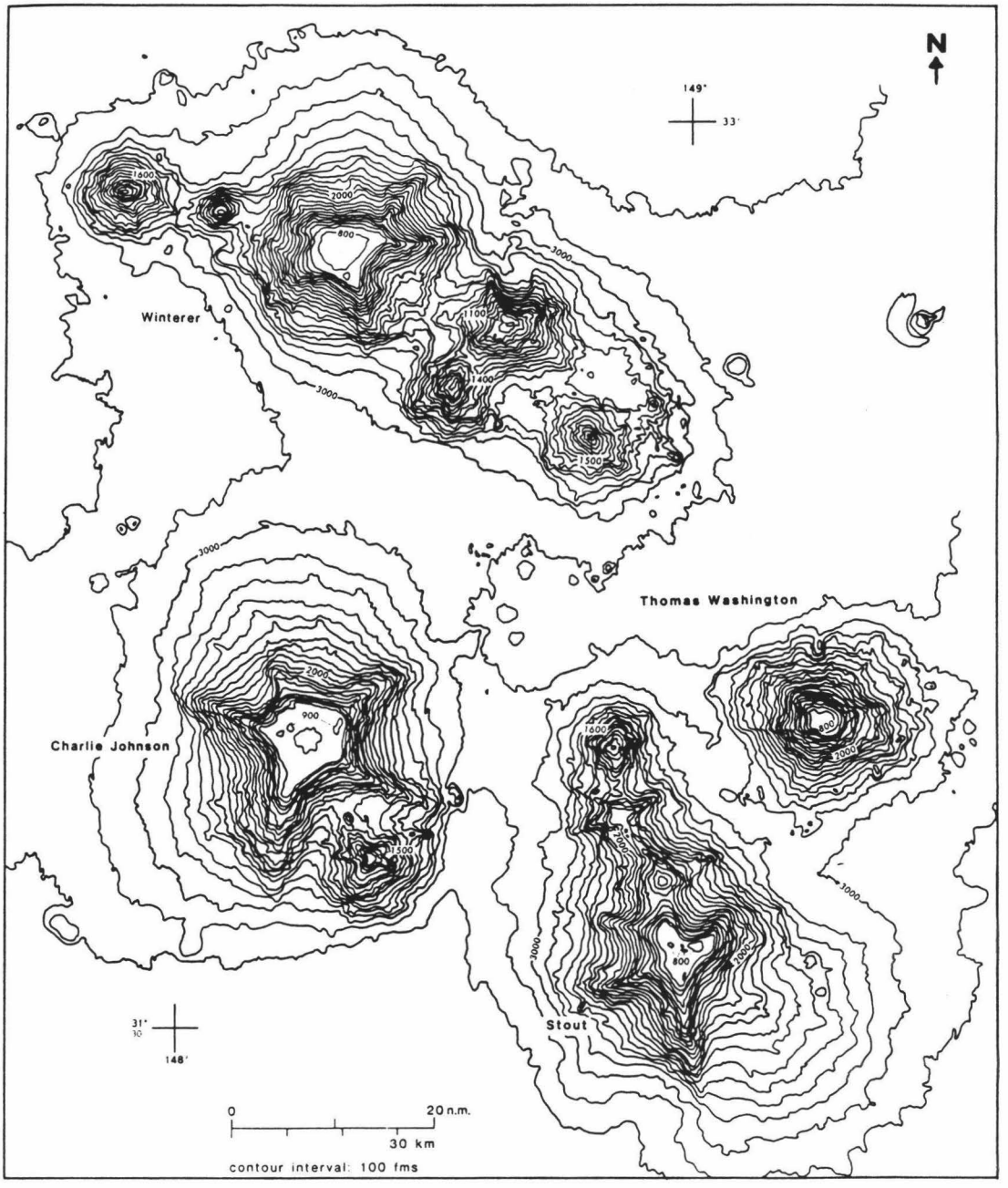

FIGURE 7. Bathymetric chart from Vogt and Smoot [1984] of the Winterer cluster of guyots and seamounts in the western Pacific. Note the distinctive starfish shapes resulting either from rift zone formation or mass wasting.

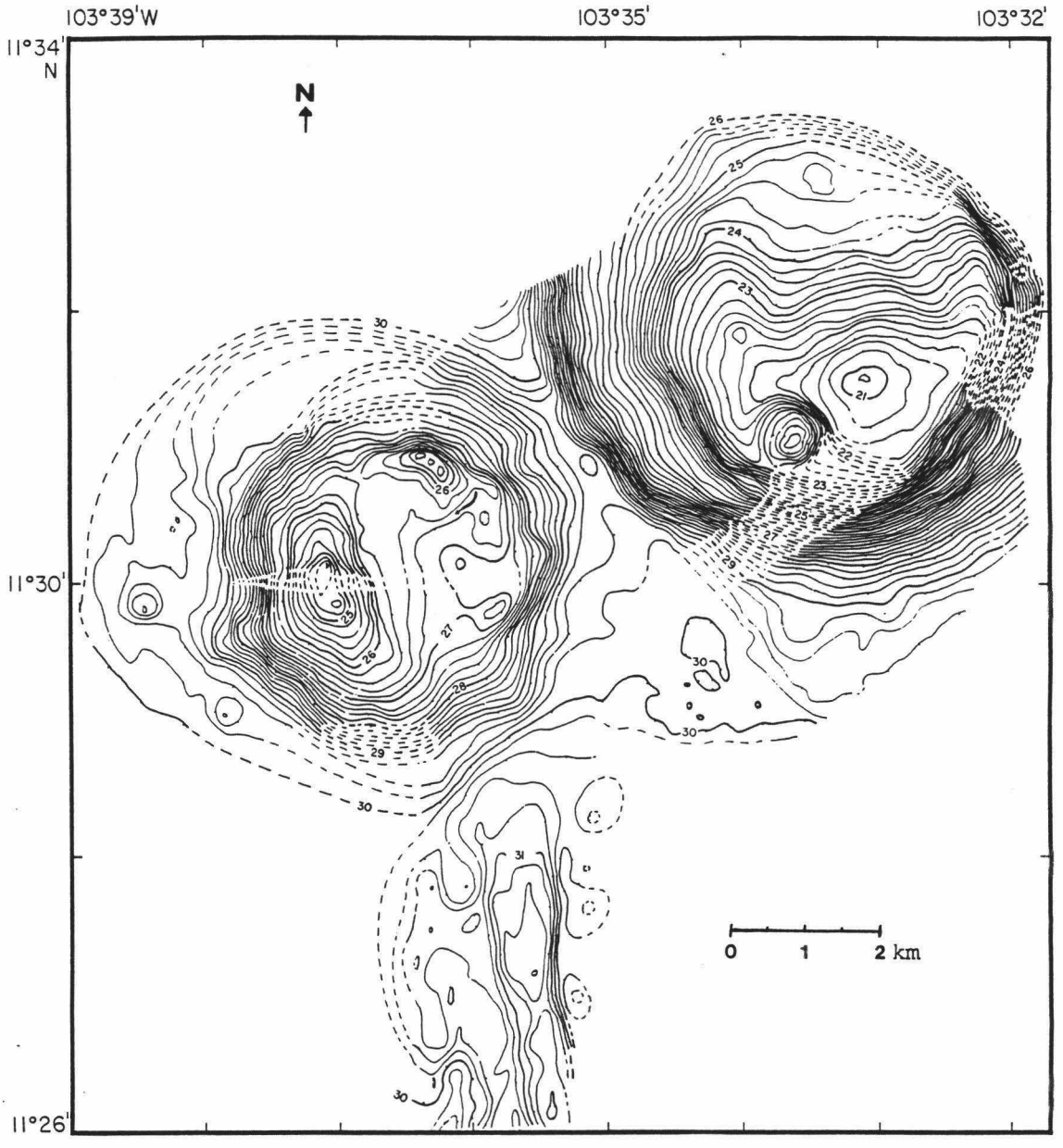

FIGURE 8. Bathymetric map of two seamounts generated near the East Pacific Rise (EPR). The edifice to the east posseses a summit crater, while the one to the west has a small pit crater. Note also the typical steep outer flanks and relatively flat summit regions of near-EPR seamounts.

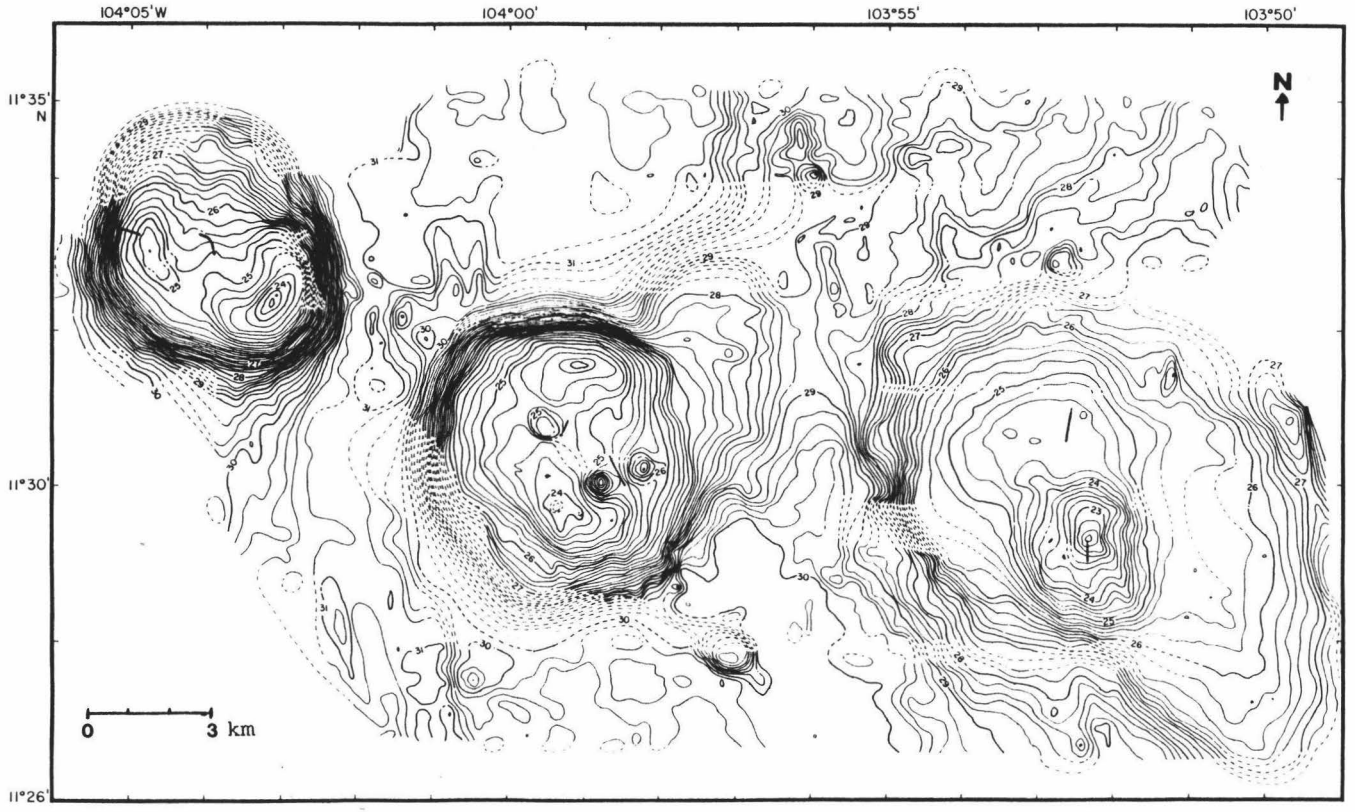

FIGURE 9. Bathymetry of small cluster of seamounts formed near the East Pacific Rise, displaying characteristic morphology of such volcanoes - steep outer flanks and broad, flattish summits. Notice two summit craters on the central edifice and the presence of several satellite cones.

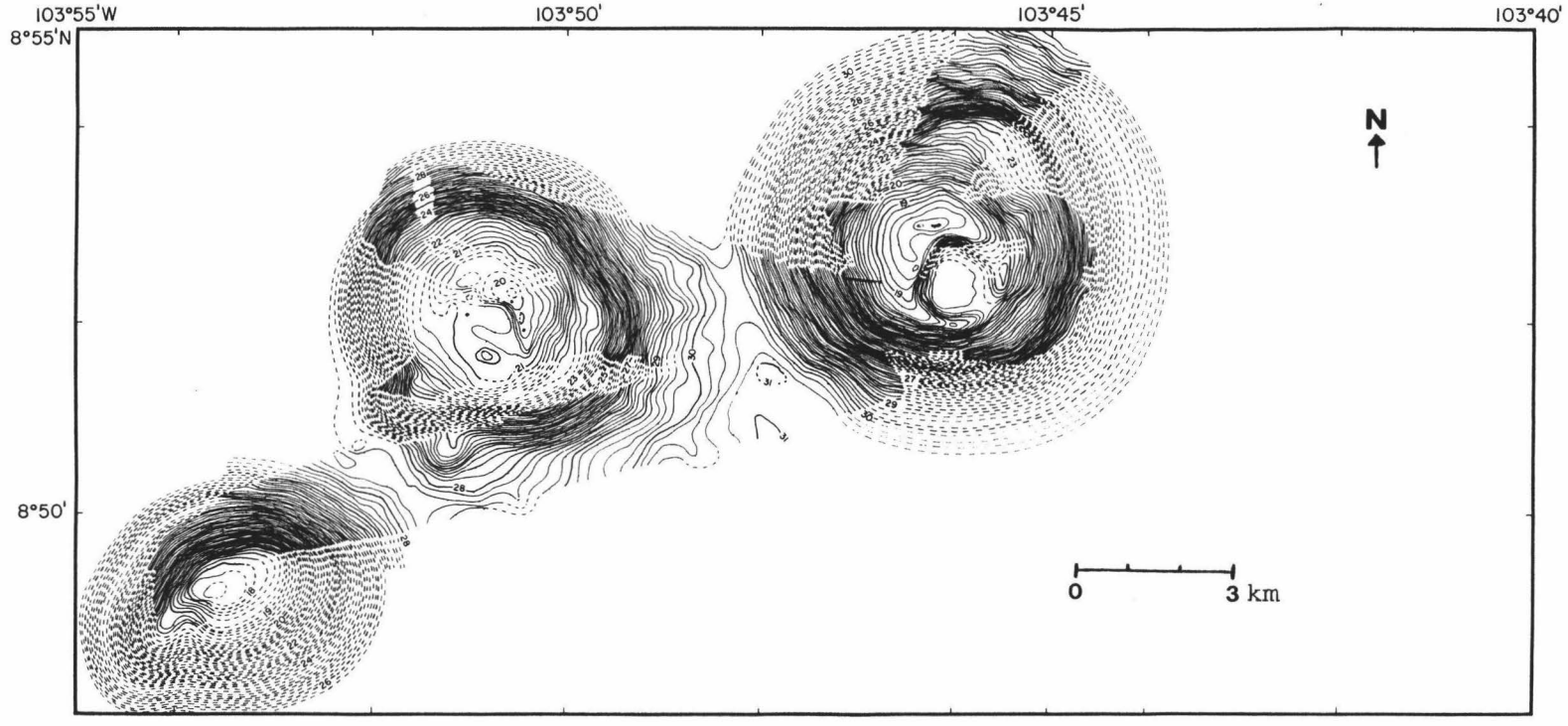

FIGURE 10. The central and eastern seamounts in this bathymetric map display arcuate summit benches. Evident on the easternmost seamount is a large caldera. Also noteable in these near-EPR seamounts, are the circular forms, steep outer flanks and flattish summit regions.

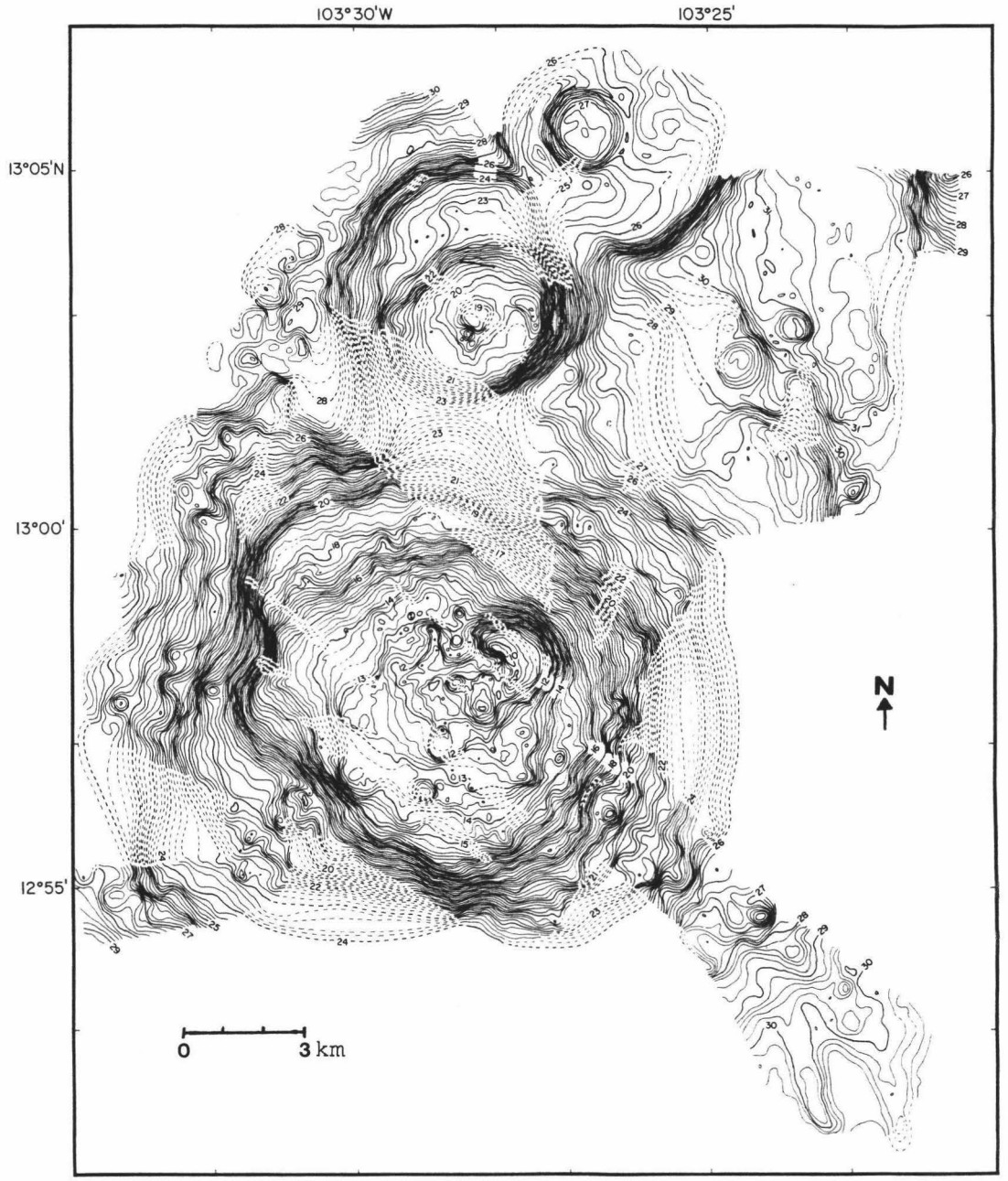

FIGURE 11. This bathymetric map shows many small satellite cones present about these seamounts located near the East Pacific Rise.

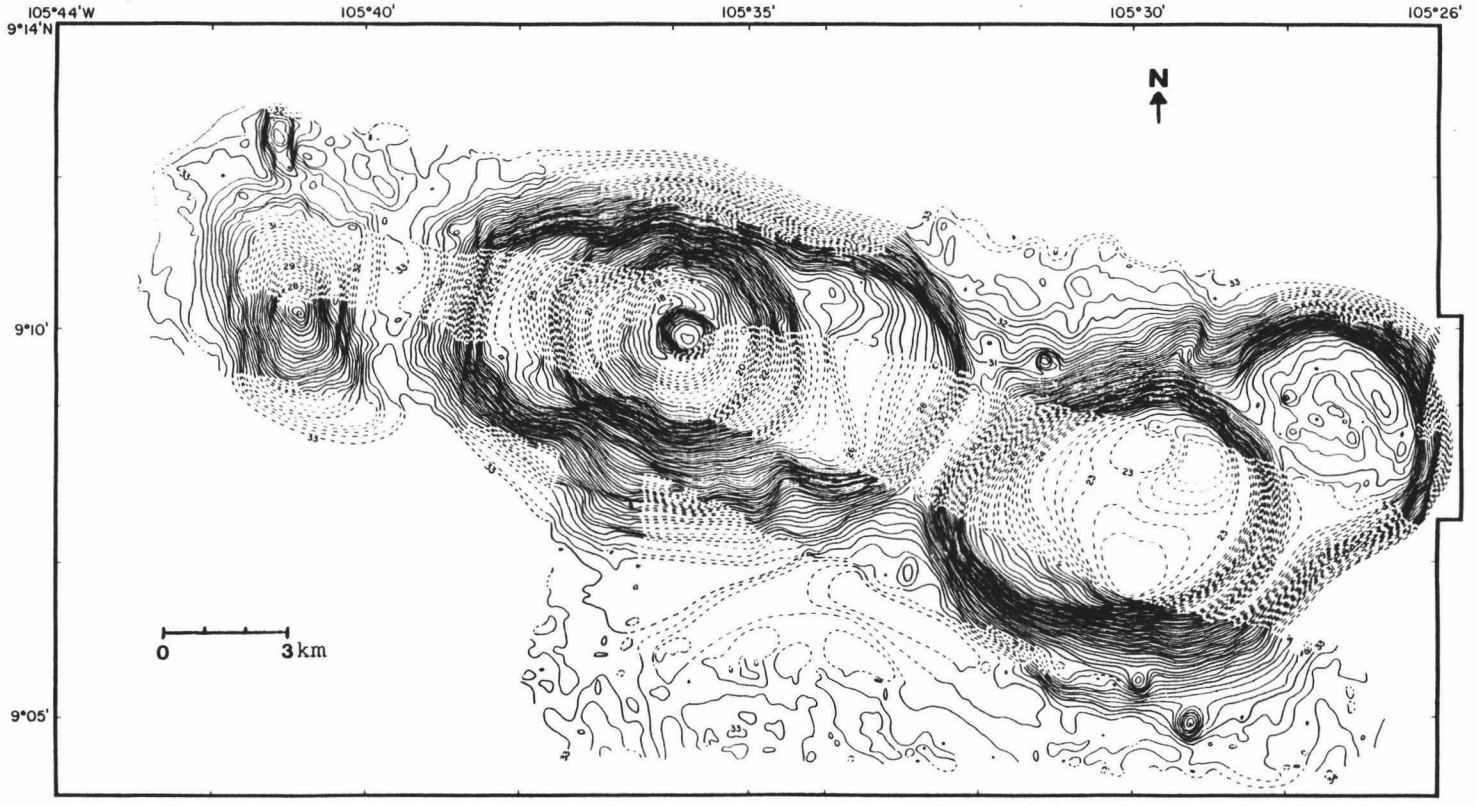

FIGURE 12. Bathymetric map of OCP ridge. The large, rectangular-shaped seamount in this bathymetric map possesses not only a large summit crater, but also an arcuate summit bench. The steep outer flanks, plus the relatively flat summits typical of seamounts generated near the East Pacific Rise are also shown.

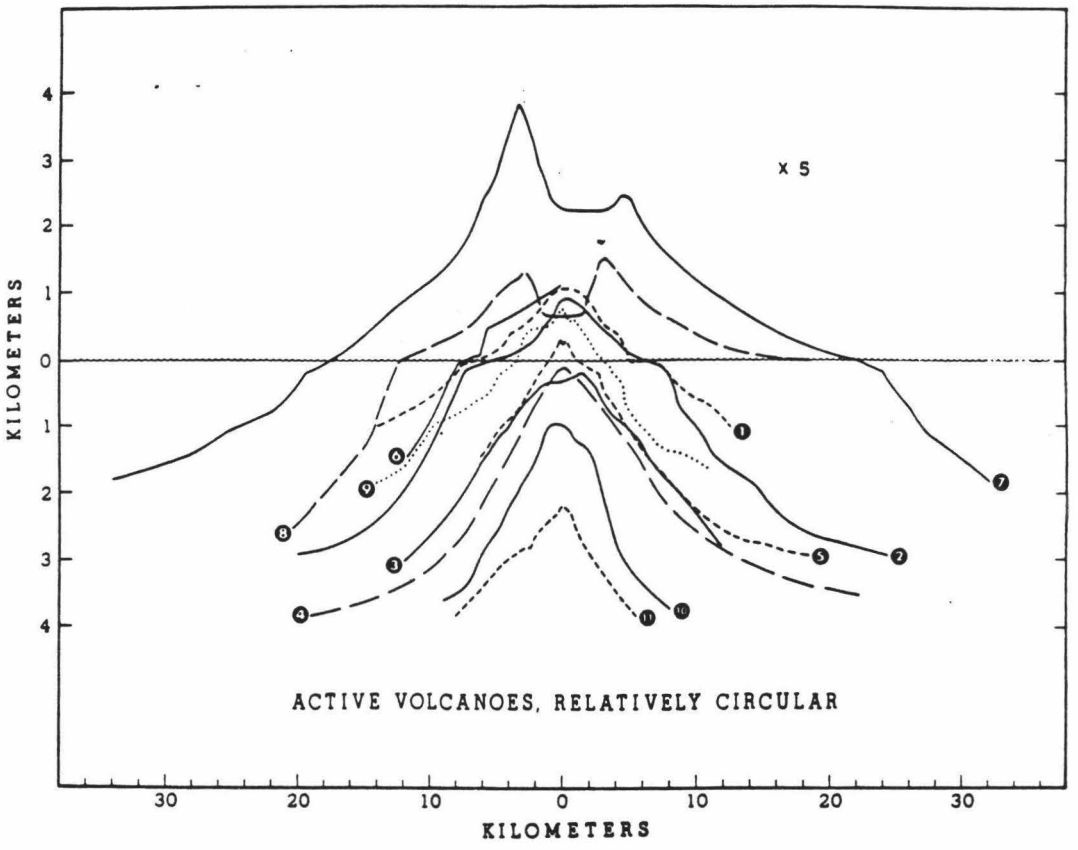

FIGURE 13. Profiles of active oceanic volcanoes, both islands and seamounts [from Menard, 1984]. As volcano volume increases, slope angles decrease. (1) Faial, Azores. (2) Socorro, Revillagegados. (3) Moua Pikaa, Societies. (4) Macdonald, Australs. (5) San Benedicto, Revillagegados. (6) Marion Island. (7) Tenerife, Canaries. (8) Fernandina, Galapagos. (9) Pinto, Galapagos. (10) Loihi, Hawaii. (11) Rocard, Societies.

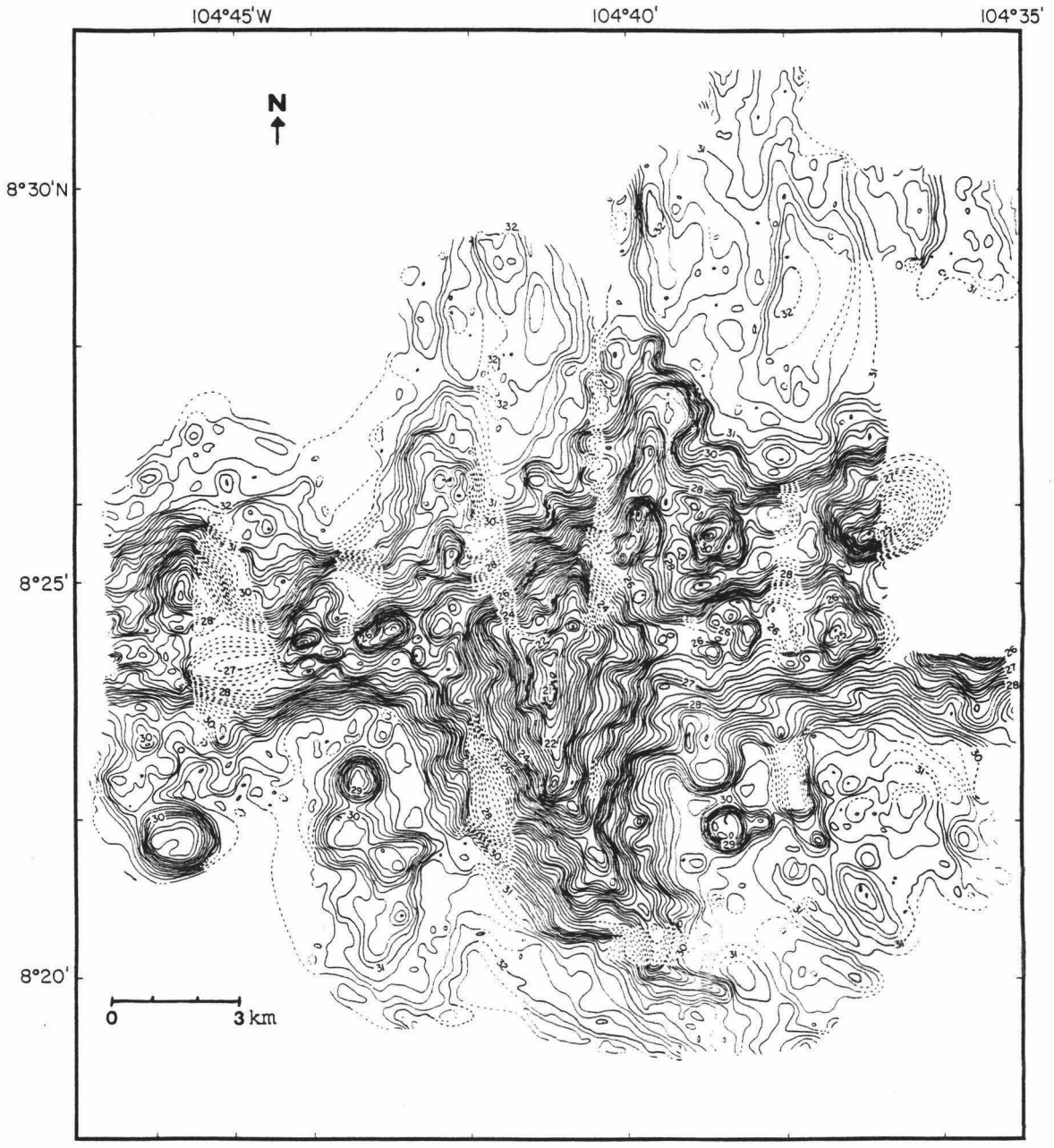

FIGURE 14a. This bathymetric map is of a lava field just east of the intersection of the Siqueiros transform and the East Pacific Rise (EPR), displaying the characteristic morphology of small Pacific seamounts- circular or elliptical with steep outer flanks and, usually, flat tops.

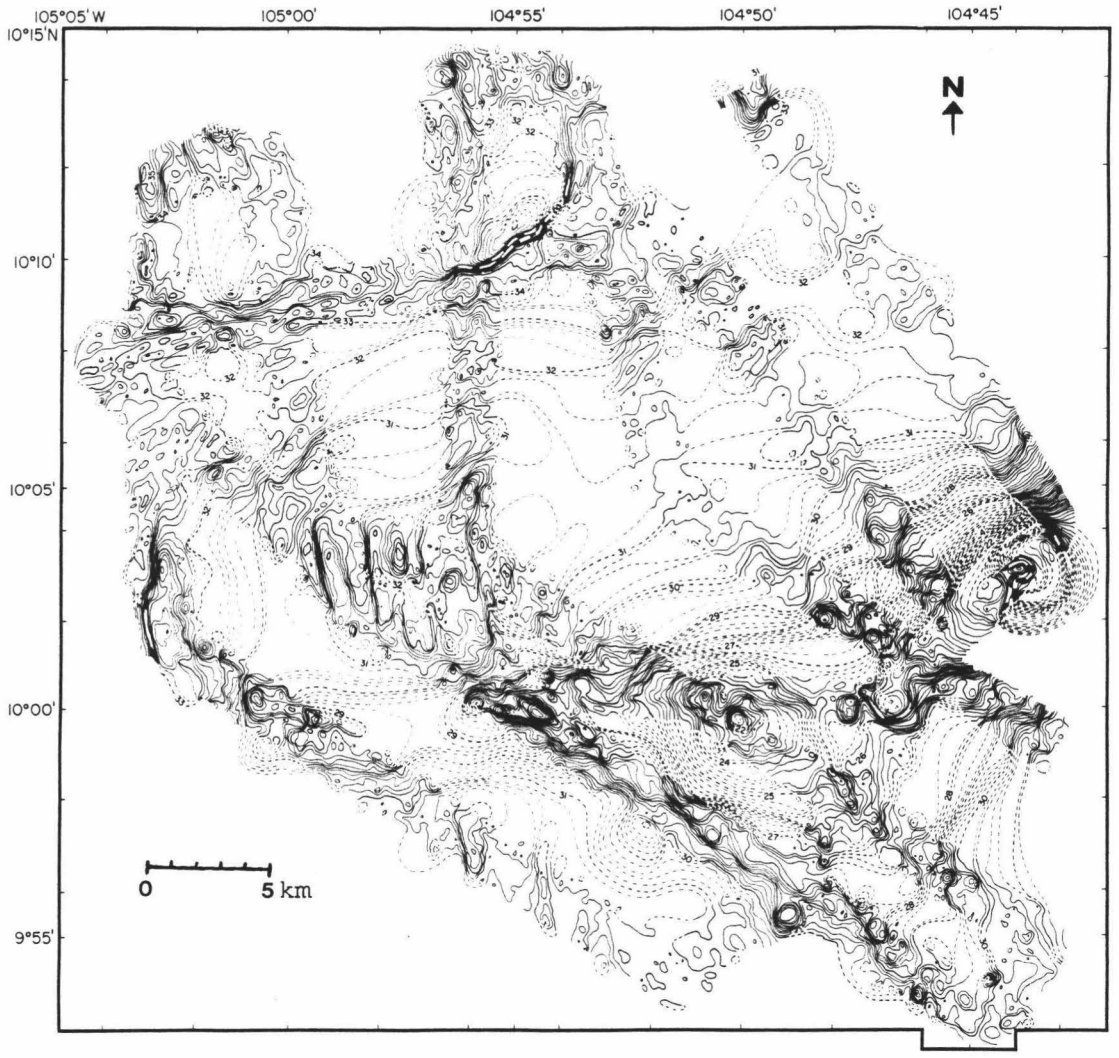

FIGURE 14b. This bathymetric map displays characteristic morphology of an area east of the intersection of the Clipperton transform and the East Pacific Rise. See caption for Figure 14a.

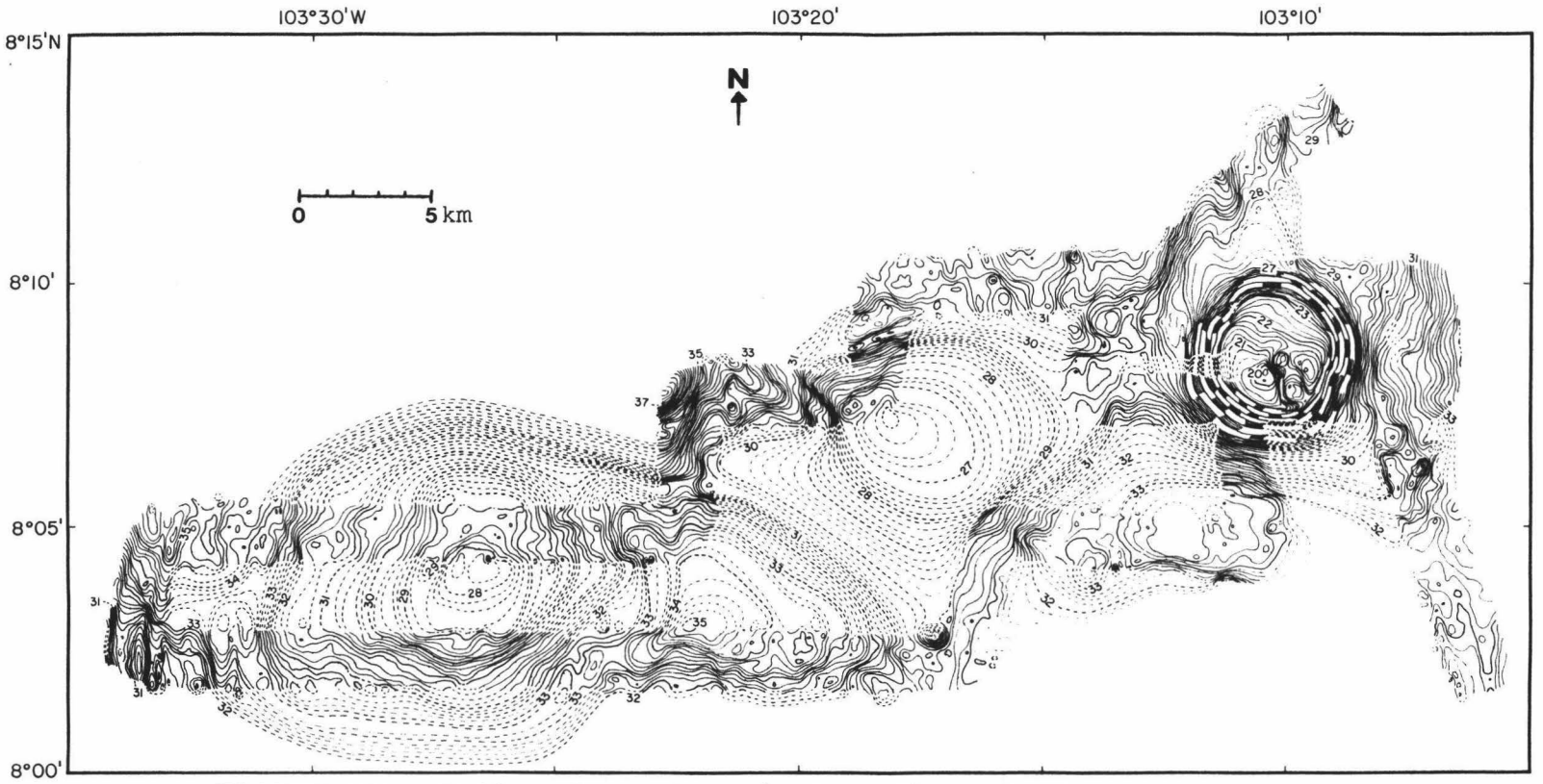

FIGURE 15. Bathymetry of typical medium-sized East Pacific seamounts. Note the steep outer flanks and relatively flat summits. The summit of the easternmost seamount is cratered. Also noteable are the beginnings of what seem to be northwest trending rift zones on the central and eastern volcanoes.

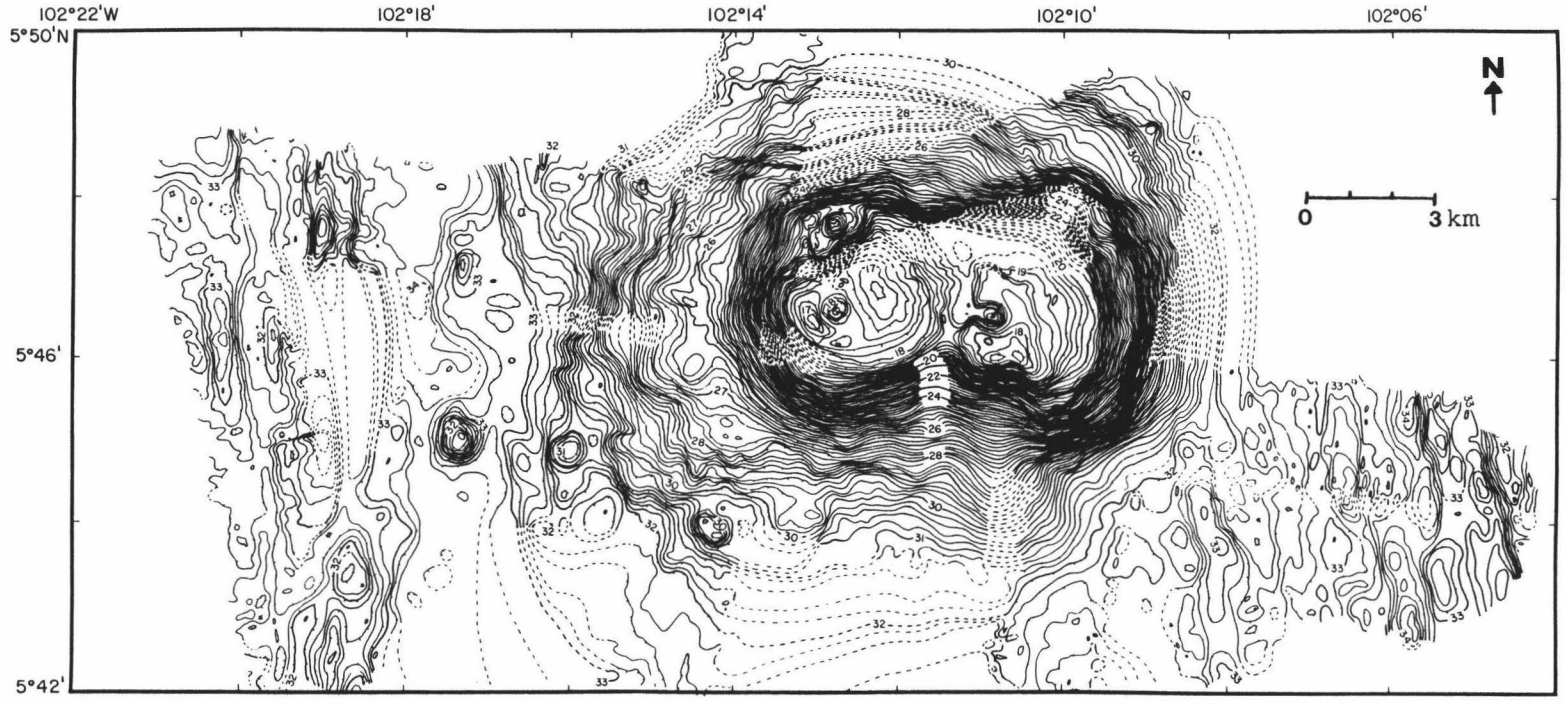

FIGURE 16. Bathymetry of a large seamount near the East Pacific Rise which may actually be two coalesced volcanoes, accounting for its polygonal shape. Many characteristic morphological features are in evidence here: steep outer flanks, a relatively flat, broad summit region, summit craters, arcuate summit benches and satellite cones.

meters deep with steep walls and irregular floors [Batiza et al., 1984]. Within the calderas, pillow mounds, talus piles and pit craters are seen (Figure 17) [Batiza et al., 1984]. Pit craters are about a hundred meters wide and deep and bounded by fault scarps [Lonsdale and Spiess, 1979]. These larger seamounts were formed from a number of eruptions and have longer and more involved histories [Batiza and Vanko, 1984; Fornari et al., 1988; Fornari et al., 1987]. Small seamounts are present in the inner rift valley and on the flanks of the MAR (mid-Atlantic Ridge), in the FAMOUS area [Walker et al., 1984; Phillips and Fleming, 1978; Bryan and Moore, 1977], and in other parts of the Atlantic. Indeed, Batiza et al. [1989a] have shown that MAR and EPR near-ridge seamounts display similar shapes, sizes, distribution, abundances and chemistry. This seems to indicate that the production of seamounts is a normal mid-ocean ridge process independent of spreading rate.

Small seamounts are much more abundant than large ones in the Pacific (Figure 2) and the Atlantic Oceans, but the total volume of smaller seamounts is less than that of the larger ones. In the Pacific, seamount abundance increases with crustal age on crust of Eocene and younger age. On lithosphere older than Eocene age, the size of seamounts increases while the abundance decreases with increasing crustal age [Batiza, 1982]. This trend is also seen in small Atlantic seamounts, the abundance falling off with

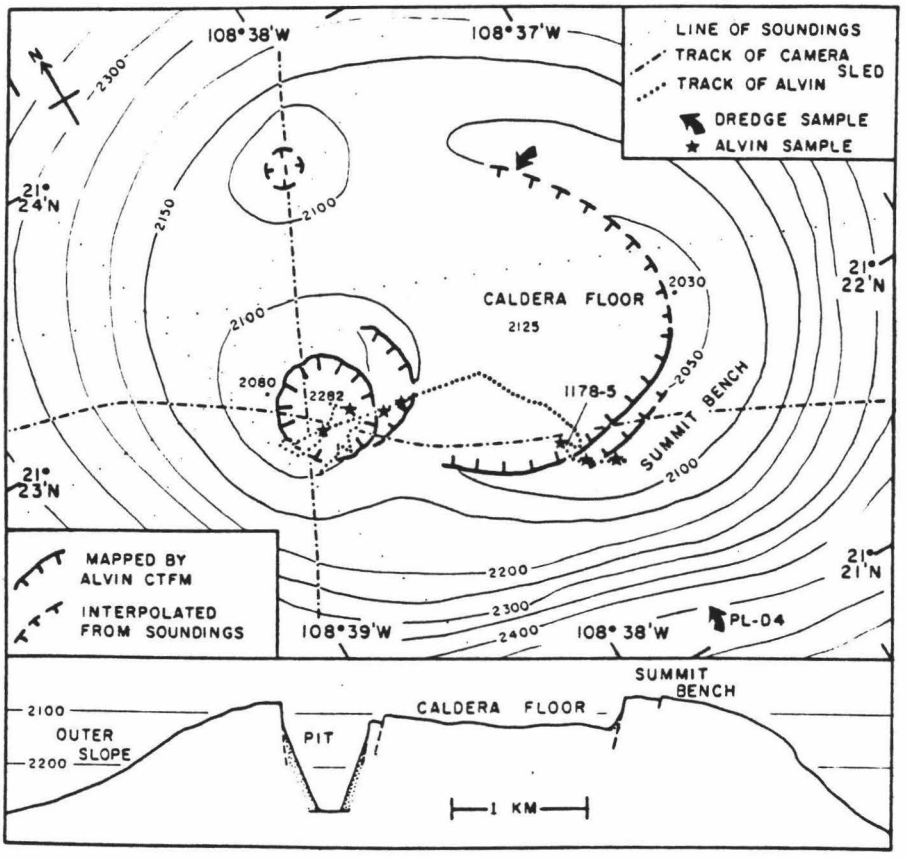

FIGURE 17. Bathymetry of the summit area of Seamount F [from Batiza et al., 1984], showing some of the typical morphologic features of seamount summits. Northwest to southeast profile at twice vertical exaggeration is constructed from the bottom pinger trace of the camera sled.

increasing lithospheric age [Batiza et al., 1989a]. In the Pacific, at least, the decrease in the number of small seamounts is attributed to sediment burial on the older lithosphere [Batiza, 1982]. Also, the increase in larger volcanoes is probably due to the affect of increasing lithospheric thickness on the maximum size volcanoes may attain [Vogt, 1974b].

PRIMARY VOLCANIC PROCESSES

The primary morphology of volcanoes depends on several factors, including morphology of magma conduits, eruption rate, magma viscosity, previous topography and regional and gravitational stresses within the edifice. Fractures, faults and joints act as conduits, providing preferred paths for the transport of magma. Eruption rate is related to magma availability and magma viscosity which are major controls in producing various lava flow forms. Pre-existing topography also contributes to the morphology of lava flows. Regional and gravitational stresses are important in controlling the shape of the volcano.

Vogt [1974b] suggested that the size of seamounts is controlled by lithospheric thickness, since the largest volcanoes seem to be on the oldest, thickest lithosphere. Nakamura [1977] and Kear [1964] showed how vent alignment and elongate shapes of volcanoes reflect regional tectonic stresses and fault patterns. Fiske and Jackson [1972]

demonstrated that gravitational stress within a volcanic edifice can localize eruptions along linear zones of maximum tension. This model explains linear volcanic rift zones. Simkin and Batiza [1984] used Fiske and Jackson's model to explain flat-topped seamounts. They suggested that a doughnut shape of the edifice is established by cratering, and then gravitational stresses maintain volcanic conduits that are circular in plan view. Extrusions of lava from this ring may then flow into the crater, eventually filling it and forming a flat top (Figure 18).

Fornari et al. [1987] argue that the shape, size and arrangement of magma supply conduits is a very important control on the shape of volcanic landforms. For instance, if the magma conduit is a point source, conical lava piles will result; if it is a fissure, a ridge-like feature will result. They go on to say that the irregular or polygonal shaped seamounts owe their shape mainly to the shape and geometry of these conduits. Irregular shaped seamounts are seen as primary growth forms, probably fed by a series of conduits which are controlled by sets of intersecting seafloor faults and fractures that form the polygonal outline [Batiza and Vanko, 1983]. Examples of possible conduit patterns are shown in Figure 19.

As seamounts grow, their shapes probably evolve. It is possible that the large, circular volcanoes (1-2 km high) begin as irregularly shaped seamounts. Eruption

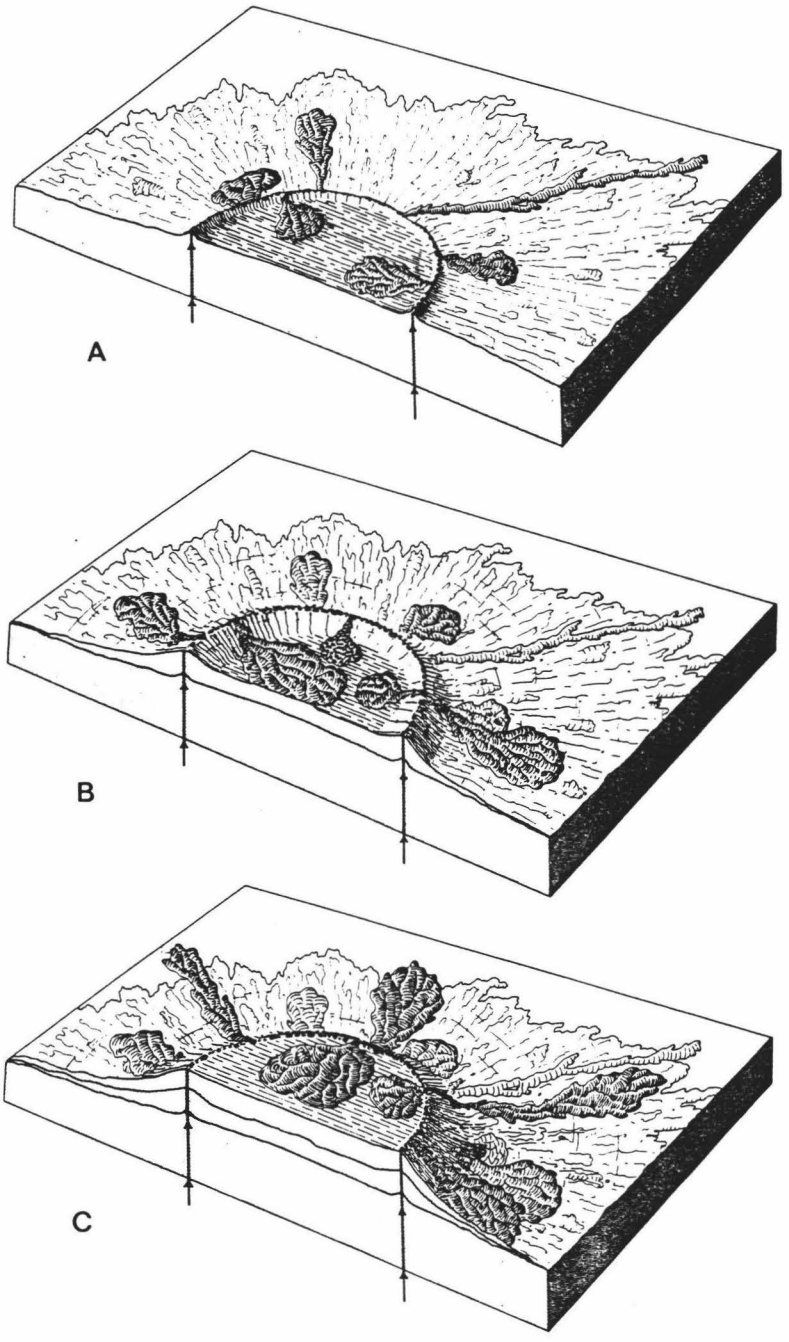

FIGURE 18. Schematic figure [from Simkin, 1972] illustrating how a flat top may develop because of extrusion from ring-shaped conduits.

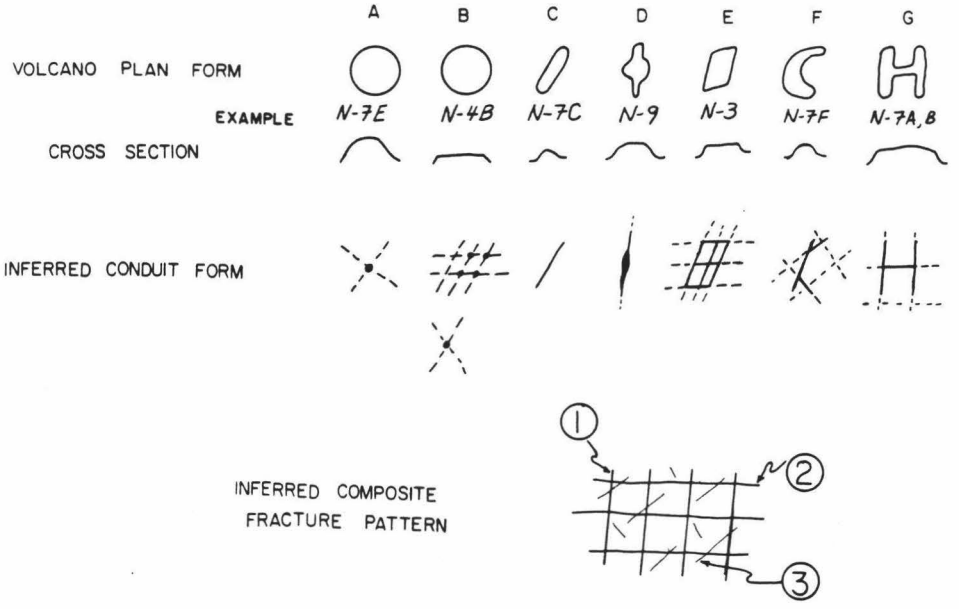

FIGURE 19. Examples of inferred conduit shapes and patterns for small volcanoes of given plan form and cross-sectional shape [from Batiza and Vanko, 1984]. The composite fracture pattern is reconstructed from the inferred conduit geometry of individual volcanoes. It represents the composite pattern of fractures which could serve to produce all of the observed shapes of small volcanoes. The orthogonal pattern of fractures are the ridge normal and ridge parallel directions while the oblique direction is that of fractures found only near active transforms and presumably present on inactive fracture zones also.

through intersecting fractures produces intersecting linear volcanic ridges or a set of ridges that enclose a polygonal basin. With further eruption from the linear ridges, the basin fills. During this process, growth of the edifice is probably limited to a few hundred meters in elevation. The volcano may be large enough at this stage to possess a small magma chamber. Subsequent summit collapse due to the presence of such a magma body would produce a circular symmetry [Fornari et al., 1987]. This symmetry could lead to the formation of a new set of conical feeders. Further growth of the edifice would form larger, circular volcanoes.

Vogt and Smoot [1984] also propose an evolution of morphology between small and large volcanic edifices (Figure 20). They observed that some of the larger edifices in the Geisha Guyot cluster of the Northwest Pacific exhibit a distinct starfish-shaped morphology (Figure 7). In most cases, the starfish "arms", typically 3-6 in number, are thought to be flank rift zones such as those seen in the Hawaiian Islands [Fiske and Jackson, 1972]. These same starfish shapes are observed on guyots and volcanic islands larger than the Geisha Guyots, which are considered intermediate in size. Small seamounts are diverse in their morphology, but the starfish morphology is not observed. The length of flank rift zones increase (up to > 100 km long) as the size of the edifice increases. These observations suggest an evolutionary growth.

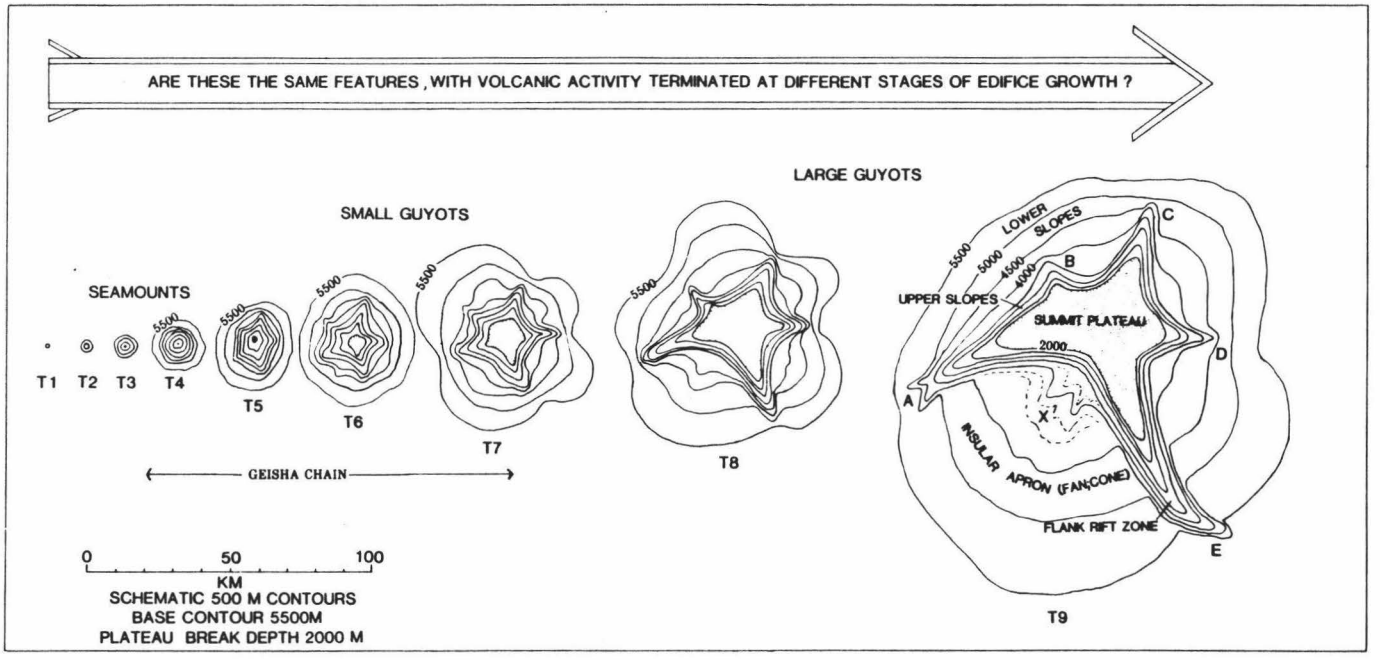

FIGURE 20. Schematic drawing [from Vogt and Smoot, 1984] showing possible evolution of small to large oceanic volcanoes. Note that guyots are among the largest individual volcanic features in the Pacific.

In studies of active flank rift zones [Fiske and Jackson, 1972; Ryan et al., 1981], observations indicate that magma rises in a central conduit and is then injected into flank rift zones from a shallow magma chamber. The intruding magma bodies are thought to be steeply dipping, bladelike sheets paralleling and bisecting the rift zone. Some injection events are accompanied by eruptions from the crest of the rift zone. Presumably, flank rift zones develop when the volcanic edifice reaches a critical size at which flank injection becomes easier than a summit eruption from the central conduit. Indeed, small seamounts lack flank rift zones [Batiza and Vanko, 1983], indicating it is easier to erupt from a low summit vent than to initiate rift zones [Vogt and Smoot, 1984]. Rift zones develop in response to the total regional stress field as well as the magma pressure [Vogt and Smoot, 1984].

The continued extension of the flank rift zone as the edifice increases in size reflects the increasing head of the magma column as the height of the summit increases. The higher the summit, the greater the pressure of the magma column at the base of the volcano and the easier it is to pump magma laterally into the flank rift zones. The length of the flank rift zones is limited by viscous losses and the gravitational pressure gradient [Vogt and Smoot, 1984].

The average and maximum rift length increases with summit plateau area. Rift lengths in large seamounts and

small guyots increase slowly with changes in pressure differential P (about .2 km/MPa) (Figure 21), and are all relatively uniform in length. (P is the pressure differential between the base of the magma column and the hydrostatic pressure at the same level without the edifice [Vogt and Smoot, 1984]). The rate of magma injection into these rift zones is low, and the shallow magma chambers are probably not well developed. High effective viscosity results in a high P gradient (5 MPa/km). At about 100 MPa, maximum rift length increases rapidly with an increase in P (about 3 km/MPa), but there is a great deal of range in the lengths of the rifts. This may indicate frequent injections and shallow magma chambers from which magma flows easily along flank rift zone conduits. The effective viscosity is low, allowing magma transport under low P gradients (.3 MPa/km) [Vogt and Smoot, 1984].

Regional tectonic stresses are important in controlling the initial geometry of the volcanic conduits. Eruption rate, distance from the vent, magma viscosity and pre-existing topography are all major controls on the form lava flows may take such as pillow lavas, lobate tubes, sheet flows, ponded lavas or hyaloclastites. As the volcano grows and becomes more sizeable, gravitational stresses within the edifice become important in controlling the morphology [Fornari et al., 1987].

Near axis seamounts show a preferential origin near transforms, fracture zones and overlapping spreading

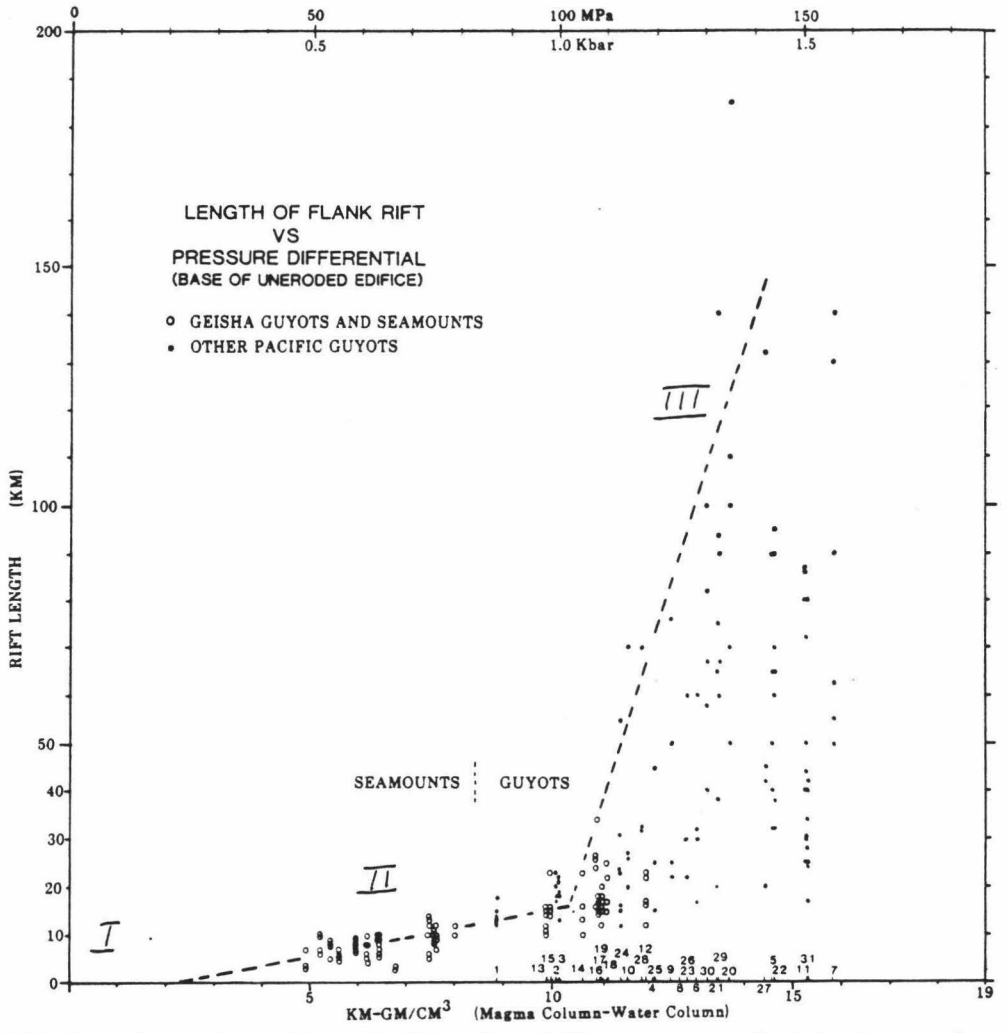

FIGURE 21. Length of flank rift zones plotted against P, the pressure difference between base of magma column (2.9 g/cm^3) below summit caldera, and hydrostatic pressure at the same level outside volcanic edifice [from Vogt and Smoot, 1984]. Numbers indicate guyots and unnumbered circles are seamounts of the Geisha chain. Data suggest 1) rifts are very short or absent on small seamounts, 2) rift length increases slowly (0.2 km/MPa) up to about 100 MPa (1 kbar), after which maximum rift length increases rapidly (about 3 km/MPa) with increasing P.

centers [Menard, 1969; Lonsdale, 1985; Fornari et al., 1984; Batiza et al., 1989a]. It is possible that at these locations, where the crust is fractured more than usual, there are more magma conduits available.

Different flow morphologies (pillows, sheet flows, hyaloclastites, etc.) are a function of magma chemistry, locus of flow source on the seamount (flanks or summit), rate of extrusion, and depth of the seamount. The upper slopes of seamount flanks probably represent the angle of repose for assemblages of pillow lavas, talus and coarse pyroclastic debris [Vogt and Smoot, 1984]. However, steeper slopes may occur. Walker [1973] showed that the length of lava flows depends on effusive rate and that volcano slope is inversely related to effusive rate. Small, slowly erupted submarine flows would produce a greater proportion of fragmented debris which can accumulate at higher angles of repose. If the average eruption produces a small amount of lava and small flows which cool quickly and do not flow great distances down the flanks, slopes will be steeper. The eruption of silica-rich lavas which are more viscous and will not flow far will increase slope angle. Eruptions which produce more pyroclastic material rather than lava flows also form steep slopes. Such eruptions occur generally shallower than 500 m, at a level where exsolving volatiles cause fragmentation of the magma [Fisher and Schmincke, 1984]. Other factors contributing to steeper slopes which are not primary

volcanic processes, include increased slumping during and after volcanism, slumping due to inflation and seismicity and coral reef growth. The upper slopes may have steepened due to coral growth and the accumulation of cemented calcareous debris following volcanism. Lower flank slopes of mature volcanoes are affected more by sedimentary processes rather than primary volcanic processes (discussed in a later section). However, Lonsdale and Spiess [1979] suggest that the lower slopes of young seamounts are lava flow aprons rather than sediment aprons found around emerged volcanoes.

Many seamounts or guyots have flat tops and/or step-like flat terraces and steep scarps. These are explained as results of wave erosion [Menard, 1964].

VERTICAL MOVEMENT

Sclater et al. [1971] explained the sinking of oceanic lithosphere due to thermal contraction with age. Volcanoes sitting on the oceanic lithosphere would be expected to sink along with it as it subsides. However, drilling on atolls and volcanic islands exhibit significant subsidence [Ladd and Schlanger, 1960] which cannot be explained by simple subsidence as the lithosphere thickens and cools. In other instances, uplift of volcanic platforms is seen. The study of such vertical movements is useful in determining properties of the oceanic lithosphere. The

possible causes of such motions are thermal and mechanical in nature.

Many atolls stand at higher elevations than expected for the age of the seafloor upon which they sit. Often, they are located near active or recently active volcanoes. Eustatic sea level highs are unable to explain the differences in elevations of atolls of the same age, or the extent of such a rise in sea level (in some instances as much as 70 m [McNutt and Menard, 1978]). This led McNutt and Menard [1978] to propose tectonic uplift due to deformation of the lithosphere by volcanic loading.

The lithosphere can respond to loads like a thin elastic plate overlying a fluid. Loads on the plate cause bending and displace the underlying fluid. Buoyancy forces from the displaced fluid are the actual supports of the feature producing the load, while bending of the lithosphere distributes the weight over an area greater than the feature itself. This flexure creates a depression near the edifice and a rise or arch further seaward (Figure 22) [Walcott, 1970]. Flexural studies are very important in determining mechanical properties of the lithosphere, such as: elastic thickness and flexural rigidity. Elastic thickness is the maximum thickness of the lithosphere allowable to account for a certain amount of flexure, assuming elastic plate behavior. Elastic thickness can be mathematically determined by modelling to fit a certain flexural profile, or can be estimated using gravity and

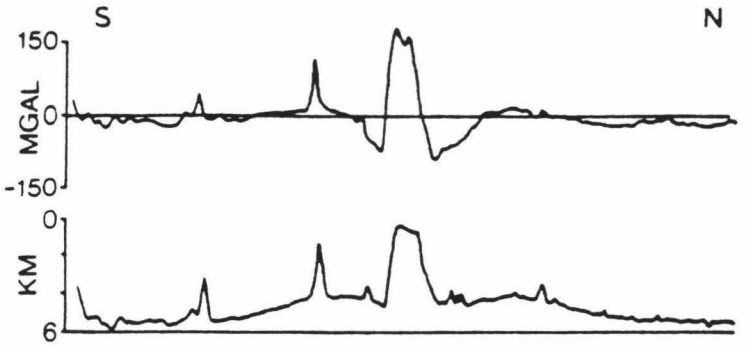

FIGURE 22. Bathymetric and free air gravity profiles across the Hawaiian ridge near Oahu showing Hawaiian swell, moat and arch [from Watts, 1976].

bathymetry data [Watts, 1978]. Flexural rigidity is a measure of the stiffness of the lithosphere and determines the wavelength and amplitude of flexure [Watts, 1978]. Flexural rigidity is determined by the elastic thickness.

Watts [1978] established that elastic thickness depends on crustal age. Elastic thickness is fixed at the time of loading and does not change significantly with time [Watts et al., 1980]. Small elastic thicknesses are associated with loads on young lithosphere while large thicknesses are calculated for older lithosphere. As oceanic lithosphere ages, it thickens and cools, therefore responding more rigidly to surface loads. By comparing computed gravity anomaly profiles for different elastic thicknesses with observed profiles to determine the actual elastic thickness (Figure 23), Watts et al. [1980] determined the age of the lithosphere at time of loading. In this manner, it is possible to estimate whether an island or seamount was formed on young lithosphere (near the ridge crest) or old (off the ridge) (Figure 24). Estimates of the distribution of volcanism can then be made (i.e., for the Pacific plate since the Jurassic (Figure 25) [Watts et al. 1980]).

McNutt and Menard [1978] discuss how growth of a young volcano flexes the sea floor and affects the apparent sea level on nearby atolls. Figure 26 shows atolls sinking with normally subsiding oceanic crust. A growing volcano flexes the lithosphere, uplifting the atoll on the arch while lowering the one in the moat. This explains how some

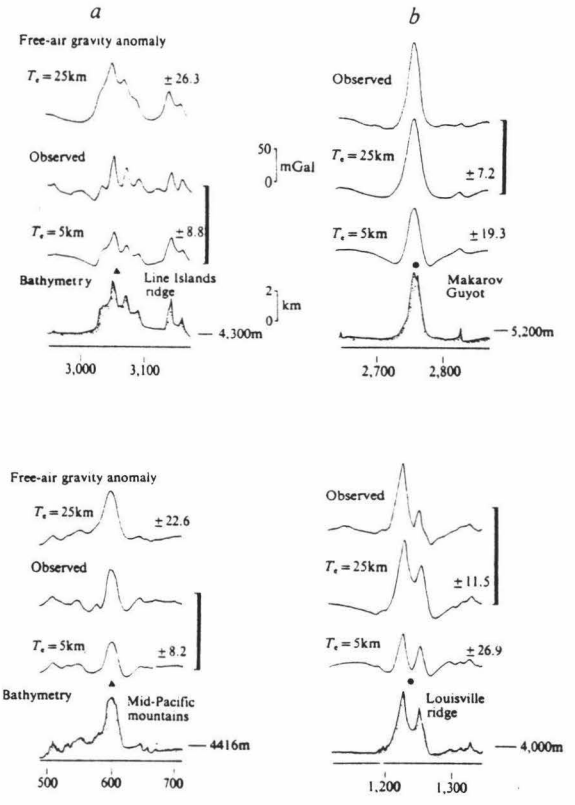

FIGURE 23. Comparison of observed free-air gravity anomaly profiles with computed profiles based on the elastic plate model and assumed values of the elastic thickness Te = 5 km and 25 km [from Watts et al., 1980]. a) Line Islands ridge at 1.7° N, 157° W and Mid-Pacific mountains at 18.5° N, 179.5° W. The observed profiles can best be explained by the computed profile of Te = 5 km. A ridge crest origin is concluded for these. b) Makarov Guyot at 29.6° N, 153.5° E and Louisville ridge at 39.3° S and 167.5° W. The observed profiles are best explained by the computed profile of Te = 25 km. Therefore, an off-ridge origin is deduced. The numbers at the right of each computed profile are the r.m.s. differences between observed and calculated gravity anomalies and the number below each bathymetric profile is the distance in nautical miles along a ship track, used to locate the feature.

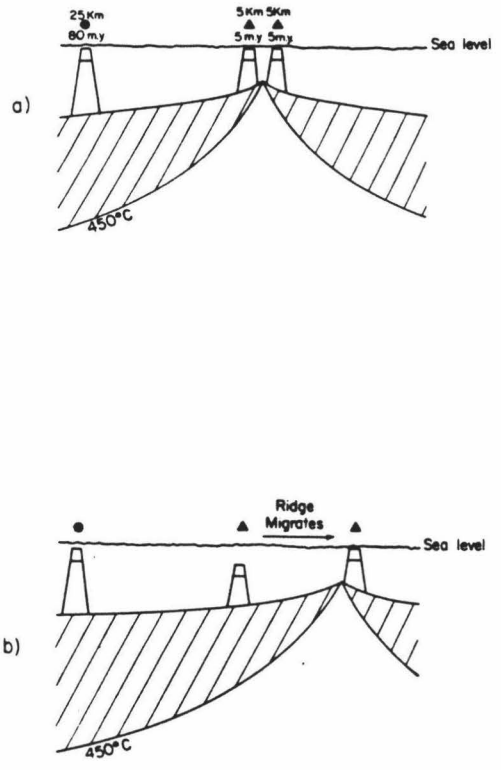

FIGURE 24. Schematic model [from Watts and Ribe, 1984] illustrating a) that seamounts formed on or near a mid-ocean ridge crest are associated with low elastic thicknesses (Te), while seamounts formed off ridge have high values. b) As the ridge axis migrates and the lithosphere ages, values of Te are not expected to change appreciably with time. The value of Te provides information on the tectonic setting of seamounts.

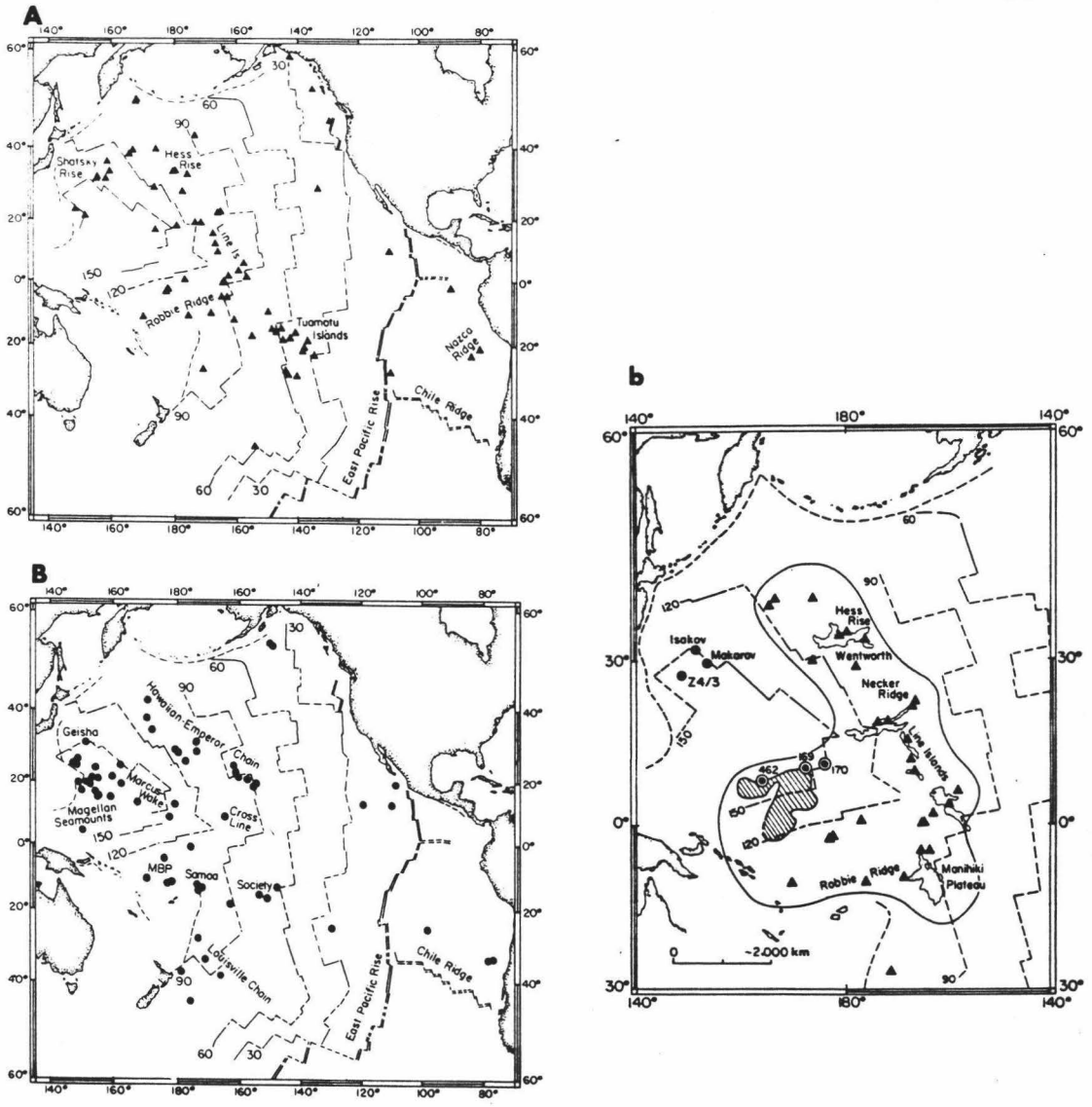

FIGURE 25. Maps from Watts et al. [1980] a) showing the distribution of volcanoes formed on young (A) versus old (B) lithosphere based on gravity and lithospheric flexure studies, and b) summarizing the inferred distribution of volcanism on the Pacific plate during the interval 90-120 Ma. Triangles represent features formed at the ridge crest; circles show features formed off-ridge.

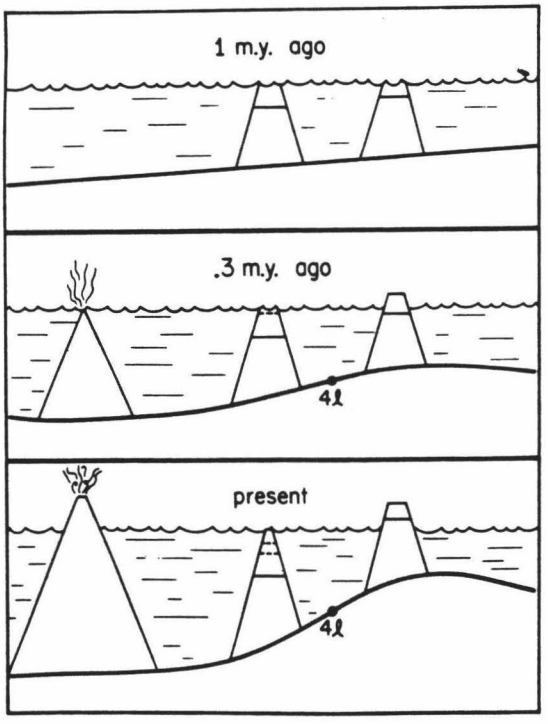

FIGURE 26. Model of apparent sea level change on coral atolls caused by volcanic loading on an elastic lithosphere [from McNutt and Menard, 1978]. The nodal point, l, depends on flexural rigidity.

atolls in an area are uplifted while most in the same area are not. The distance of the nodal point, indicated on the figure, from the volcanic load depends upon the flexural rigidity. Atoll uplift, therefore, can be used to determine the flexural rigidity of the oceanic lithosphere. However, unreliable measurements might arise if sea level was higher during previous interglacial periods or there was rapid erosion after emergence [McNutt and Menard, 1978].

Excessive subsidence of atolls and seamounts has been documented. Proposed causes include: 1) isostatic adjustments to the weight of the volcano or coral reef cap, 2) viscoelastic flexure of underlying lithosphere, and 3) subsidence following volcano formation on anomalously shallow regions, or swells, of the sea floor [Detrick and Crough, 1978]. Although isostatic adjustments would explain the high subsidence rates observed and may account for some of the subsidence [Watts and Cochran, 1974], a volcano should be completely compensated almost as soon as it is built, assuming time scales of isostatic adjustments are the same as those for the continents [Detrick and Crough, 1978]. Viscoelastic flexure involves the lithosphere responding to loading by viscous flow. Watts [1978] showed that this mechanism could not explain gravity and bathymetry data from the Hawaiian-Emperor seamount chain, and presumably, similar seamount chains. Detrick and Crough [1978] proposed that volcanoes form atop swells

- high, wide, anomalously shallow regions often elongate in form [Crough, 1983]. As the swells return to normal depths, the volcanoes subside. Topographic swells have been found to be a major morphological feature of the sea floor. Detrick and Crough's [1978] suggestion becomes even more plausible upon discovering that these swells are quite often coincident with volcanic edifices. In fact, almost every oceanic volcano sits atop a topographic swell [Crough, 1983].

The origin of such swells is still uncertain. If the Hawaiian Swell is taken as a typical example of such a feature, any proposed mechanism must be able to explain the following observations [Von Herzen et al., 1989]: 1) rapid uplift of the swell, 2) the gradual disappearance of the swell after passing over the hotspot, 3) the lack of a notable heat flow anomaly over the older part of the swell, and 4) the apparent compensation of the swell at depths > 50-100 km (within or below the lower part of the thermal plate) [Crough, 1978].

Previous evidence has led to suggestions of a thermal origin involving substantial reheating of the lower part of the lithosphere. The compensation depth obtained by Crough [1978] was consistent with the amount of lithospheric thinning needed to explain the initial uplift and gradual subsidence of the swell using a simple reheating model [Detrick and Crough, 1978]. The apparent gradual increase in heat flow over the older part of the swell [Von Herzen

et al., 1982] was also consistent with reheating of the lower part of the lithosphere. However, Von Herzen et al. [1989] have discovered that the magnitude of the heat flow anomaly is much less than originally thought. This severely hampers proposed mechanisms of origin of swells which invoke high temperature material close to the surface. The subsidence rates are explained adequately but the absence of high heat flux is not. Von Herzen et al. [1989] suggest that dynamic support of swells by plume-related convection offers the best explanation for the observations discussed earlier. In such a model, the upper part of the lithosphere behaves rigidly, acting as a "conducting lid", while the lower portion can deform ductily and take part in the flow [Parsons and McKenzie, 1978]. A rising mantle plume can penetrate and replace lower lithosphere and underlying asthenosphere which has been cooled conductively with hotter, bouyant mantle material [McKenzie et al., 1980; Parsons and Daly, 1983]. The swell is supported by the uplift from dynamic convection and the thermal expansion of the overlying conducting lid [Von Herzen et al., 1989].

The convective model described above can account for the general shape of the swell but not the shallow depth of compensation, nor the elastic plate thickness. However, coupled with a low-viscosity zone in the upper mantle to simulate a partial melt, Robinson and Parsons [1988] showed that the convective model can explain the observations.

The low-viscosity zone would allow lateral flow at the top of the rising mantle plume to entrain the lower lithosphere material and to sweep it away. This process could explain the rapid uplift of the swell. The shallow compensation depth of the swell can be explained by mantle convection in the presence of a low-viscosity zone since effective temperature changes would be concentrated near the base of the conducting lid [Robinson et al., 1987]. Also, the buffering effect of partial melting on mantle temperatures may explain the low heat flux over the swell. Any excess heat may be released through volcanism and crustal thickening over the central portion of the swell [Von Herzen et al., 1989].

SEDIMENTATION AND SEDIMENT TRANSPORT

Sedimentation is an important component in the morphologic development of seamounts. On older lithosphere sediment can completely bury smaller volcanoes. In less extreme cases, sedimentation can modify the apparent slopes on seamounts and mask the features on their summits. Sediment tends to make slopes less steep and will bury interesting features like summit craters or satellite cones. Sedimentation can even affect heat flow readings [Von Herzen et al., 1989].

A variety of sediment types are found on seamounts, including volcanogenic, lithogenic, hydrothermal, biogenic

and authigenic. Variations in deposition and removal of these materials are the result of differences in volcanism, biological productivity, current action, bioturbation and hydrothermal activity, which can lithify sediment in situ to form crusts [Levin and Nittrouer, 1987; Stanley and Taylor, 1977].

Levin and Nittrouer [1987] discuss how sediment character (texture, composition, color) is influenced by environment. Latitude, water depth and age affect sediment supply and removal through changes in biologic productivity, carbonate dissolution and hydrothermal precipitate production. In high latitudes with areas of high productivity, the supply of foraminifer sand-sized particles to the sea floor increases. As water depth increases, carbonate dissolution generally increases; therefore, the removal of foram sand-sized particles from the sea floor also increases. Young seamounts that are active or were recently active commonly have more hydrothermal and volcanic sediment exposed. Older seamounts have greater sediment cover and lack surface hydrothermal precipitates.

Different settings within seamounts affect sediment accumulation (Figure 27) [Levin and Nittrouer, 1987]. Sediment supply to seamounts occurs mostly as pelagic fallout; hence, the interiors of calderas and pit craters, areas of weak current activity, are effective sediment traps. The coarser deposits are found on topographic highs

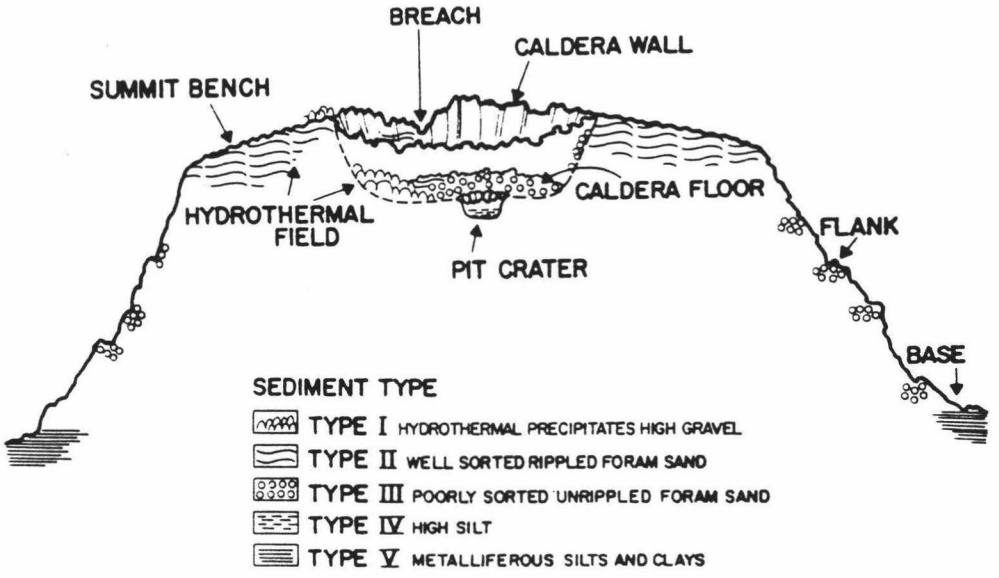

FIGURE 27. Schematic diagram of topographic settings and generalized sediment types on a typical young seamount in the eastern Pacific Ocean [from Levin and Nittrouer, 1987].

(summits) where current activity winnows out finer materials. Finer sediments are found at the base of seamounts where carbonate dissolution is greatest, provided the carbonate compensation depth is exceeded, and winnowed sediments accumulate.

Physical and biological activity cause smaller scale variations in sediment texture and distribution [Levin and Nittrouer, 1987]. Bedforms such as ripples concentrate different grain sizes within different parts of their waveform. Organisms redistribute sediments by bioturbation or selective use of certain sediments in the formation of tests. Faunal abundances are greatest in calderas, pit craters and on summit benches while the lowest are at the base and in hydrothermal fields of seamounts [Levin and Nittrouer, 1987].

Rates of sedimentation vary in different parts of the ocean. Therefore, the effect of sedimentation on morphology will depend on the location of the seamount. Rates are lowest (< 1 cm/1000 yrs) in the deepest parts of the oceans. Intermediate rates (1-3 cm/1000 yrs) are found in the shallower oceans, on mid-ocean ridges and in high latitudes where there is high biogenic productivity [Kennett, 1982]. The highest rates (10-30 cm/1000 yrs) are found at continental margins, inland seas, abyssal plains and in the North Atlantic.

Sea level influences sedimentation rates. Rates are higher in the deep sea during times of low sea level

[Davies and Worsley, 1981; Rona, 1973]. During low sea level stands, continental shelves are exposed, so the eroded materials from the continents are flushed to the deep sea. During high stands, these materials would be deposited on the continental shelf. Davies and Worsley [1981] also pointed out that during high sea level, there is more biogenic precipitation on the continental shelves, starving the ocean basins.

Sediment can be transported downslope or across slope. Cross-slope movement is accomplished mainly by currents. Downslope movement is accomplished mainly by gravity related flow processes including debris flows and creep.

Stanley and Taylor [1977] studied sediment transport processes on the twin-peaked Gilliss Seamount in the North Atlantic. Their observations are similar to those from other seamounts. Detailed bathymetry of the Gilliss Seamount shows a step-like topography formed by steep scarps alternating with ledges. Lonsdale et al. [1972], as discussed previously, interpreted similar terraces on the Horizon Guyot as a result of primary volcanic processes. The sediment on the ledges is driven by currents, as indicated by ripples. As the traction mode nears the edge of the ledge, spill-over occurs. The material is then transferred down the steep scarps by gravity-driven processes (Figure 28). At the base of the scarp, the sediment is once more open to entrainment as part of the traction carpet. The sequence is repeated until the

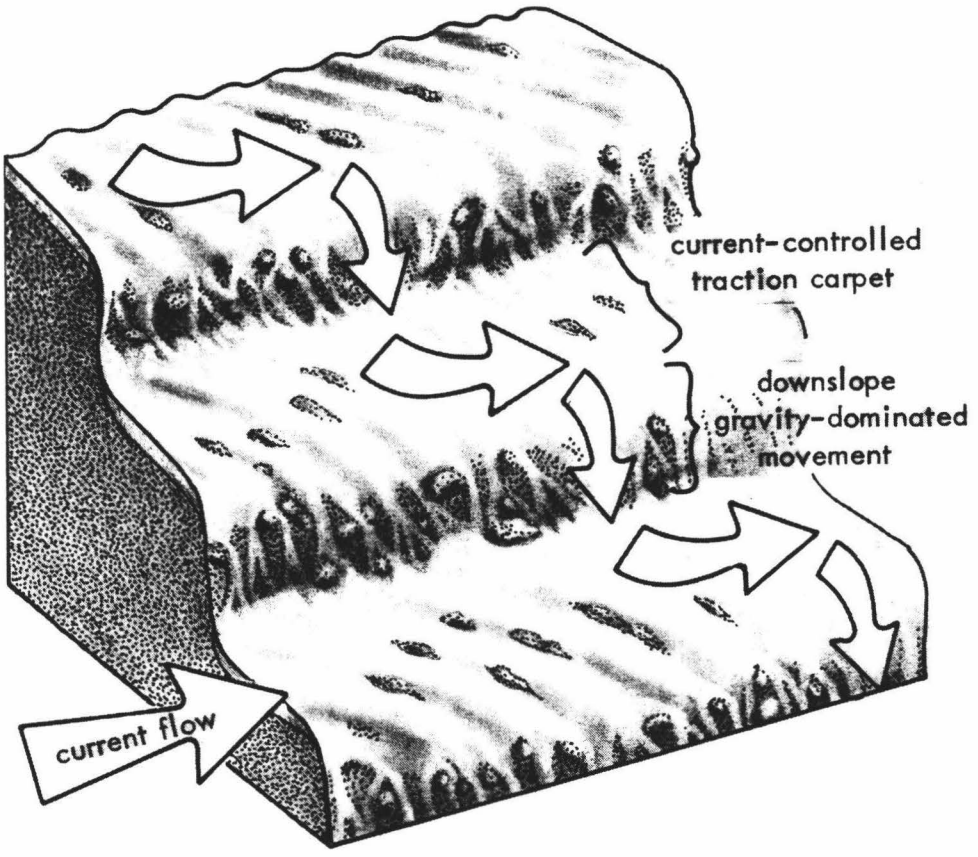

FIGURE 28. Schematic diagram of proposed current traction-gravity transport model [from Stanley and Taylor, 1977] of down flank sediment movement.

sediment reaches the base of the seamount. At this point, gravity flow is no longer an important factor, but bottom currents continue to modify the accumulating sediment. This progressive downslope movement explains the lack of significant sediment accumulation on the upper flanks of seamounts.

The lower flank slopes of seamounts consist mainly of sediment aprons. These aprons, or cones, or fans, surrounding the base are generally small, but increase greatly in area and volume once the guyot state is reached. Menard [1956] stated that these aprons were probably composed of a mixture of volcaniclastics, shallow water bioclastics and pelagic sediment transported from the upper slopes of the seamounts by slumps and debris flows. The crenulations typically seen in bathymetric contours of the lower slopes of ocean volcanoes represent slump fronts and channels carved by debris flows (Figure 29).

In order for large aprons to develop, it is necessary for the volcanic vent to approach the sea surface. More clastic debris can be formed and rock density decreases because vesicularity increases due to lower confining pressure. This begins at about 1 km depth and accelerates as the vent approaches a few 100 m of the surface [Vogt and Smoot, 1984]. The importance of producing more clastic debris is obvious. Decreased rock density is helpful in producing large aprons because material can be entrained

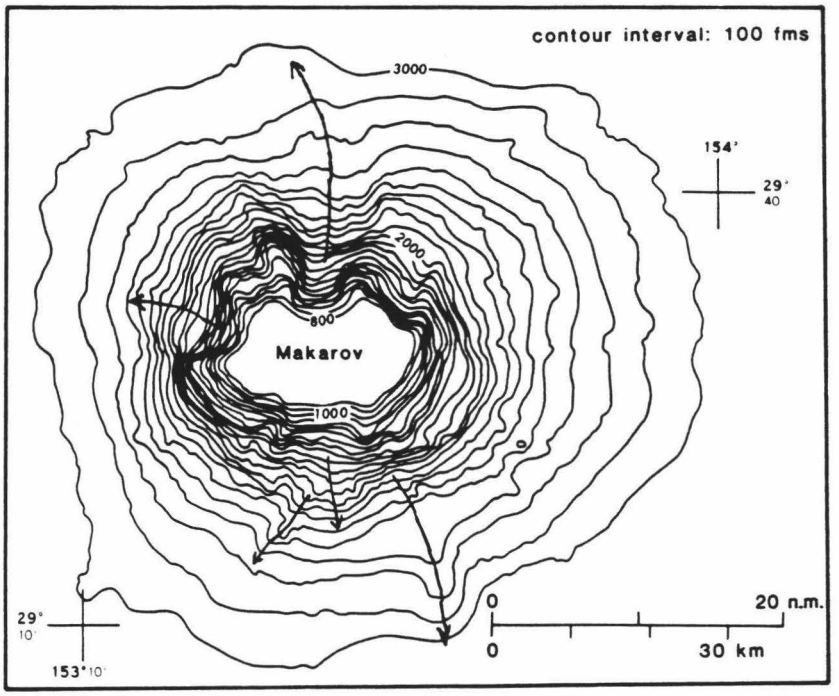

FIGURE 29. Detailed bathymetry of Makarov Guyot (100 fm = 183 m contour interval) [from Vogt and Smoot, 1984]. Arrows show paths of some major debris flows.

for longer periods and can be deposited farther from the base of the volcano.

One effect of large aprons is to alter heat flow. Rapidly deposited cold sediments can lead to a reduction in the observed surface heat flux, while radioactive heat produced by the sediments increases it. Hutchison [1985] discussed the affects of sedimentation rate, type and depth of burial on heat flux observed. High sedimentation rates reduce the flux. The response of the surface flux is rapid, but after deposition stops, the system gradually recovers. Highly conductive sediments such as salts, evaporites and sandstone affect the heat flux the least, while low conductivity, low porosity materials like limestone affect it the most (Figure 30). Thermal diffusivity increases with depth of burial due to sediment compaction.

CURRENT ACTION

Ocean currents affect a variety of processes which, in turn, affect the morphology of seamounts. Surface currents are intimately involved with sedimentation rates, coral growth and formation of ocean bottom currents. The circulation patterns of surface waters and bottom and intermediate waters differ greatly. Surface waters have narrow latitudinal ranges very similar to climatic belts. Surface currents are primarily wind-driven. Deeper

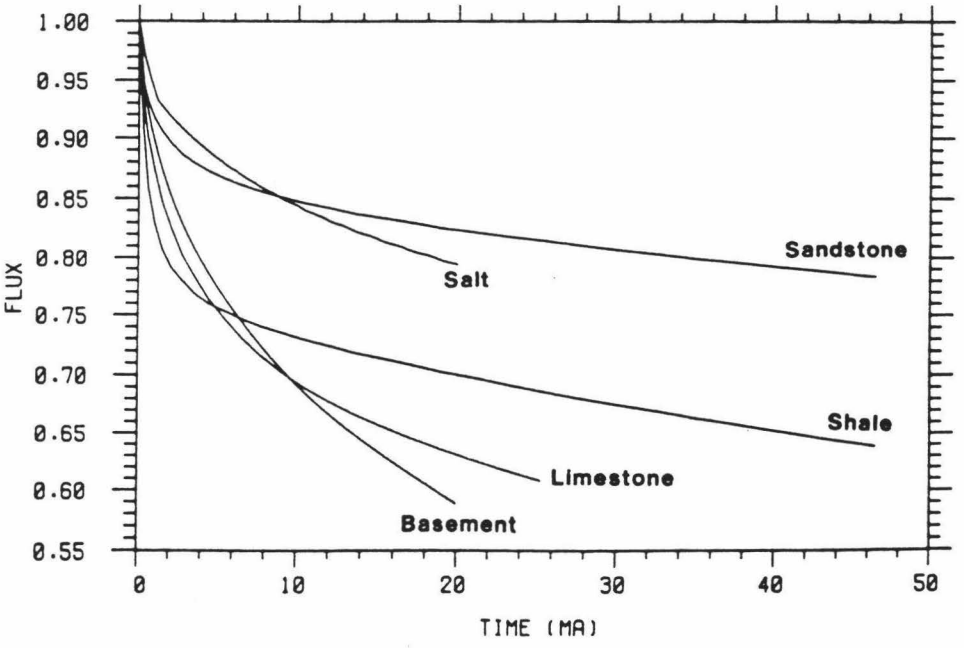

FIGURE 30. Comparison of the alteration to the surface heat flow due to the deposition of salt, shale, sandstone and limestone [from Hutchison, 1985]. Each curve accounts for 10 km of deposited material.

circulation patterns originate from surface processes, then spread widely through the water column [Warren, 1971]. The dominant process involved in these deeper currents is gravity-driven thermohaline circulation.

Although precise directions, longevity and intensities of ocean bottom currents are not well known, they are known to exist. Swallow [1971] discovered deep-sea currents of 5-10 cm/sec that completely change direction within the space of a month. Intensities can be inferred by observing the following: the extent of winnowing of sediment, current modification features (ripples, sediment scour, etc.), and the prescence of organisms [Stanley and Taylor, 1977]. Current direction can be determined in some cases, such as from asymmetric ripples and current tails.

Deep ocean current velocities are periodic. Semidiurnal and monthly tidal variations have been recorded (Figure 31) [Kennett, 1982]. The effect of tidal energy is greatest in shallow seas and on continental margins. In times of lower sea level when continental shelves are exposed, tidal energy is a greater factor in the deeper ocean. Tidal currents are known with velocities up to 17 cm/sec just above the sea floor on seamounts [Kennett, 1982].

Currents have been shown to be affected by seamount topography. Submarine topography can change current direction and velocity. Flow is accelerated over the peaks of seamounts [Genin et al., 1986]. The faster currents not only are capable of entraining more sediment, but also

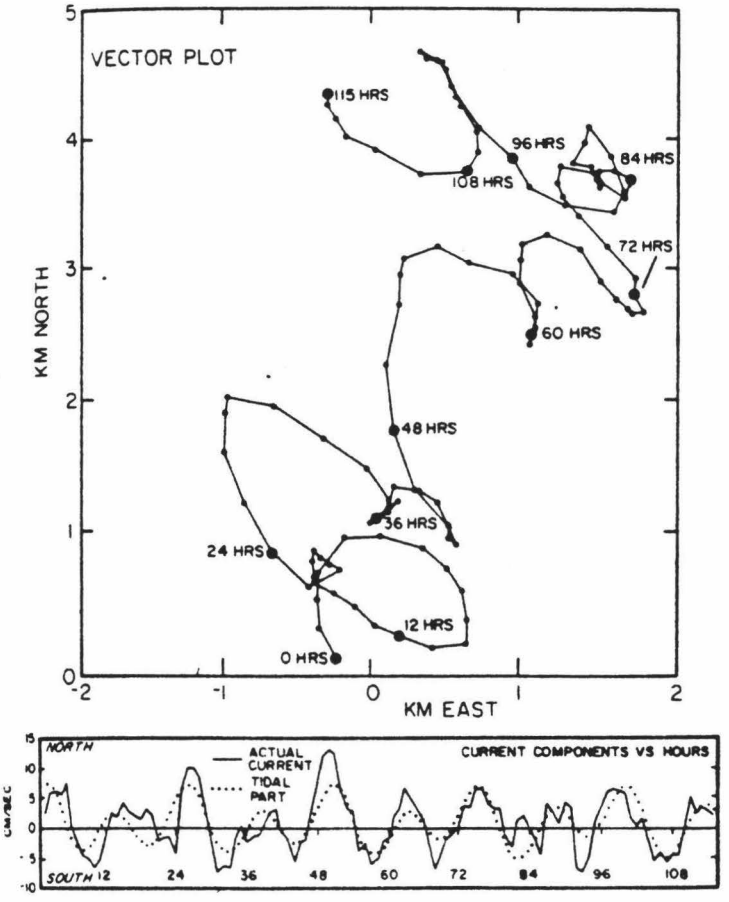

FIGURE 31. Sample plot of current meter data to show tidal periodicities in the current [from Lonsdale et al., 1972].

enhance biogenic production and coral growth (Figure 32), at depths where growth is possible, by providing more nutrients. Coral growth will be discussed in more detail in a later section. This current acceleration is another explanation for the tendency to have a thinner sediment cover on seamount summits than on the flanks. In addition, it affects the type of sediment and grain size found [Levin and Nittrouer, 1987]. More biogenic sediments are found in areas of higher nutrient content due to the greater productivity. Where currents are strong enough to winnow fine sediments (over seamount summits) coarser lag deposits are found.

Where currents are forced to divert around seamounts, erosion and deposition of sediments is affected. More erosion will occur where the current first encounters the obstruction, while deposition will occur on the lee side. This will affect the appearance of the volcano.

EROSION AND MASS WASTING

Erosion is a powerful influence on the morphology of any geologic landform. Seamounts are no exception. Whether near the ocean surface or deeply submerged, erosion can affect the shape of any edifice. On near surface seamounts, erosion by ocean surface currents, wave action, bioturbation, mass wasting and in some cases, subaerial erosion may occur. On deeper seamounts, erosion is

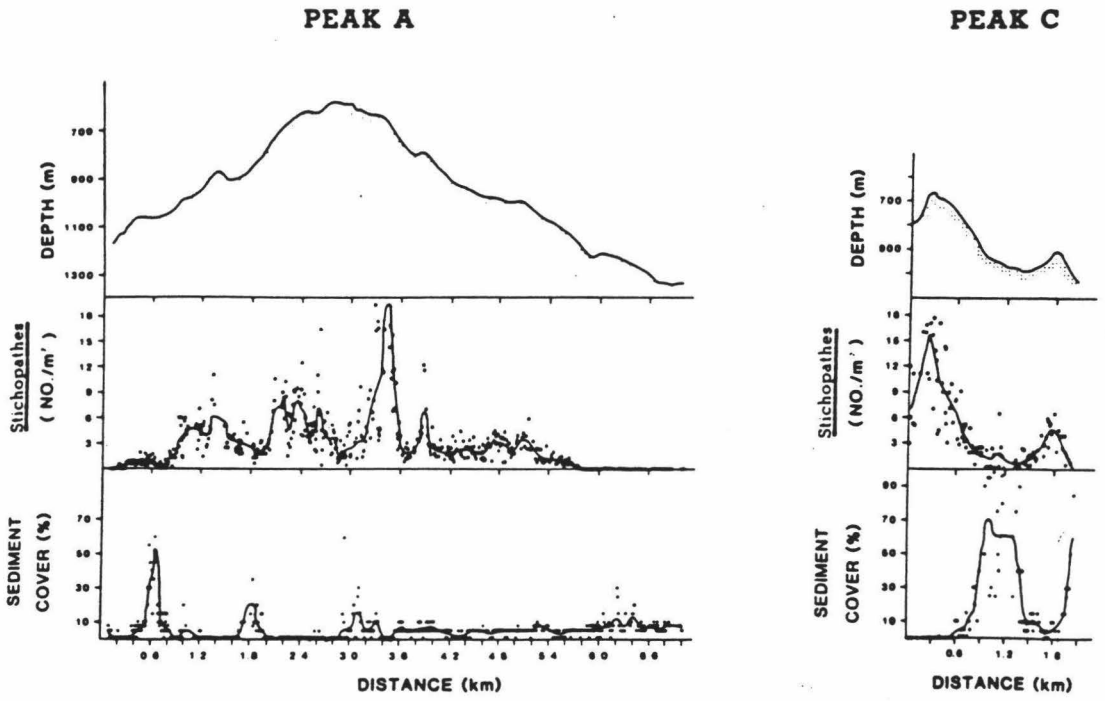

FIGURE 32. Bathymetry, densities of Stichopathes and sediment cover across two satellite peaks on Jasper Seamount [from Genin et al., 1986]. Each dot indicates the animal density or sediment cover in a single photograph. Note that animal densities follow the bathymetric line on the sharp peak (C) whereas lower densities are found near the center of the wide Peak (A) than near its edges. Animal densities are relatively higher on small topographic prominences. Note the sharp increase in sediment cover in the depression near peak C.

accomplished by bottom currents, dissolution of sediment, bioturbation and mass wasting.

Malahoff et al. [1982], suggested that slumping is typical on seamounts and guyots. Indeed, major landsliding is apparently an important factor throughout the growth of oceanic volcanoes, continuing even after dormancy [Moore et al., 1989]. Some of the largest landslides occur near the end of the shield-building stage when volcanoes are active and vigorously extending their shorelines. However, during the entire shield-building stage, intermittent mass wasting events probably occur, but the evidence is obscured by incorporation of the landslide debris into the edifice as it grows [Moore et al., 1989].

Many slope failures on Hawaiian volcanoes display movement perpendicular to the primary rift zones of the volcano, or head on the sides of long, shallow submarine ridges which are most probably submerged rift zones [Moore et al., 1989]. There is a cause-effect paradox at work here. Rift zones form along zones of tension at the head of landslides, but landsliding can also be triggered by the lateral motion caused by magma injection into the rift zones [Moore et al., 1989].

Continued mass wasting after the cessation of volcanic activity, could provide an alternative explanation to flank rift zones (discussed in a previous section) for the starfish shape of some volcanoes. The pattern of radial arms could represent unslumped residual ridges, the remains

of a more extensive volcano (Figures 7, 29). On the other hand, the mass wasting may simply remove debris from between the rifts, made more resistant by cores of dikes. This would expose flank rift zones previously embedded in the edifice.

Erosion is responsible for such striking morphological features as flat-topped guyots. Guyots are seamounts that were truncated by erosion at the ocean surface [Menard, 1964]. Ideally, guyots are perfectly flat-topped with no summit plateau relief. Achieving such an ideal state requires shoreline erosion rapid enough to negate thermal or other subsidence. In addition, there can be no differences in the erodibility in the rocks of the edifice; otherwise, resistant knobs and shallow depressions may be formed [Vogt and Smoot, 1984].

However, the summits of most guyots are not ideal. Generally, the observed summit relief increases with increasing summit area and a decrease in thermal age and erosion rate. The summit area versus summit relief relation reflects the importance of shoreline erosion. On such near surface seamounts, erosion can truncate smaller seamounts faster than large ones [Grigg and Epp, 1989]. (This is discussed in more detail in the next section.)

The importance of erosion cannot be denied. Menard [1983] discussed the role of erosion in isostasy. He stated that the principal factors which influence vertical movement of volcanic islands are: thermal subsidence of

the underlying crust (at a rate proportional to the square root of time), eustatic sea level changes, and isostasy. Isostatic effects result from compensation for thermal subsidence, eustatic fluctuations, loading by coral growth (minimal due to the small density contrast between coral and water) and unloading by erosion. According to Menard [1983], the most important isostatic effect is erosion, which is greatly influenced by the presence or absence of barrier reefs (to be discussed in the next section).

On near surface seamounts, there are two main types of erosion - wave and river. The relative importance of these types of erosion depends upon the radius of the island. The rate of wave erosion varies with perimeter while the rate of river erosion varies with area. Smaller islands tend to be eroded more by waves, while large ones are more eroded by streams [Menard, 1983]. This is reinforced by the influence of height on rainfall. The higher the mountains, the higher the percentage of precipitation and the greater the amount of erosion. Windward sides of high islands can be eroded up to 30-40 x faster than the lee side. This can be seen on the island of Kauai where once the windward side was eroded, rainfall centered on the lee side and deep canyons were cut [Menard, 1983].

Subsidence combined with wave and river erosion affects morphology and distribution of off-lying volcanic islands. In cases where thermal subsidence is slowed by erosion but not balanced, wave erosion may form a series of narrow

terraces separated by cliffs; or a relatively smooth shelf that is steeper near the shelf break than in the interior (Figure 33) [Menard, 1983]. On large tropical volcanoes where river erosion has carved out ridges and spires, subsidence causes the narrow saddles between spires to disappear and leave small outlying islands.

Erosion is affected by the rate of flow of bottom currents and the corrosiveness of the bottom water to biogenic sediments [Kennett, 1982]. Current activity can lead to oversteepening of sediments on seamount flanks which, in turn, may lead to slumping [Levin and Nittrouer, 1987]. Erosion by currents can also form moats (Figure 34) or accentuate those formed around seamounts as a result of lithospheric flexure. The longer the biogenic sediment is exposed to the bottom water with no deposition occurring, the greater the possible dissolution of the sediment.

REEF CAP GROWTH

Coral reef caps form on some seamounts and serve as modifications to the morphology. They often lend a flat-topped look to seamounts which are termed guyots (Figure 35). They can influence the erosional history of oceanic volcanoes: a reefless volcano will erode faster than one with a protective reef. Reefs may trap erosional debris, thus affecting subsidence due to loading, which in turn

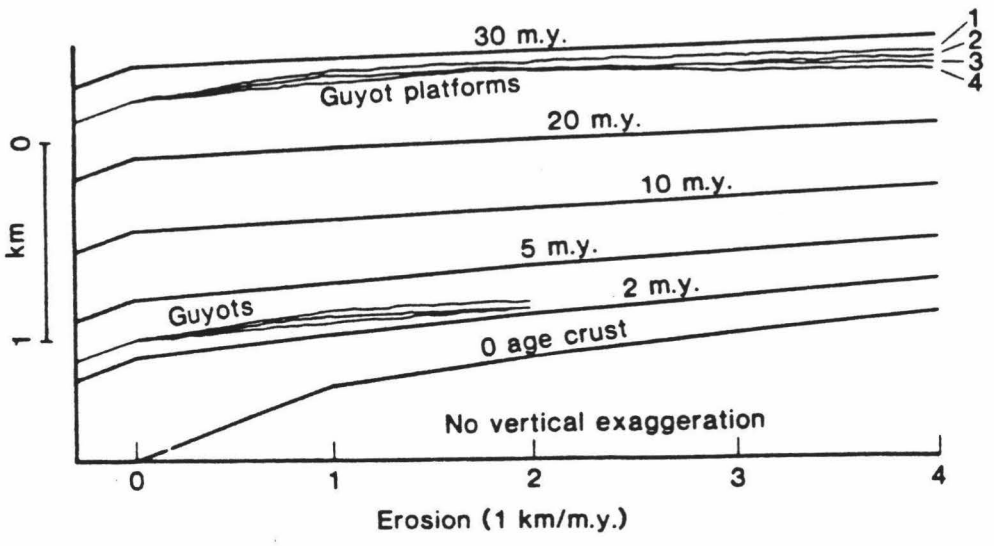

FIGURE 33. Profiles of eroded basement summits of four small guyots in the Gulf of Alaska compared with theoretical shapes produced by shelf widening at 1 km/my and thermal subsidence at different equivalent thermal ages [from Menard, 1983]. Note the smooth shelves are steeper toward the shelf break than in the interior.

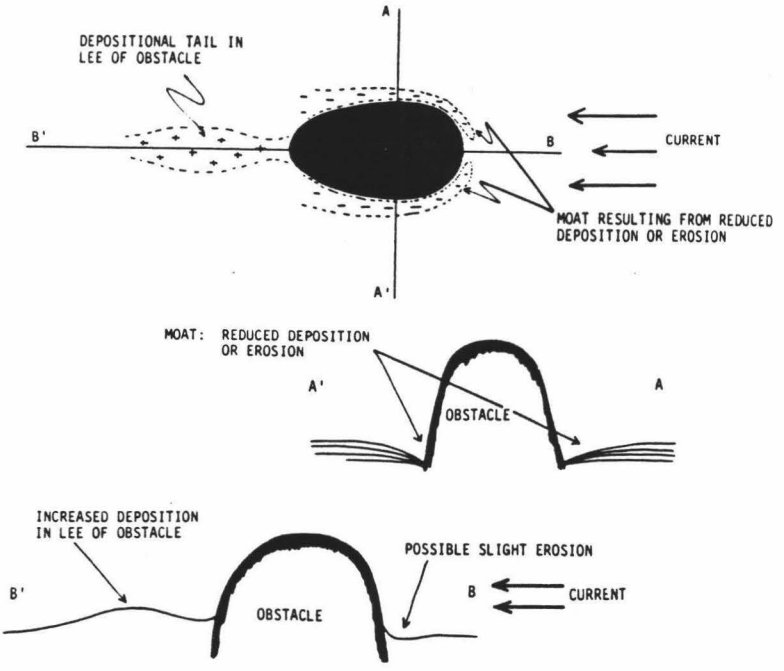

FIGURE 34. Schematic diagrams showing the formation of moats by bottom currents [from Davies and Laughton, 1972].

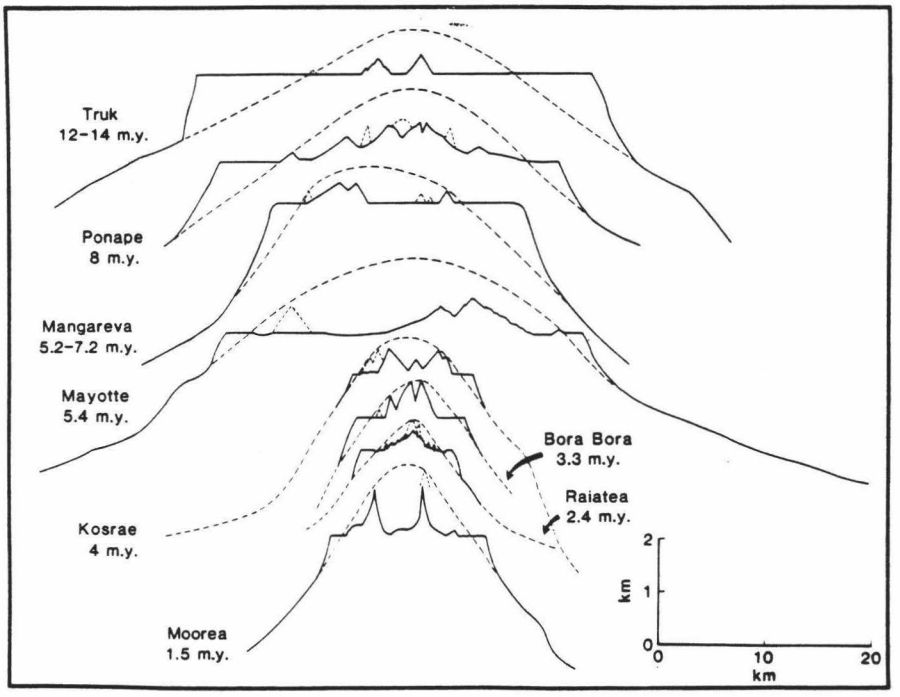

FIGURE 35. Morphology of dated oceanic volcanoes with barrier reefs [from Menard, 1983] showing the typical flat topped appearance of guyots. Short dashed lines indicate relief interpolated into profile, and long dashed lines represent assumed subaerial and probable relief buried under reefs. Vertical exaggeration, 5 x.

affects the erosional/ depositional history. Reefs are important not only because they contribute to shaping seamounts, but they can also be used to study sea level changes and tectonic processes (subsidence and uplift).

The maximum upward growth of coral reefs is about 10 mm/yr [Grigg and Epp, 1989]. This rate applies in areas of optimum growth for corals, at depths of 5-10 m and at low latitudes below the Darwin Point. The Darwin Point, presently at about 29^{o} [Grigg, 1982], is the latitude at which reefs cannot grow upward fast enough to keep pace with subsidence of the edifice. It has varied from 27^{o}-31^{o} over the past 20 my [Rotondo, 1980]. Below a critical depth, coral reefs are unable to maintain a net positive rate of upward growth. Growth rates decline very quickly below the critical depth. For example, at 30 m below sea level, growth rates are 15%-40% of their maximum [Grigg and Epp, 1989]. If growth is unable to keep up with subsidence, the reef will drown. The depth at which drowning will occur is between 30 and 40 m. It could be less depending on variations in light, temperature, sedimentation, turbidity and erosion. Some corals can survive at greater depths, but cannot build to the surface.

Genin et al. [1986] observed that the abundance of coral varied with seamount topography. For instance, on narrow peaks, corals are more abundant on the crest; on wide peaks, they are more abundant at the edge of the crest; and on knobs and pinnacles, abundance increases. It was

suggested that the cause was accelerated currents over the peaks. This provides higher fluxes of nutrients to the corals and benefits their growth (Figure 32). Indeed, modern corals are known to depend upon breaking surf, up to a limit, thus preferring the windward edge of an island [Vogt and Smoot, 1984].

In fact, current acceleration, up to a limit, over topographic features may increase local populations of all suspension-feeding organisms. In addition, topographically induced upwelling may contribute to particle flux on the benthic layer. The eastern tropical Pacific is characterized by a shallow mixed layer and a pronounced oxygen minimum. Low plankton abundances are associated with oxygen minimum zones in the water column. Such zones, if sufficiently broad vertically, serve as effective barriers against plankton. The consumption of particulate matter in these regions is reduced, thus increasing the supply of undegraded organic material reaching the sea bed [Wishner et al., 1990]. Sharp benthic zonations may result due to the enhancement of the food supply and the exclusion of hypoxia-sensitive organisms, as seen on Volcano 7 [Wishner et al., 1990].

The subsidence of an island depends on its size and the presence of reefs [Menard, 1983]. Islands with barrier reefs sink as though on thermally youthful crust, regardless of actual age (Figure 36). Isostatic uplift is eliminated because the barrier reefs prevent wave erosion

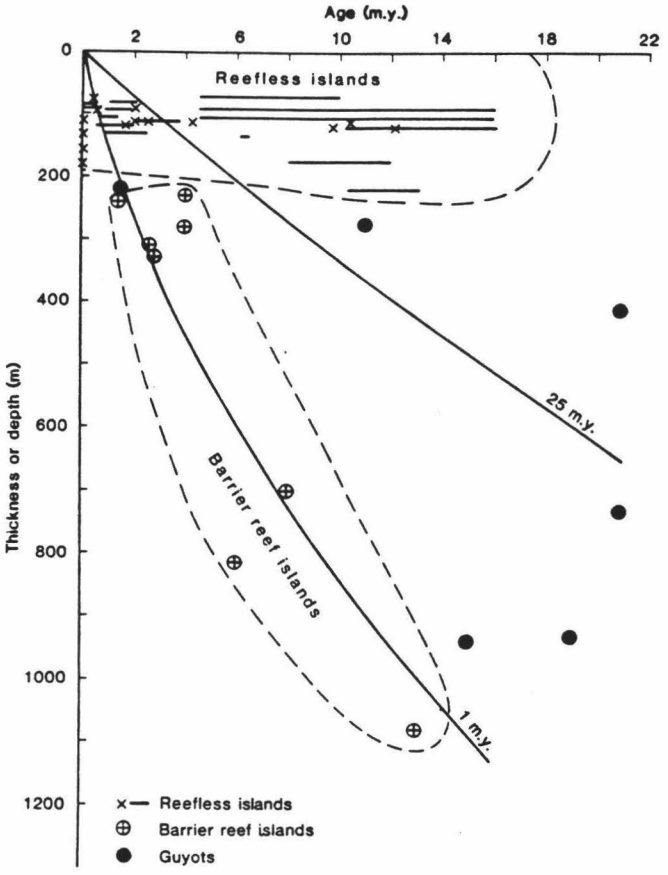

FIGURE 36. Comparison of subsidence of barrier reef islands, reefless islands and reefless guyots [from Menard, 1983]. Presumably, guyots remained at sea level, like reefless islands, until truncated and then sank like barrier reef islands of the same age. The 1 and 25 my lines indicate subsidence expected for oceanic crust with these thermal ages.

and capture stream erosion products. Islands with no reefs do not sink until they are truncated by erosion. Apparently, thermal subsidence is compensated by isostatic uplift as a result of erosion.

The morphology of islands is affected by the presence or absence of reefs [Menard, 1983]. The shelves surrounding islands are mostly erosional. As volcanic islands grow, cliffs may form at the same time. But sea cliffs are not found on older islands with barrier reefs. The reef protects the island from further wave erosion while streams erode any existing cliffs. On reefless islands, there are cliffs, sea stacks and the shelf is very rocky.

Embayments form when valleys submerge. These are conspicuous on islands with barrier reefs, but rare or minor on reefless islands [Menard, 1983]. On younger islands with vigorous stream erosion, deltas may fill some bays. On older islands, this is not the case since there is not an adequate supply of sediment.

Reefless islands tend to remain at sea level until almost totally truncated. This is why guyot platforms are smooth, indicating they were stable long enough to be eroded away. The surrounding seafloor continues to sink as it cools while the island is isostatically uplifted. Once the island has been leveled, it subsides along with the seafloor at an equivalent thermal age [Menard, 1983].

The longer a reefless island remains at sea level, the wider its insular shelf will become, assuming late shield-

building or post-erosional stage volcanism does not flow over and reset the width/age relation [Menard, 1983]. Also, the shelf will be wider on the weather side of the island than on the lee side because of greater erosion.

Grigg and Epp [1989] suggest that summit area of the volcanoes upon which reefs form, may be a factor in the success or failure of atolls. Islands with smaller summit areas are eroded to a greater extent during lower sea level stands than those with larger summits. Since such islands are truncated to greater depths, as sea level rises, the growth of corals may not be able to keep pace with the rate of sea level rise. Larger summit areas are not eroded as quickly so can support growing reefs during sea level changes. There are indeed paired atoll-guyots observed, such as Bikini-Sylvania (Figure 37) [Grigg and Epp, 1989]. Bikini is an atoll with a living coral reef, while the smaller and deeper Sylvania is a guyot with a drowned reef.

Obviously, once a coral reef is drowned, it can no longer continue to influence the morphology of the seamount. Unless, of course, there is tectonic uplift of the edifice or sea level falls and the reef is able to reestablish itself.

Coral reefs have been known to come back after having been exposed and killed during low sea levels. During periods of low sea level, subaerial erosion works on the exposed reefs and forms karst features. This lends an uneven, craggy appearance to the summit morphology, as the

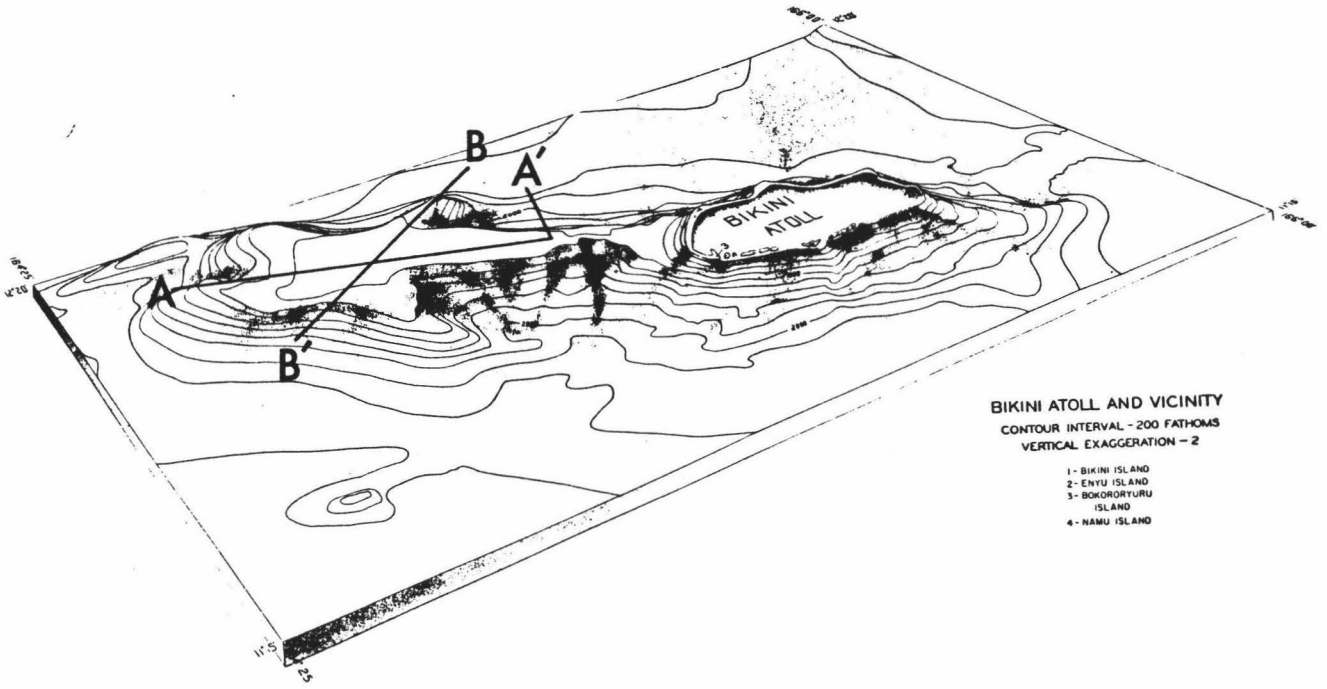

FIGURE 37. Perspective diagram of Bikini Atoll and adjoining Sylvania Guyot [from Emery et al., 1954]. The reef on Bikini Atoll is still living while that on Sylvania Guyot has been drowned.

mid-Pacific Mountains where steep sawtooth profiles are seen [Winterer and Metzler, 1984]. Perhaps this is yet another explanation for Menard's [1964] wave cut platforms.

CHAPTER 3

SEAMOUNT 6 TEXTURAL ANALYSIS

INTRODUCTION

In addition to being able to accurately map structural features of the seafloor, sidescan sonar systems such as SeaMARC II can distinguish areas of differing acoustic backscatter strength. Energy backscattered from any surface outcropping on the seafloor is a function of variables including 1) the composition and roughness of the surface, 2) the slope angle of the reflecting surface and 3) acoustic look angle of the outgoing acoustic energy.

If the important controls on backscatter strength of the seafloor can be quantified, sidescan sonar images, such as produced by SeaMARC II, will come much closer to becoming geologic and lithologic maps of the seafloor. This is important because 100% optical/sample coverage is not possible, even for small areas. To this end, I have undertaken the following study.

The tools used in this study are the acoustic mapping systems SeaMARC II and SeaBeam. My technique was to choose a feature set consisting of statistics measured from backscatter data to and attempt to correlate members of this feature set with observations of geology from bottom photographs. The location chosen for this study is a well-studied seamount in the eastern Pacific - Seamount 6.

Seamounts are ideal for this study since they offer variable slopes and variable geology within a small area. Seamount 6 has been mapped with SeaBeam, has overlapping SeaMARC II coverage, abundant towed camera and submersible photographs, and has been well sampled.

Provided in this chapter, is a brief introduction to the data acquisition system, location of study area, texture features used to describe remotely sensed data and classification methods followed by an application of the analytical techniques to Seamount 6.

SeaMARC II

Remotely sensed data is an important tool in the study of the seafloor. 100% photographic/sample coverage is not possible; therefore, remote acoustic mapping systems are utilized to provide wider swaths of data than produced by one pass of a towed camera, for instance. Acoustic systems are used in seafloor mapping since electromagnetic radiation does not penetrate the water column. The following section is a brief overview of the tools and techniques of seafloor remote sensing used in my study. Specifically, I provide an introduction to SeaMARC II, discussing physical description, data acquisition, how images and bathymetry are created, corrections applied to data and data analysis.

Systems used in the study of the seafloor are multi-beam and bathymetric sidescan sonars. Multi-beam echo sounders, such as SeaBeam, yield high resolution (about 10 m vertical and 100 m horizontal) bathymetric maps. For a complete system description, see Renard and Allenou [1979]. Bathymetric sidescan sonars, such as SeaMARC II, yield high resolution (10 m) acoustic imagery, plus swath bathymetry with 50 m vertical and 100 m horizontal resolution. As SeaMARC II imagery gives high resolution detail, we hope to use this as an analog to aerial and satellite remotely sensed imagery to aid in the classification of the seafloor.

A brief description of SeaMARC II follows. A complete system description can be found in Blackinton et al. [1983]. The SeaMARC II seafloor mapping system (Figure 38) consists of two subsystems. The first produces digital sidescan sonar images by recording acoustic backscatter amplitudes versus time. The second measures the direction of the acoustical returns versus time and converts the angles to bathymetry [Blackinton et al., 1983]. The unit is towed at about 100 m beneath the sea surface for deep ocean surveys to avoid surface sound speed variations and to enhance platform stability. Normal survey speeds are 8-9 kts. The sidescan swath width is limited by hardware to 10 km, while the width of the bathymetry swath is limited to 60^{o} on either side of the towfish.

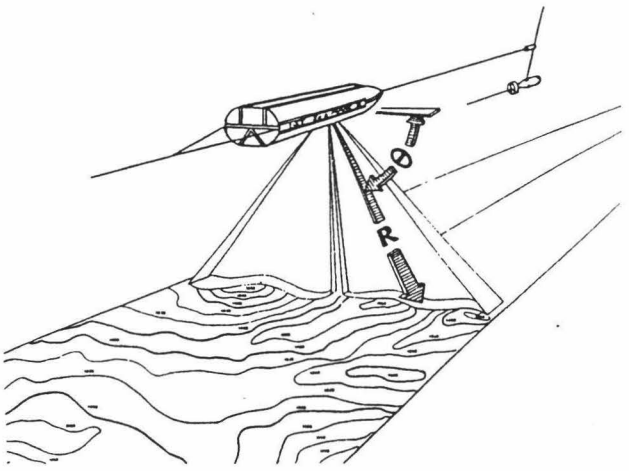

FIGURE 38. Schematic of the SeaMARC II acquisition system [from Bergersen, 1991]. Acoustic backscatter amplitudes are referenced according to arrival angle (θ) and radial distance (R).

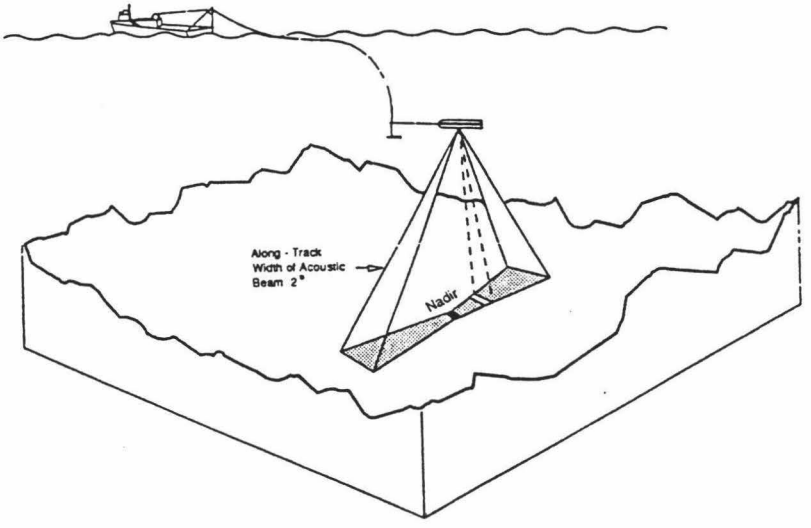

FIGURE 39. Schematic of the acoustic "footprint" of a sidescan sonar system [from Johnson and Helferty, 1990]. The grey area represents the intersection of the beam pattern with the ocean floor. A typical beam width for such a system is 2^{o} along-track.

Beam forming is accomplished by two parallel, inclined sonar arrays on either side of the SeaMARC II towfish. The port arrays operate at a frequency of 11 kHz while the starboard arrays are 12 kHz in order reduce interference of returning signals from either side. The transducer arrays produce a fan-shaped beam about 2^{o} wide along track (Figure 39). Each ping, or outgoing pulse, (in water > 1000 m deep) images a swath 10 km wide across track. The result is a sampling of a bowtie-shaped piece of the seafloor, centered at nadir.

Sidescan sonar images are created as two-dimensional displays of pixels. The image pixels are acquired from the bowtie-shaped swath by dividing the returning signal into increasing intervals of time. For each ping, 2048 pixels, each 5 m across and each with an associated intensity which graphically represent how sound interacts with the seafloor, are generated. Each digitized pixel is represented as an 8-bit word, limiting the range of image intensity values to 256. The middle 80 pixels are discarded since they are generated much too rapidly to be resolved. The result is an image with 984 pixels per ping per side of the ship track.

The intensity value assigned to each pixel depends upon how the acoustic signal interacts with the seafloor. The acoustic return received at the towfish is a combination of backscattered (diffracted) and specularly reflected (as by small mirrors) sound from the ocean bottom (Figure 40).

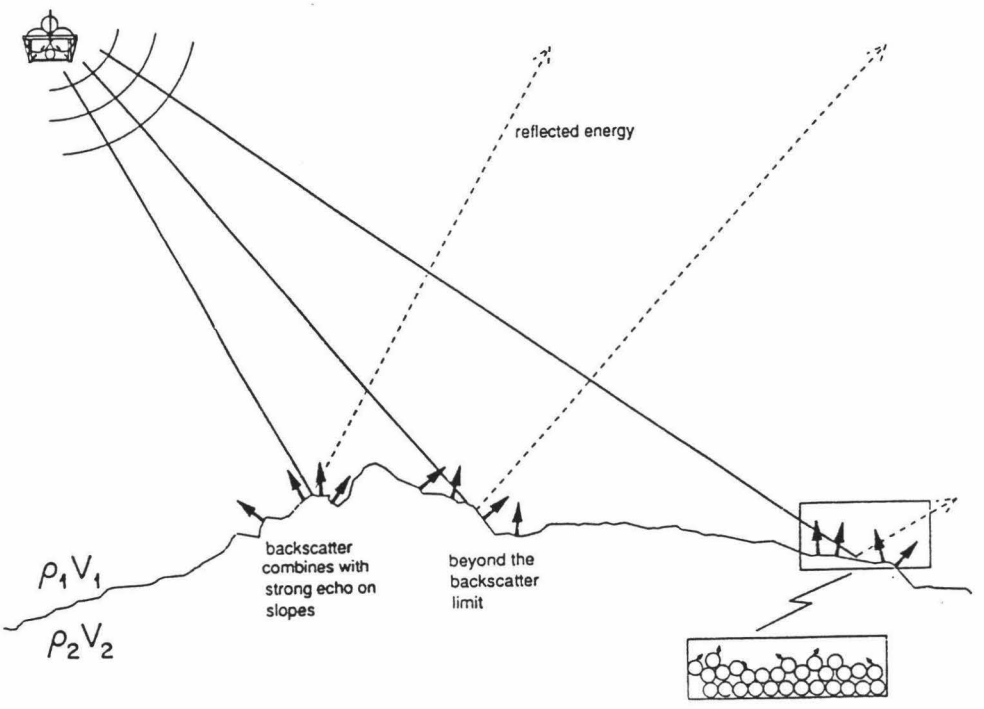

FIGURE 40. Possible results of an outgoing acoustic signal interacting with the ocean floor [from Johnson and Helferty, 1990]. The energy from the signal can either be reflected away or backscattered to the receiver.

Rough surfaces both scatter and reflect, while smooth surfaces mainly reflect specularly. Thus, except when the angle of incidence is 0, smooth surfaces will appear less reflective. SeaMARC II plots strong reflectors as dark, so rough surfaces, which tend to return more signal to the towfish, will appear dark on a SeaMARC sidescan image and be associated with higher intensity values. By the same token, smooth surfaces appear lighter on a SeaMARC sidescan image because less energy is returned to the towfish.

SeaMARC II bathymetric information is collected in the same manner as the sidescan image data, but is processed differently via a phase difference algorithm. The pairs of transducers on each side of the towfish operate in parallel on transmission. Upon reception, each row in the pair is sampled separately. Any signal with an incidence angle off normal to the transducer face will have a different phase lag at each row. The depression angle (θ) of the reflector (Figure 41) is calculated from this phase lag [Hussong and Blackinton, 1983]. The slant range (SR) (Figure 42) to the reflector is calculated using round trip travel time of the signal and an assumed sound speed of 1500 m/s. Conversion of SR and θ for each reflector into across-track distance and depth produces values which can be contoured, creating a bathymetric map.

Processing corrections applied to SeaMARC II image data are of two types - radiometric and geometric. Radiometric corrections refer to those that remove all contributions to

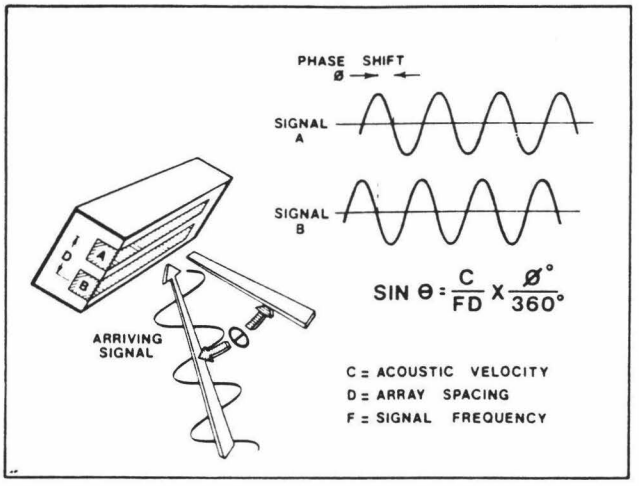

FIGURE 41. Schematic of SeaMARC II phase difference measurement technique for determining the acoustic angle to the target reflector. Using precise arrival times and this calculated angle Θ, range and depth pairs can be calculated across-track. [From Blackinton et al., 1983].

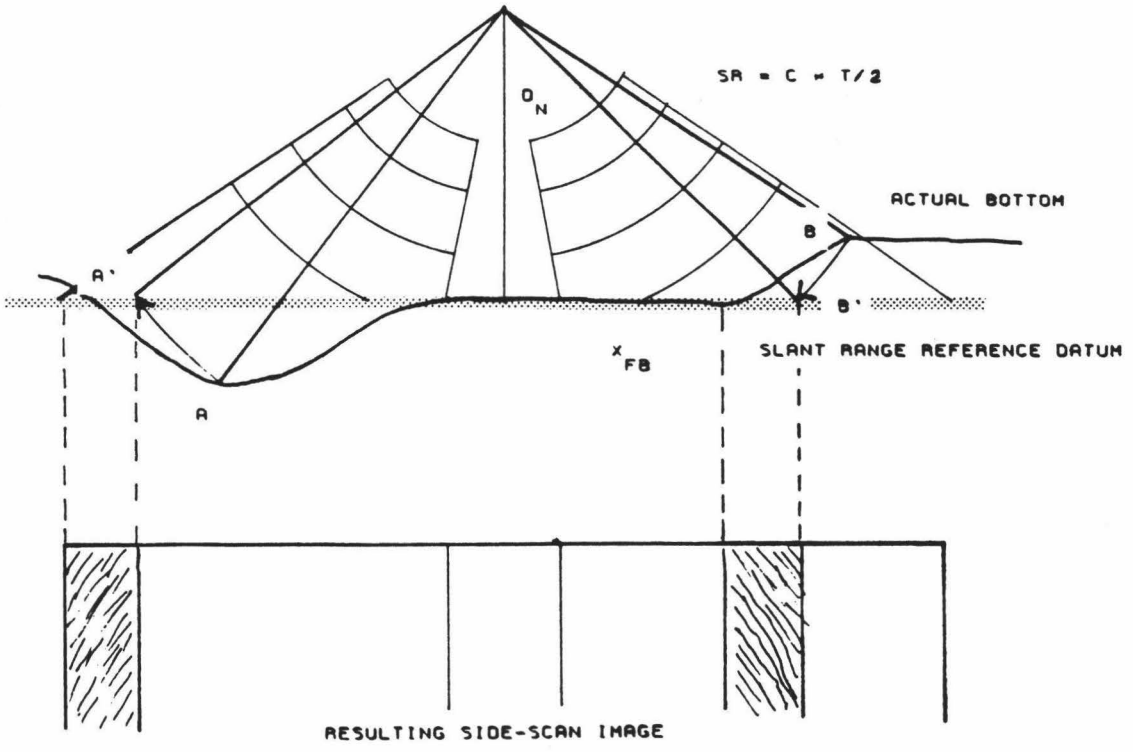

FIGURE 42. Diagram showing how regional slope can cause the target reflector to be displaced from its actual position, due to the flat bottom assumption. Looking upslope, the 2-way travel time tricks the system into "thinking" the target is closer to nadir than it really is. Conversely, a target downslope will be displaced farther from the ship track than in actuality. This is called the layover effect and can be corrected for in order to move the targets to their proper positions [from Reed and Hussong, 1989]. SR is slant range and C is speed of sound in water. See text for details.

the sidescan data which are not indicative of actual changes in the acoustic character of the seafloor [Reed and Hussong, 1989]. Geometric corrections position features as close as possible to their actual locations. Radiometric corrections I focus on are time varying gain, angle varying gain and amplitude gain; the geometric correction most important to this study is layover correction.

Two of the radiometric corrections are applied automatically to the SeaMARC II sidescan data during acquisition. One is time varying gain, used to correct for spreading and attenuation of the acoustic signal [Bergersen, 1991]. The other is angle varying gain which corrects for variations in the transmitted beam pattern and the change in backscattered signal intensity observed at different look angles [Reed and Hussong, 1989]. A third type of amplitude gain is a scaling factor applied by an operator in response to the image amplitude of the data being recorded. These preprocessing corrections attempt to minimize image distortion, but are often inaccurate for the seafloor being surveyed. Post-acquisition processing is needed to eliminate these system and operator induced signals. However, in order to avoid loss of any pertinent acoustic information due to further processing and filtering which would remove the aforementioned distortions, we used a minimally processed sidescan record (Figure 43) in this study for extracting texture information.

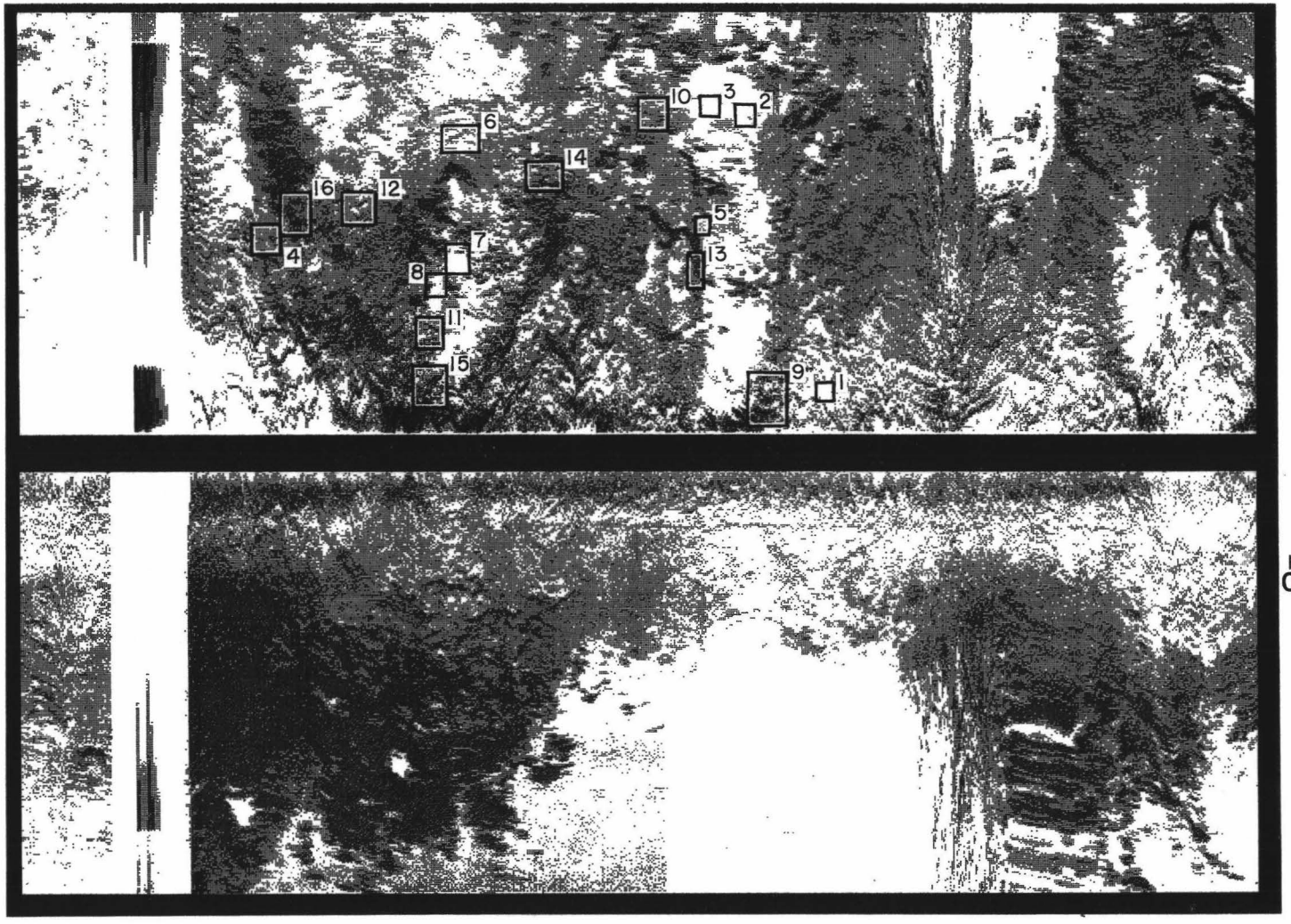

FIGURE 43. This raw SeaMARC II sidescan image shows sample locations from the preliminary study.

Before spatial analyses of sidescan sonar images can be attempted, the pixels must be correctly positioned, so a layover correction is applied. The layover correction is a post-acquisition processing technique which corrects the across-track distance at which pixels have been placed. During acquisition, most sonars assume the bottom is flat, at a mean depth given by the nadir signal return. If the depth across-track is different from the nadir depth, calculations of across-track distance will result in the pixels being misplaced. As seen in Figure 42, if the seafloor actually slopes, the calculated slant range (SR) using the time of travel to the target reflector (B in Figure 42) and back to the towfish results in displacement of the reflector downslope, and the pixels associated with the reflector are plotted too close in across-track distance. Conversely, a point targeted in the downhill direction (A in Figure 42) is plotted too far from nadir because of the flat bottom assumption. For the purposes of accurate sample locations for our study, layover correction was applied to the sidescan using a computer program which adjusted the across-track position of pixels composing the sidescan, to SeaMARC II bathymetry (Figure 44) which had been renavigated and coregistered to SeaBeam bathymetry (Figure 45). Using the SeaMARC II bathymetry as a "map", the program mosaics the sidescan image over the bathymetry so that topographic features are positioned close to their actual plan view locations (Figure 46).

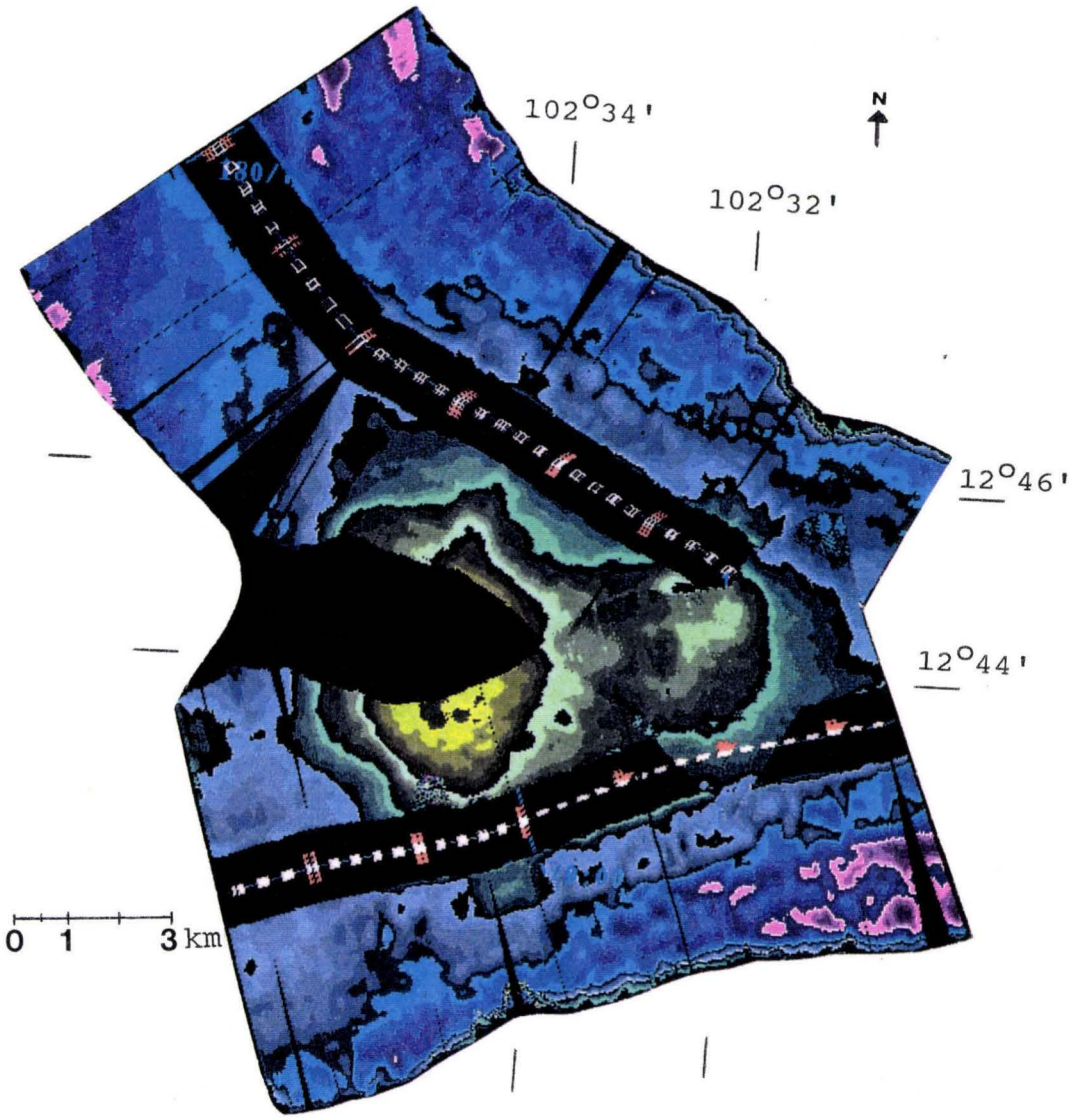

FIGURE 44. Fully corrected SeaMARC II bathymetry of Seamount 6. Contours are at 50 m intervals. Black signifies areas of no information.

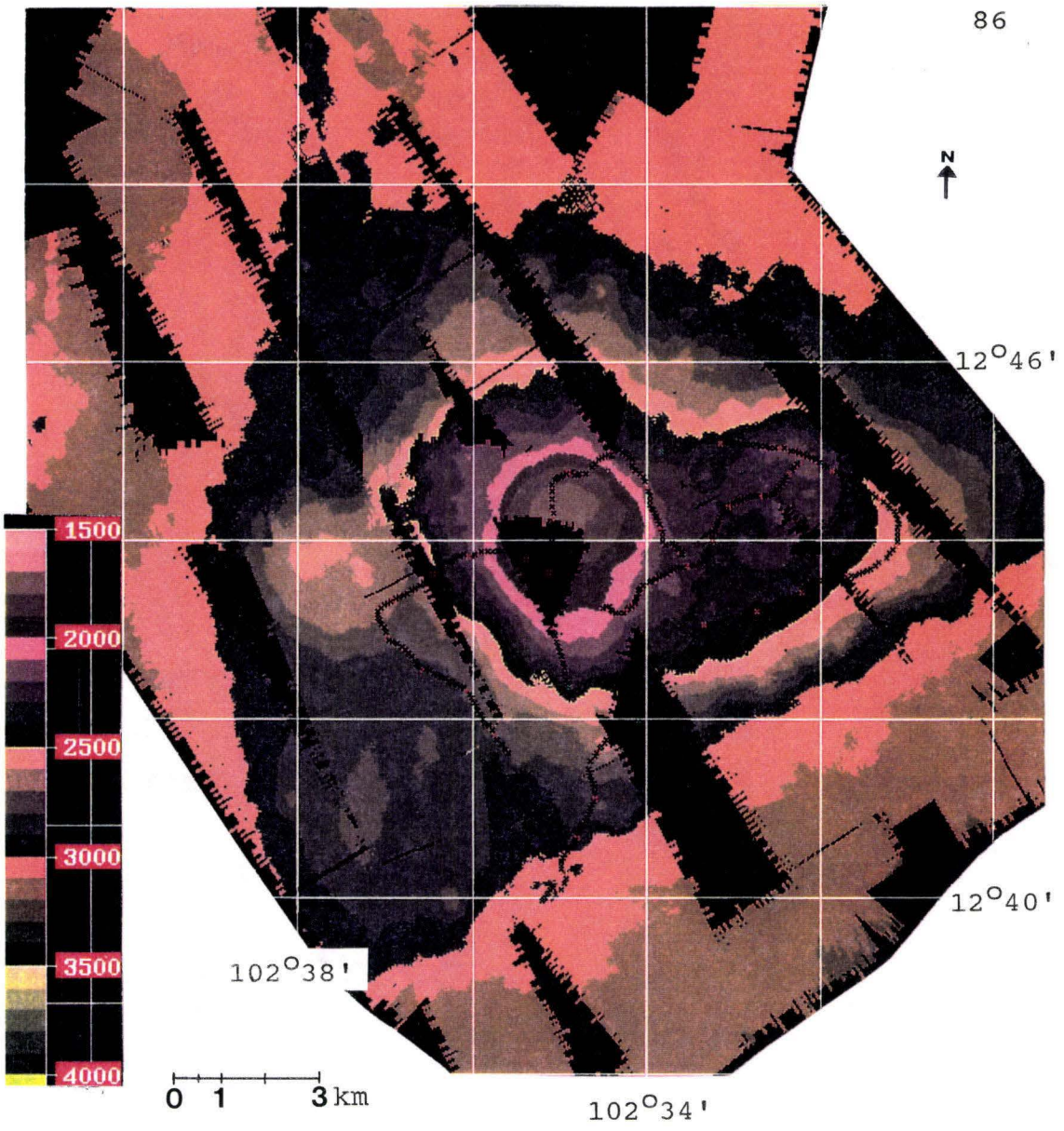

FIGURE 45. Fully corrected SeaBeam bathymetry of Seamount 6 showing plotted digitized ANGUS tracks. Contours are at 100 m intervals.

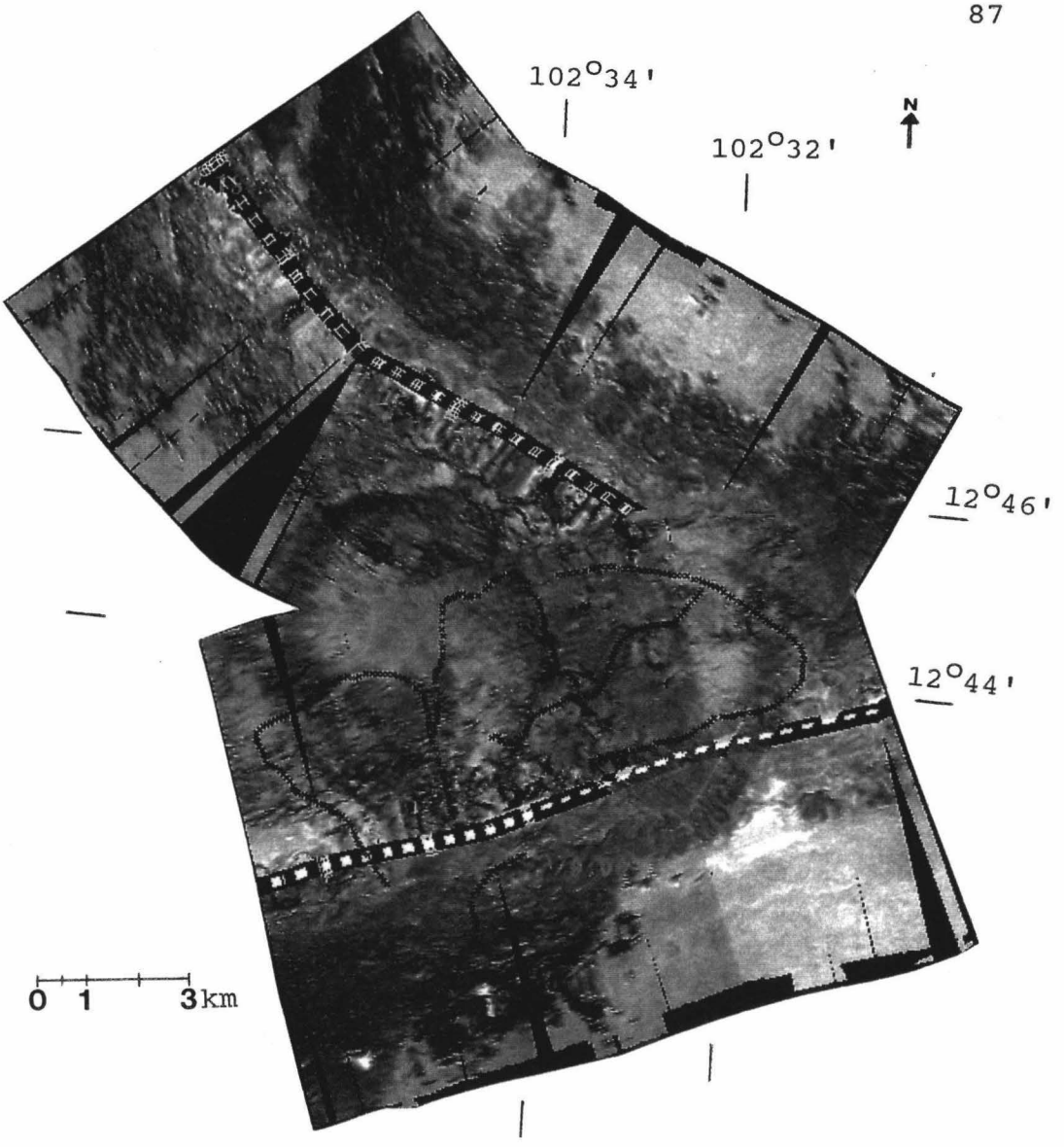

FIGURE 46a. Layover-corrected, renavigated SeaMARC II sidescan with digitized ANGUS tracks superimposed. Displays both the top and bottom coregistered sidescan swaths covering our survey area. ALVIN tracks were not digitized due to transponder problems.

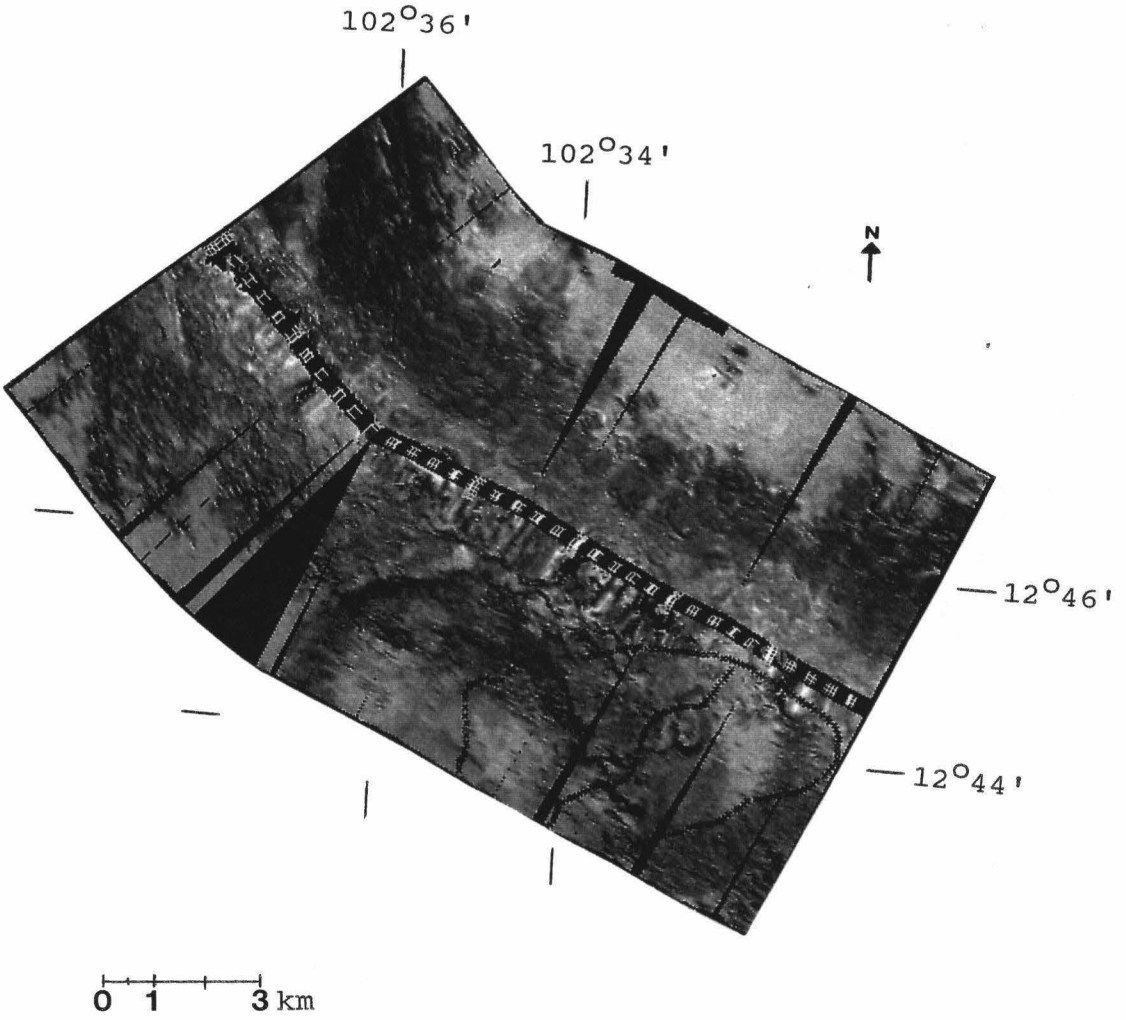

Figure 46b. Shows just the top swath of the survey (covered in 46a).

Data analysis can become more complicated than alluded to previously, i.e., rough surfaces appear as strong reflectors and smooth surfaces as weak reflectors. For instance, the generalization stated above is highly dependent upon regional slope; the inverse (rough surface = weak reflector and smooth surface, strong) is possible. Also, significant (up to several meters) acoustic penetration of sediments occurs at frequencies of 12 kHz or lower [Gardner et al., 1991]. The depth of this penetration depends on the frequency and angle of incidence of the signal and the physical properties of the sediment. Sonar images may, therefore, map lithologic variations obscured by a thin coating of sediment. Indeed, Mayer [1979] and Tyce et al. [1980] have demonstrated interference by shallow subbottom reflections. Another possible complication is volume reverberation. Once the sound penetrates below the water/sediment interface, it interacts with a volume of sediments and is reradiated in all directions, including back to the sidescan receivers [Stanton, 1984; Jackson et al., 1986]. The return signal would therefore be stronger than normally expected from sediment and the image would appear darker.

With this rudimentary knowledge of SeaMARC II data acquisition and analysis in hand, I now present a brief description of the area of seafloor that was surveyed for this study.

SETTING

Seamounts are ideal to the current study because they possess variable geology, variable slopes and cover only a small area. The type of geology present is highly correlated with regional slope and, therefore, with location on the seamount (i.e., base, flank, summit). Seamount 6 was selected due to an abundance of data from a variety of surveys: SeaMARC II, SeaBeam, ANGUS towed camera and ALVIN submersible. What follows is a short tour of Seamount 6, including a brief introduction, an overview of types of lithologies found at the base, flanks and summit regions of the edifice, as well as a summary of the volcanic history of the volcano. Detailed descriptions and analyses are found in Batiza et al. [1989] and Smith and Batiza [1989].

Seamount 6 is a small linear seamount group consisting of three coalesced edifices aligned parallel to the relative motion of the Cocos plate [Batiza and Vanko, 1983] (Figure 47). Located about 75 km south of the East O'Gorman Fracture Zone, it sits on crust of ~3.0 Ma (Figure 48). The middle edifice of this group (6C) is the largest (52 km^3, ~1300 m high), while the east and west volcanoes (6E and 6W) are 21 km^3, 750 m high and ~22 km^3, 420 m high, respectively [Batiza et al., 1989]. Volcano 6E has an arcuate summit bench and a summit crater (750 m wide) which

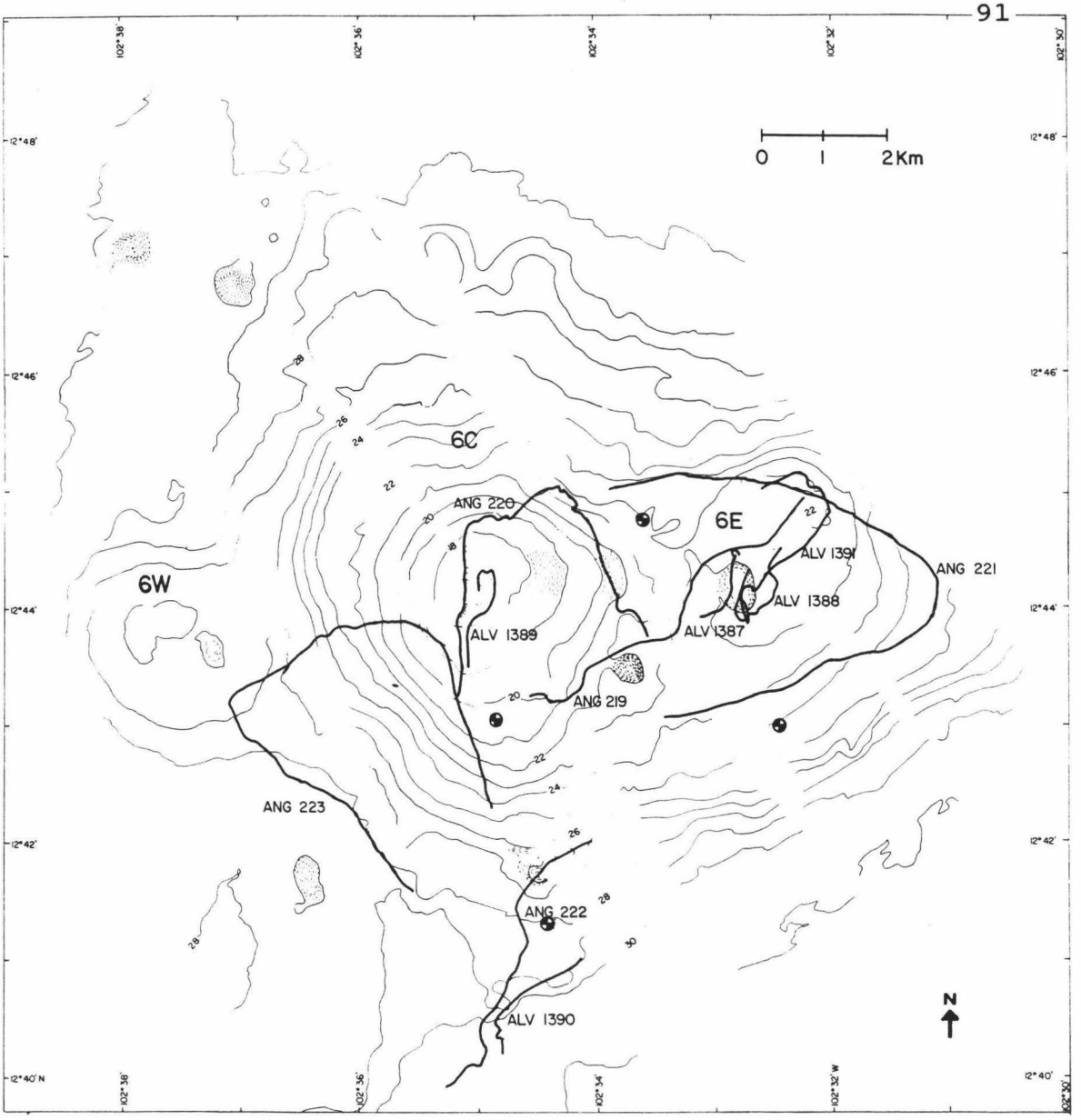

FIGURE 47. Bathymetric map of Seamount 6 showing the ALVIN and ANGUS tracks [Batiza et al., 1989]. Contours are in hundreds of meters.

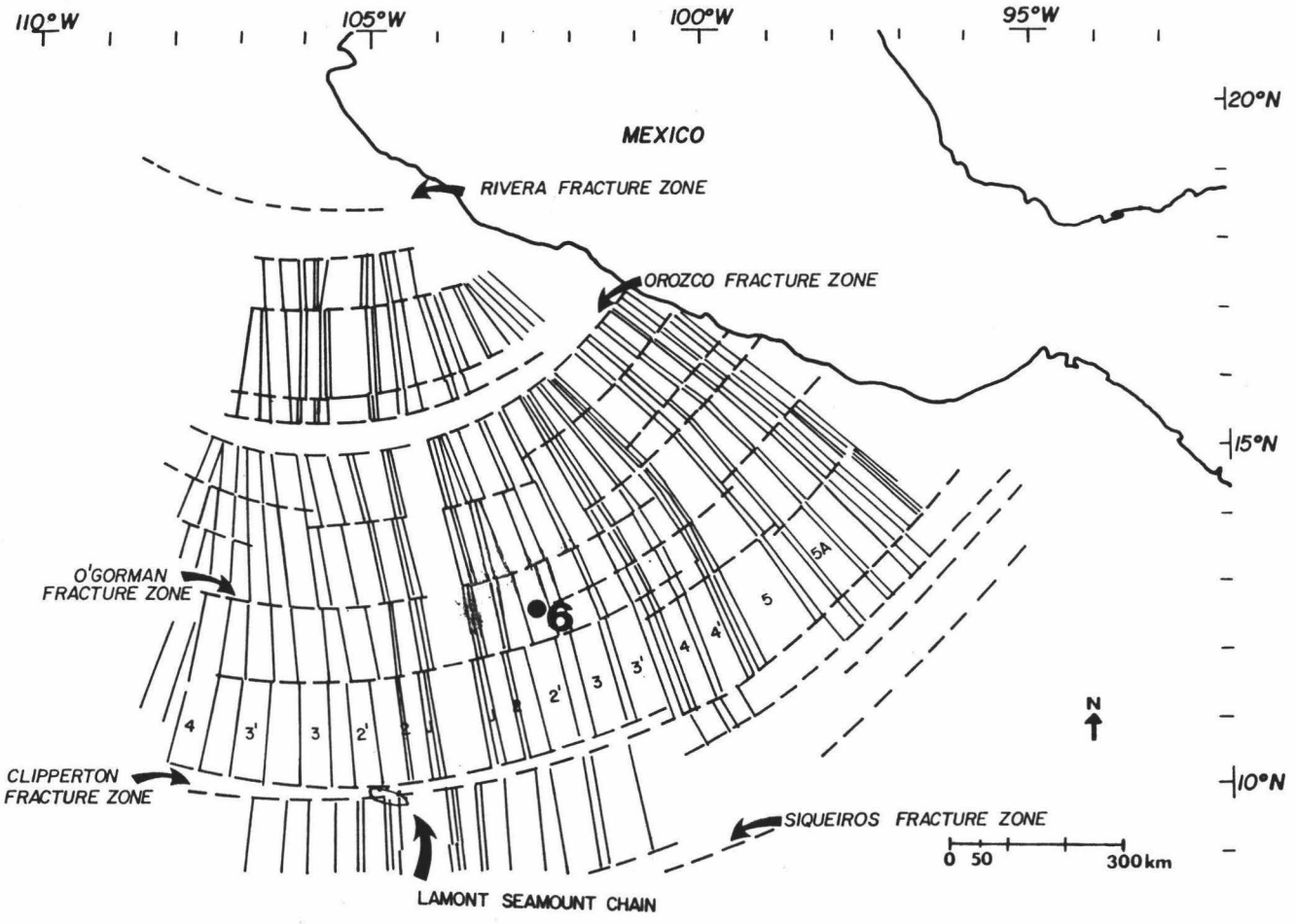

FIGURE 48. Location map of Seamount 6 [Batiza et al., 1989]. Magnetic lineations after Klitgord and Mammerickx [1982].

is open to the west. The summit of 6C is gently sloping and terraced. Batiza et al. [1989] interpret it as a filled caldera. A prominent flank rift zone on the north side of 6C trends at 340°, subparallel to the trend of the East Pacific Rise. The lower flanks of 6C are gentle and contain many small volcanic cones, up to 100 m high. Seamount 6 was surveyed by 5 ALVIN dives and 5 ANGUS camera runs (Figure 47). The geology determined from examination of bottom photographs acquired along these traverses are shown in Figures 49, 50 and 51.

The cone and lava field south of 6C, surveyed by ANGUS 222 and ALVIN 1390 (Figure 51), is composed mainly of pillow lava which forms haystacks and outcrops of bulbous and tubular pillows [Batiza et al., 1989]. Most of these outcrops, even on steep slopes, are evenly covered with dark fine-grained sediment. The individual rocks have coatings of manganese up to 2 cm thick and are weathered. Very steep slopes, which are probably fault-controlled, have in situ tubular pillows and may, in addition, possess aprons of pillow talus. Similar deposits characterize the deeper (below 2500 m) flanks elsewhere on 6C and 6E, but are almost completely covered with sediment and have greater amounts of talus [Batiza et al., 1989]. The steeper outer flanks of 6C and 6E (2500 m to 2300 m) consist of pillow tubes elongated downslope and, for the most part, are free of sediment (Figure 52). On gentler slopes, there are scattered outcrops of bulbous pillows and

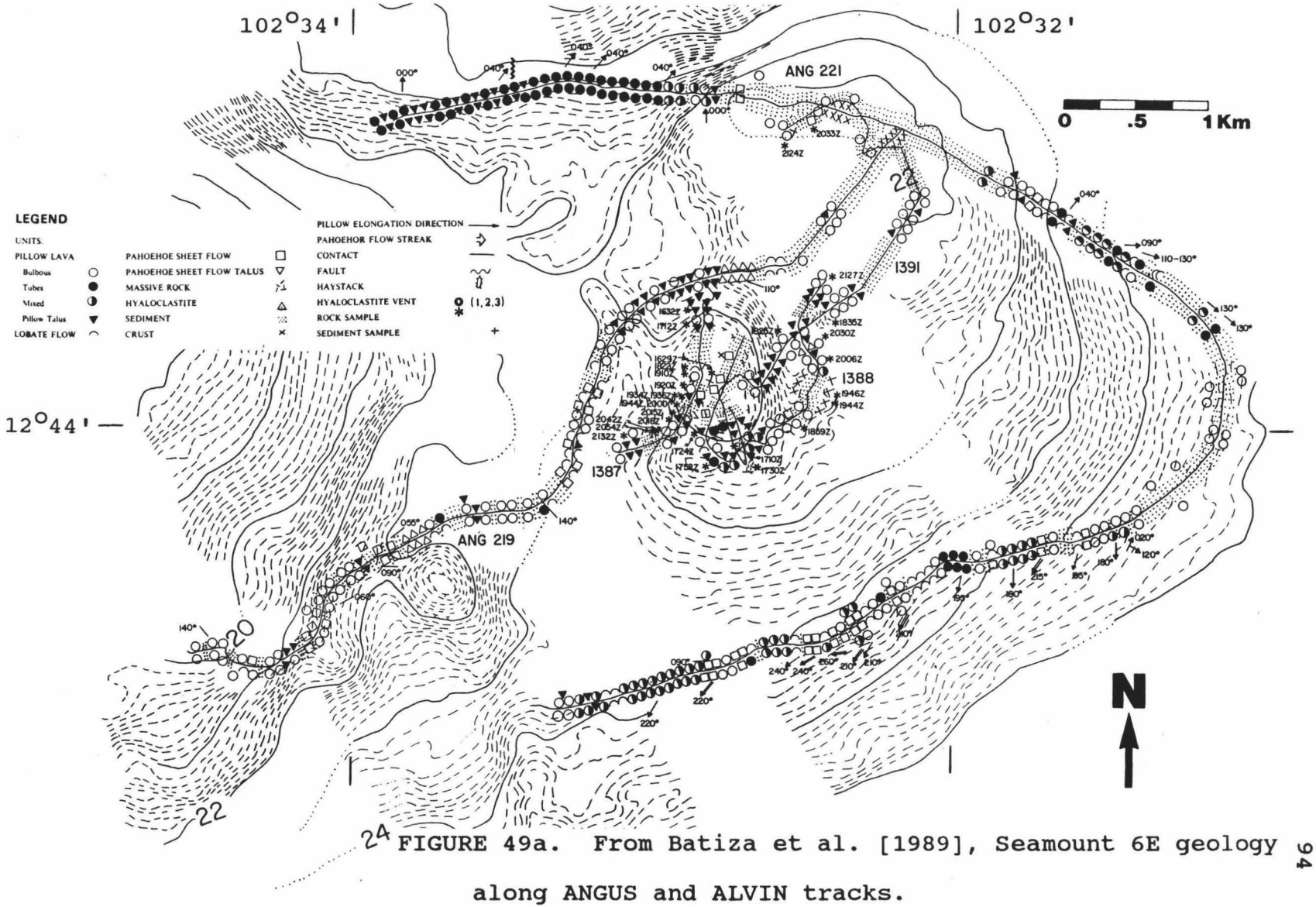

FIGURE 49a. From Batiza et al. [1989], Seamount 6E geology along ANGUS and ALVIN tracks.

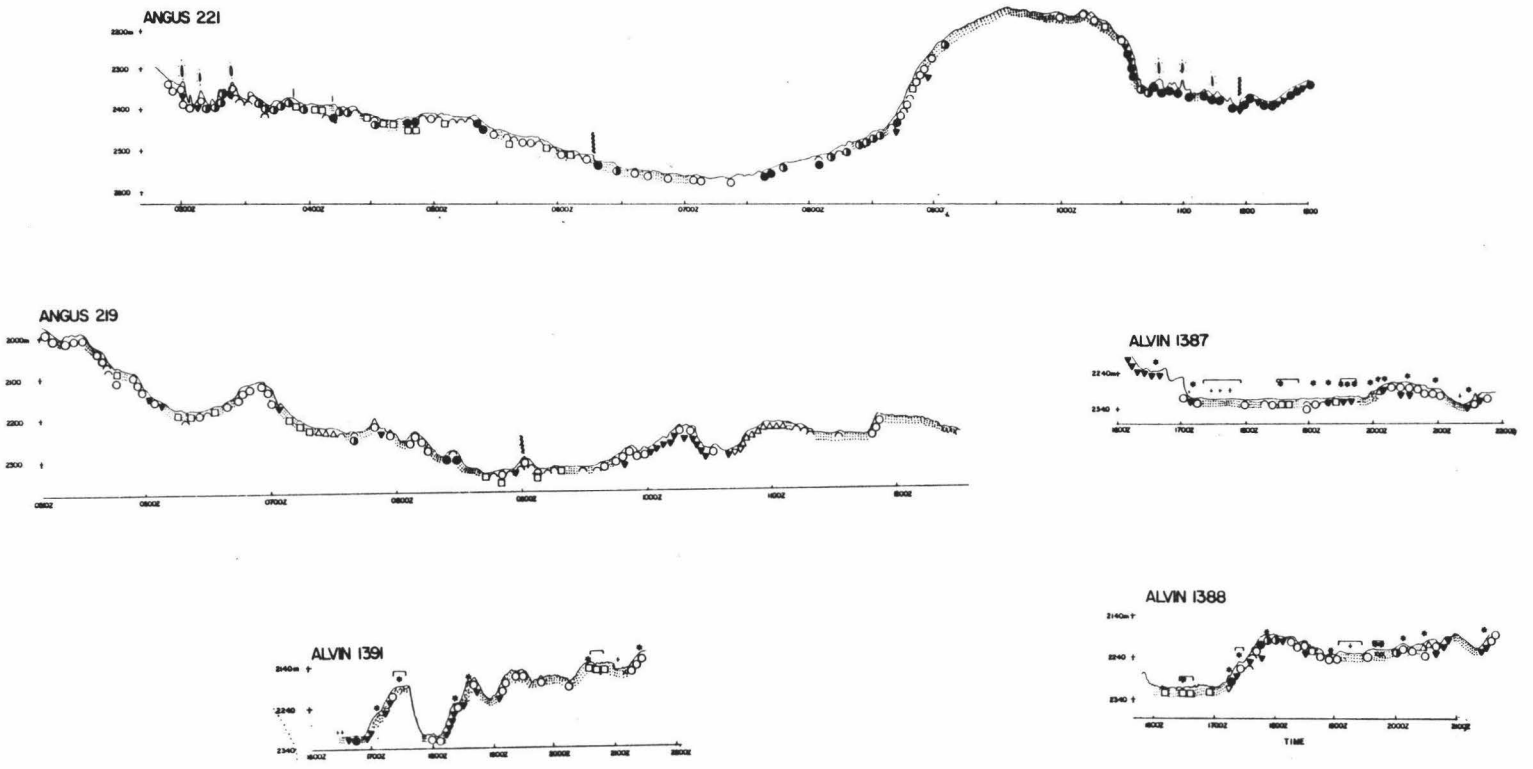

FIGURE 49b. From Batiza et al. [1989], profiles of the dive tracks from Figure 49a showing geology (V.E. 4X).

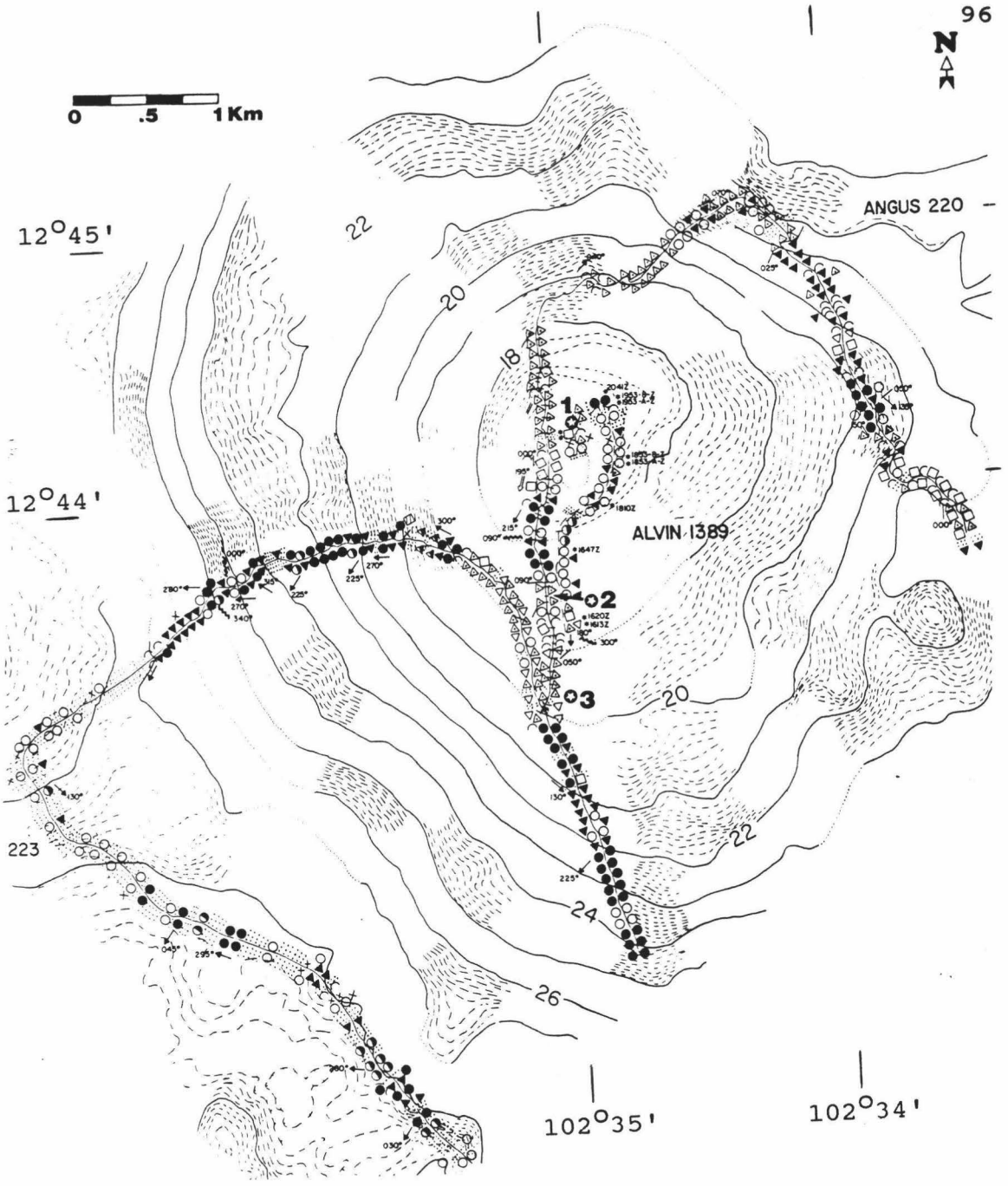

FIGURE 50a. Geology of Seamount 6C along ANGUS and ALVIN tracks [Batiza et al., 1989]. Symbols are the same as those of Figure 49.

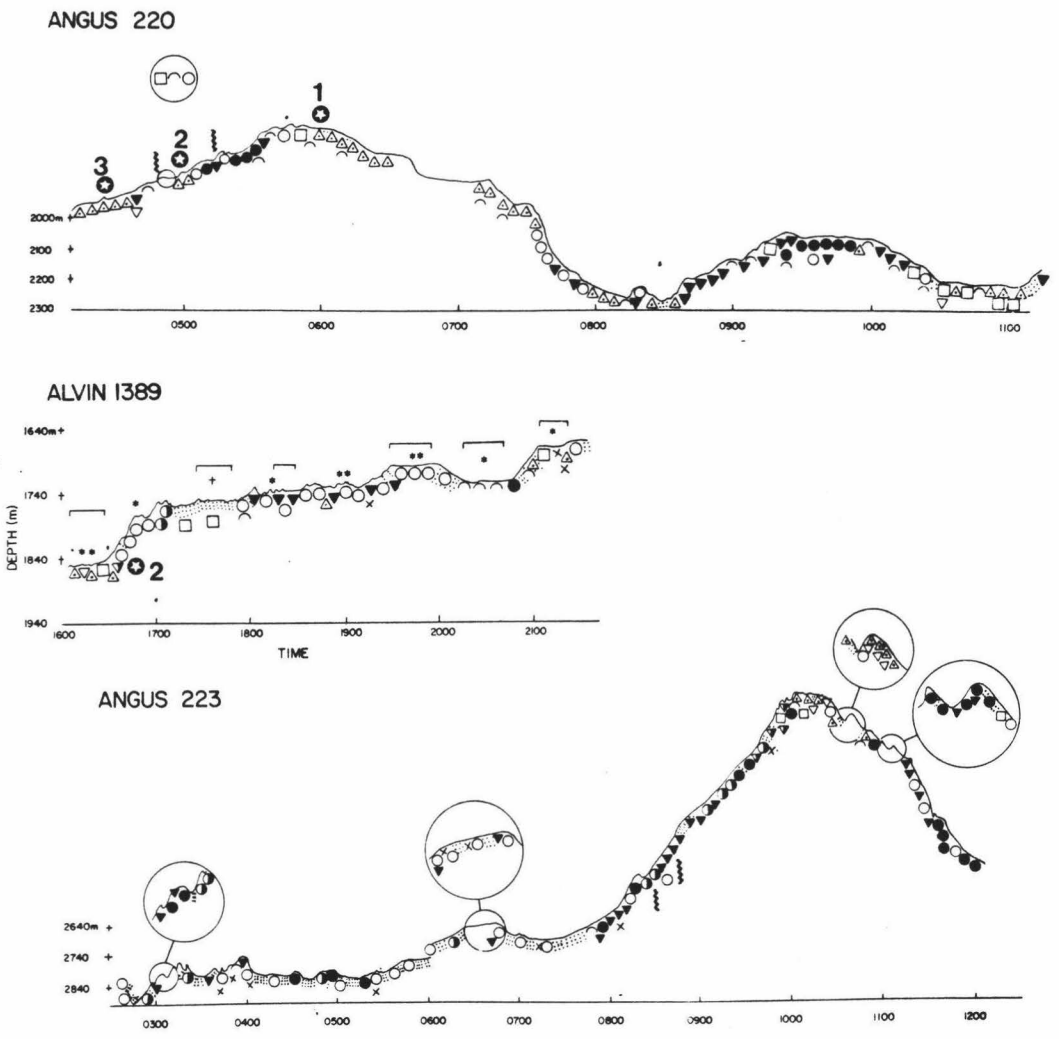

FIGURE 50b. Profiles (V.E. 4X) along the dive tracks from Figure 50a [Batiza et al., 1989]. Symbols are the same.

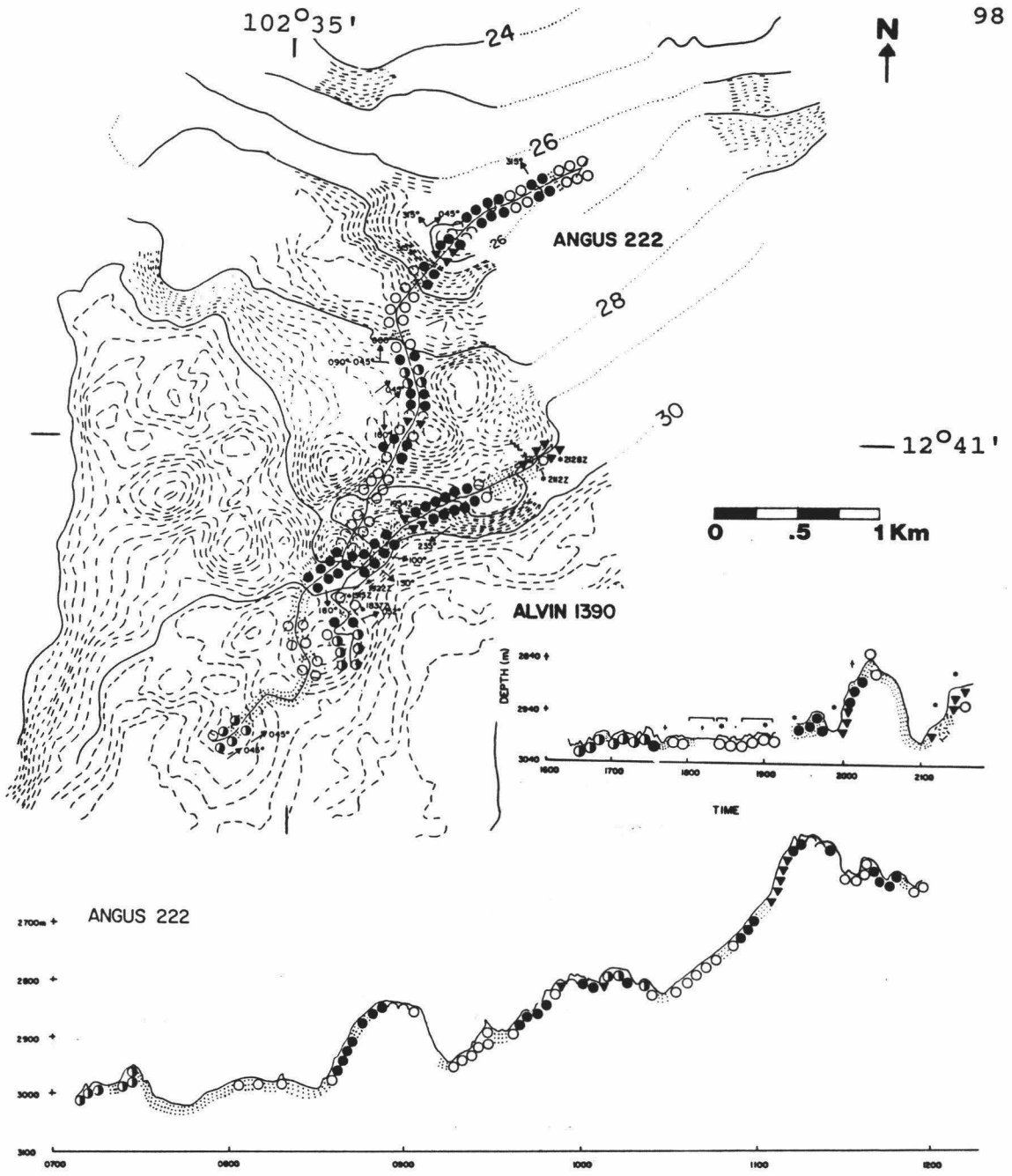

FIGURE 51. Geology of the cone/lava field on the flanks of Seamount 6 along the ALVIN and ANGUS tracks, with profiles (V.E. 4X) [Batiza et al., 1989]. Same symbols as Figure 49.

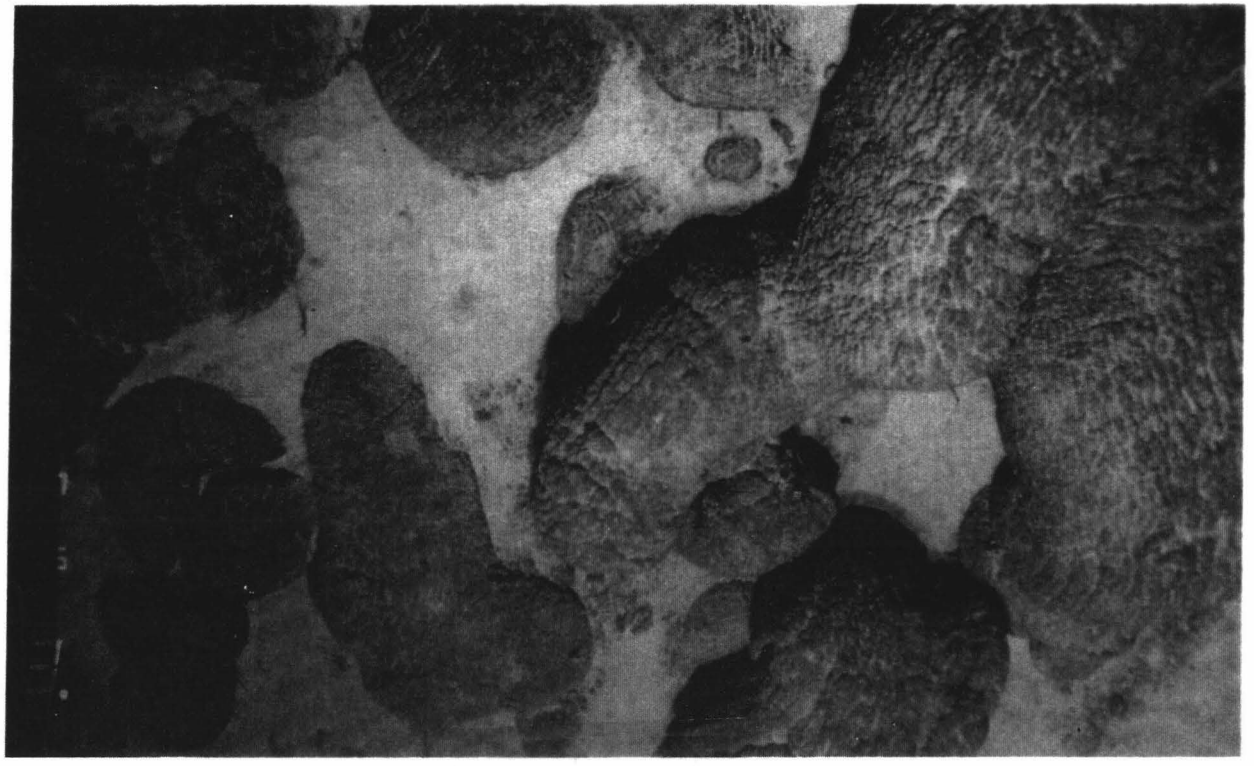

FIGURE 52. Photo showing elongate and bulbous pillows on the south flank of Seamount 6C. ANGUS 223, 0918Z [from Batiza et al., 1989].

minor talus deposits. Between 6C and 6E, lies a saddle which is sedimented and has about 50% or less rock outcrop. Lava haystacks and small pillow ridges characterize the slopes of 6C near the saddle. The slopes of 6E in this vicinity consist mainly of pahoehoe (Figure 53) and large lobate pillows with scattered talus outcrops [Batiza et al., 1989].

Shallower than 2200 m, the summit of 6C consists mostly of hyaloclastite (Figure 54), sheet flows, submarine pahoehoe and lobate pillows. Hyaloclastite is a name used to describe many different rocks consisting mostly of basalt glass fragments. Deposits vary in shape and size and the rocks themselves often have different textures and types of glass shards, presumably depending upon magma type and mode of formation [Smith and Batiza, 1989]. On Seamount 6, most of the hyaloclastites are of hydrovolcanic origin, but some show evidence of being sedimentary in origin. The deposits are sheet-like with variable surface textures. The sheets thin at the distal ends and are often broken up into slabby fragments. Hyaloclastites may be rubbly nearer inferred vents and overlie sheeted deposits [Smith and Batiza, 1989]. Above 2000 m, the summit deposits of hyaloclastite, sheet flow, submarine pahoehoe and lobate pillow appear very young and have only 2-3 mm of manganese coating [Batiza et al., 1989]. More than ~50% outcrop is present in the summit area. These outcrops are separated by sediment ponds which become rippled at depths

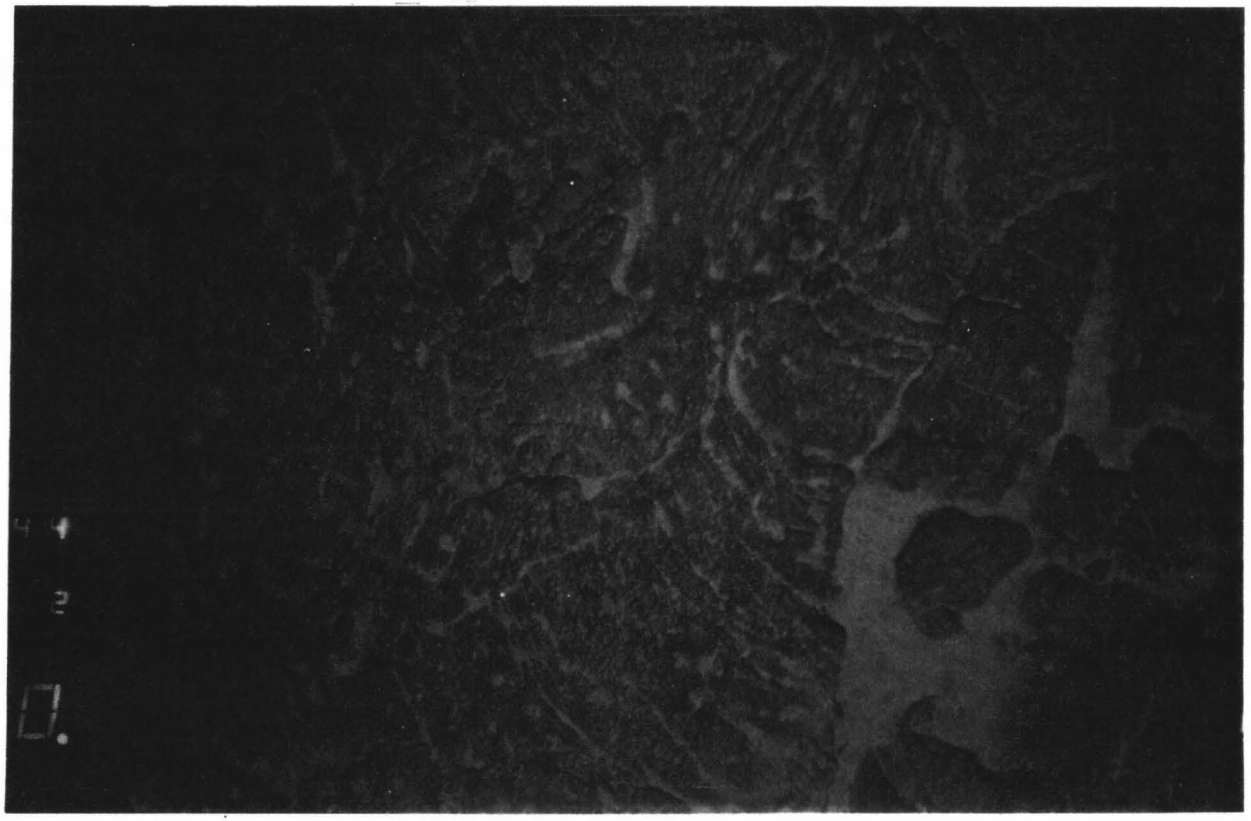

FIGURE 53. Photo showing ropey pahoehoe on the gentle slopes of Seamount 6C near the saddle with 6E. ANGUS 220, 1044Z [from Batiza et al., 1989].

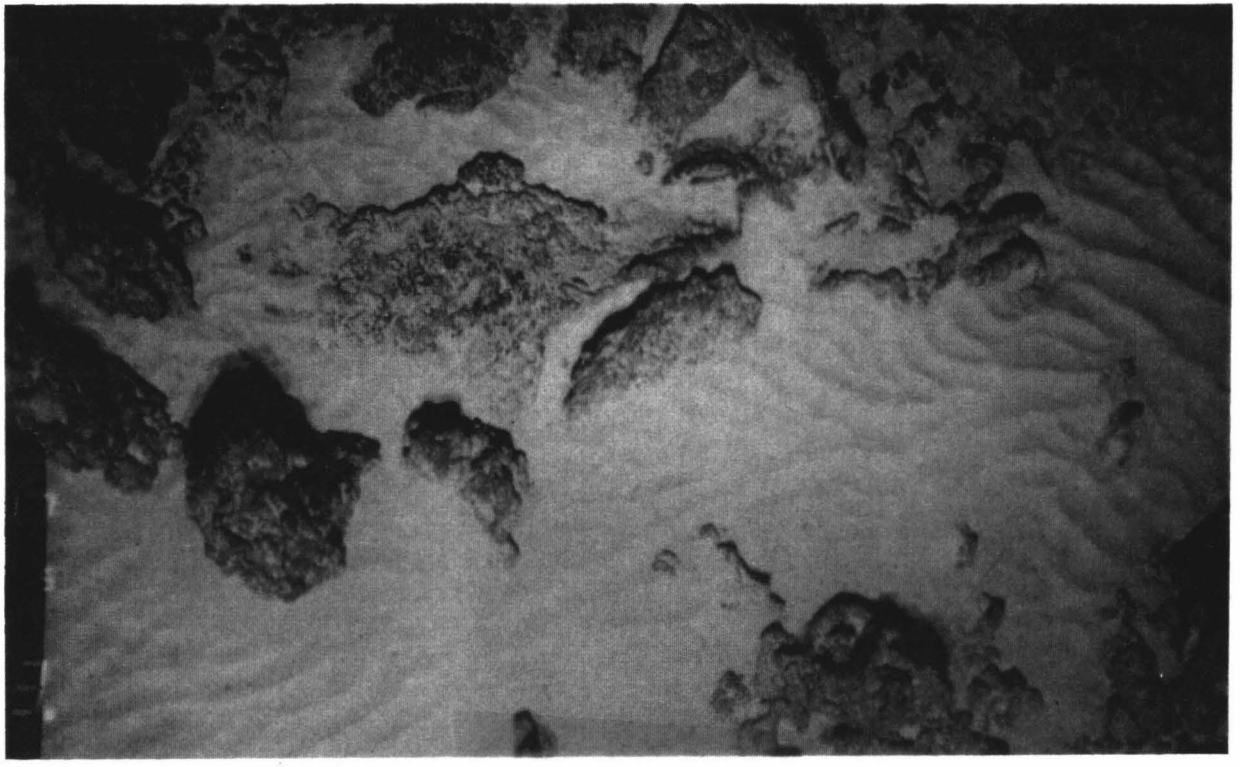

FIGURE 54. Photo showing tabular hyaloclastite and rubbly lava with rippled sediment on the summit terrace of Seamount 6C. ANGUS 223, 1017Z [from Batiza et al., 1989].

< ~2000 m. The summit area of 6E consists mostly of pillow flows with only rare pahoehoe and lobate pillows. A thick covering of rippled sediment blankets the summit of 6E. On both 6C and 6E, the general direction of sediment transport is to the east [Batiza et al., 1989], as shown by directional indicators such as ripples and scour marks. On 6C and 6E, sediment transport is usually downslope; however, there are some locations on 6E where sediment ripples indicate transport up gentle slopes.

The caldera walls of 6E are mostly covered with pillow talus. The wall is vertical in places, but elsewhere on gentler slopes, there are scattered outcrops of bulbous pillows which appear in situ [Batiza et al., 1989]. Talus, covered and mixed with sediment, is present at the base of the caldera wall. Sediment almost entirely covers the floor of the caldera. Pahoehoe, lobate pillows and deposits of honeycomb-textured lava that resembles spatter compose the rare outcrops [Batiza et al., 1989]. The rocks on the summit of 6E appear older than those on the summit of 6C. On 6E, rocks generally have thick (mostly 2-3 cm, up to 7 cm) coats of manganese and are weathered. Based on outcrop appearance, thickness of manganese coats and sediment thickness, Batiza et al. [1989], proposed that 6W, 6E and 6C formed about the same time. Pahoehoe preceded caldera collapse on 6E, followed by pillow eruptions at the summit bench and elsewhere. At the time of formation of the 6E caldera, 6C may also have had a caldera. The

filling of the 6C caldera may have occurred at the same time as post caldera eruptions on 6E. However, summit eruptions on 6C apparently continued for some time after volcanic activity ceased on 6E.

TEXTURE FEATURES

In order to describe the sidescan data used in this study, some knowledge of how images are interpreted is necessary. Humans use three features to interpret pictorial information [Haralick et al., 1973], including spectral, textural and contextual. While spectral features describe the average tonal variations in different bands of the visible and infrared portions of the electromagnetic spectrum, textural features contain information about the spatial distribution of tonal variations within a band. Contextual features provide information derived from the surroundings of the area being analyzed. Context, texture and tone are always present in an image, but there are times when one property may dominate. Texture and tone are most important in single-spectral band image areas such as sidescan images. Tone describes the varying shades of grey of pixels in an image. Texture pertains to the spatial distribution of the grey tones composing an image. Texture is an intrinsic property of all surfaces, containing important information about the structural arrangement of surfaces. It is a strongly stationary property independent

of illumination and carries useful information for discrimination purposes. Provided below is a discussion of the relative effectiveness of second-order textural statistics versus first-order statistics, as well as an introduction to the grey level co-occurrence matrix method of texture characterization by which the second-order statistics used in this study were estimated.

Multispectral remote sensing images such as Landsat consist of a scene imaged simultaneously in several bands of the electromagnetic spectrum [Schowengerdt, 1983]. For single-spectral images such as those produced by single-frequency side-looking sonars and radars, first-order statistics like mean intensity are not effective in classifying imagery. Different intensity values from a uniform reflector can be caused by several factors, including random noise, system changes and imaging geometry. Image speckle or random image noise can be caused by ambient noise, electronic noise and water column transmission anomalies [Reed, 1987]. It takes the form of isolated pixels with intensities uncorrelated to their neighbors. Gain changes applied during acquisition of data, required by variations in signal strength due to changes in water depth or reflectivity of a lithologically uniform surface, destroy any 1:1 relationship there might have been between intensity and target strength [Reed, 1987]. And finally, variations in backscatter strength occur along with changes in angle of incidence of the

outgoing acoustic signal, which are not completely rectified by angle varying gain corrections. Therefore, looking at texture, an abstract second-order statistic feature which relies on the spatial relationships between tonal variations and is independent of image intensity (though it is inter-related), is more useful in classifying single spectral imagery such as sidescan data.

Subjectively, texture recognition is easy for the human observer, but difficult to quantify in the objective sense. Of the many proposed methods for extracting statistical texture signatures for image analysis [Pratt, 1978; Laws, 1980; Haralick et al., 1973], we use the grey level difference matrix method which is closely related to the grey level co-occurrence matrix method of Haralick et al. [1973]. The use of this type of texture characterization is justified by results of experiments in human texture perception which indicate that second-order probabilities of the form measured by co-occurrence matrices are important in texture discrimination [Julesz, 1962; Julesz et al., 1973; Gagalowicz, 1980]. What follows is a description of the grey level co-occurrence matrix method of Haralick et al. [1973].

The grey level co-occurrence matrix method works under the assumption that texture information in an image is contained in the overall or average spatial relationship which the grey tones in the image have to one another [Haralick et al., 1973]. A set of grey-tone spatial-

dependence probability-distribution matrices are created for a given image block. These matrices express the relative frequencies P_{ij} with which two adjacent pixels, separated by distance d, occur on the image, one having grey tone i, the other j [Haralick et al., 1973]. Moments evaluated from these joint probability matrices provide quantitative estimates of image texture.

Digital images are stored in the computer as a 2 dimensional array of resolution cells, or pixels. Each pixel is assigned some grey tone value N_g, N being the number of grey levels possible. Each grey level co-occurrence matrix is a square matrix with dimension N. The entries in this matrix, S(i,j;θ,d), are the number of times a pixel of intensity i has a neighboring pixel of intensity j in the direction θ, at a distance of d. As an example, say the image is represented by

1	1	2	3	3
1	2	2	3	4
2	3	3	4	4
1	2	4	4	4
1	1	3	3	3

In the horizontal direction ($\theta = 0^{o}$), at a lag or distance of 1, the grey level co-occurrence matrix is

	1	2	3	4
1:	4	3	1	0
2:	3	2	3	1
3:	1	3	8	2
4:	0	1	2	6

[Reed, 1987]. In the case of our grey level difference matrices, the entries in the matrices express the

probability that two pixels separated by distance d, in the direction θ, will differ in intensity by X amount. The elements of the matrix are normalized by dividing each entry by the total number of possible entries for that direction θ and distance d. The matrices are evaluated at $\theta=0^{o}$, 45^{o}, 90^{o} and 135^{o} (Figure 55). To avoid any angular dependence upon the texture signature, Haralick et al. [1973] suggested taking the average and the range of the statistics which are extracted at each angle θ.

Haralick et al. [1973] discussed 14 texture feature vectors which can be extracted from the grey level co-occurrence matrices. As many of these features are strongly correlated to each other, we use only 6 plus isotropy, devised by Reed and Hussong [1989]. The texture features we examine include: contrast, measuring image contrast; inverse difference moment, measuring local homogeneity of the image; entropy, a measure of image complexity or how structured the image is; energy, measuring image busyness or coarseness; mean; correlation, a measure of linearity of the image; and isotropy, measuring the rotational invariance of the image. Appendix A contains formulas and explanations for each of the texture features mentioned.

A texture feature vector, composed of the seven second-order statistics listed above (contrast, entropy, etc.) is used to define each sample (i.e., numbered boxes in Figure 43). A sample is a group of pixels from a SeaMARC II

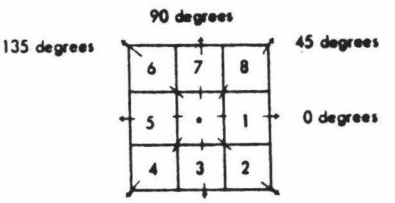

FIGURE 55. Diagram showing the angles of θ at which the grey level co-occurrence matrices are evaluated [from Haralick et al., 1973]. Pixels 1 and 5 are the nearest neighbors of the * pixel at 0^{o} (horizontal). Pixels 4 and 8 are nearest neighbors at 45^{o}. 3 and 7 are nearest neighbors at 90^{o}, and 2 and 6 at 135^{o}. This information is purely spatial and has nothing to do with grey levels.

sidescan image chosen as a representative area of a specific lithology. The following section describes how the feature vectors are used to classify samples into distinct groups.

CLASSIFICATION

The goal of classification is to attempt to assign the samples, each defined by a texture feature vector (composed of the seven second-order statistics), into distinct classes. This can be achieved through unsupervised or supervised classification schemes. An unsupervised classification is done by clustering. The feature vectors from each sample are given to a clustering routine which determines natural groupings of the data. In a supervised classification, samples are assigned to classes according to supplementary knowledge, such as that obtained of lithology from the examination of bottom photographs. In this way, classes are defined by representative, homogeneous samples for each class (in this study: pillow, sediment, hyaloclastite, sheet flow and talus).

The clustering algorithm used in this study for an unsupervised classification is Hartigan's [1975] K-means algorithm. The algorithm is initialized by assuming there are 1, 2,...K classes, K specified by the operator. K number of initial mean vectors are chosen either randomly,

assigned by the operator or defined by the data. This study allows the data to define the initial mean vectors. This is achieved by initially assigning each sample area to a class (1, 2,...K), done one of two ways, either cyclically or by weighted means. This is specified in a parameter file which is read by the clustering routine. The cyclic method will assign the first K samples to classes 1 through K, then the next K samples to classes 1 through K, and so on. The method of weighted means sums all the components of the feature vector for each sample, sorts them from highest to lowest and assigns the first X (total sample number/K) samples to class 1, the next X samples to class 2, and so on to class K. The clustering routine then calculates the means of the feature vectors for each of the assigned K classes. This mean vector for each K defines the centroid of that K class. The routine assigns each sample to that cluster from whose centroid its feature vector is least distant. Once all the samples are assigned to a cluster, the cluster means are recomputed, and the samples reassigned on a minimum distance basis. The process continues until there is no significant change in cluster assignment from one iteration to the next. In this way, each sample is classified, according to its second-order statistics, to the group to whose members it is most similar.

A supervised classification can be done using groundtruth information (bottom photographs) which we have

from ANGUS towed camera and ALVIN submersible dives. I assigned each sample area to a specific lithologic class (pillow, talus, hyaloclastite, sediment or sheet flow) based on my observations of the bottom photographs. The average feature vector and standard deviation for each class can then be calculated from the representative samples.

METHODS

Now that we have the necessary background information in hand, I discuss in this section the methods applied in this study. Specifically, I describe the preparation of SeaBeam and SeaMARC II data sets for analysis, the process involved in the selection of sample areas and how sample boxes were "picked" via a computer program designed to calculate texture statistics. I also include a brief review of preliminary results from the application of our technique which leads into a discussion of our final results.

Accurate location of sample areas for analysis required the coregistration of SeaBeam and SeaMARC II data. The logged SeaBeam data from Scripps contained shipboard navigation, which upon plotting showed significant offsets. To correct this, software was developed to play back the SeaBeam mosaic which was adjusted, by hand, to fit the bathymetric map from Batiza et al. [1989] (Figure 47),

assumed to be correctly navigated and adjusted. SeaMARC II navigation was readjusted by optimizing the fit, by hand, of SeaMARC II bathymetry (Figure 44) with the readjusted SeaBeam mosaic in Figure 45. SeaMARC II navigation was then replotted and merged with SeaBeam navigation (Figure 56).

The ANGUS camera tracks and ALVIN dive tracks had to be adjusted to the new coregistered data. These transponder-navigated tracks were previously plotted on SeaBeam bathymetry (Figure 47). In order to adjust the tracks, time ticks were added at 5 minute intervals and then digitized. There had been transponder problems on the ALVIN dives, so only the ANGUS tracks were digitized and plotted on the re-navigated, layover-corrected SeaMARC II sidescan (Figure 46). Figure 45 shows the dive tracks plotted on the mosaicked SeaBeam bathymetry. This allows for more accurate placement of sample boxes.

Despite all our careful efforts in coregistering and renavigating SeaBeam and SeaMARC II data, navigational uncertainties may still exist. These uncertainties may be of key importance and, at least, should be kept in mind. It is possible that due to navigational uncertainty, a patch of seafloor we see in the bottom photographs, does not correspond precisely with a patch of seafloor chosen to sample on the SeaMARC II sidescan image. Misplacement of sample boxes may also arise in the translation of the sample box locations from the layover-corrected sidescan

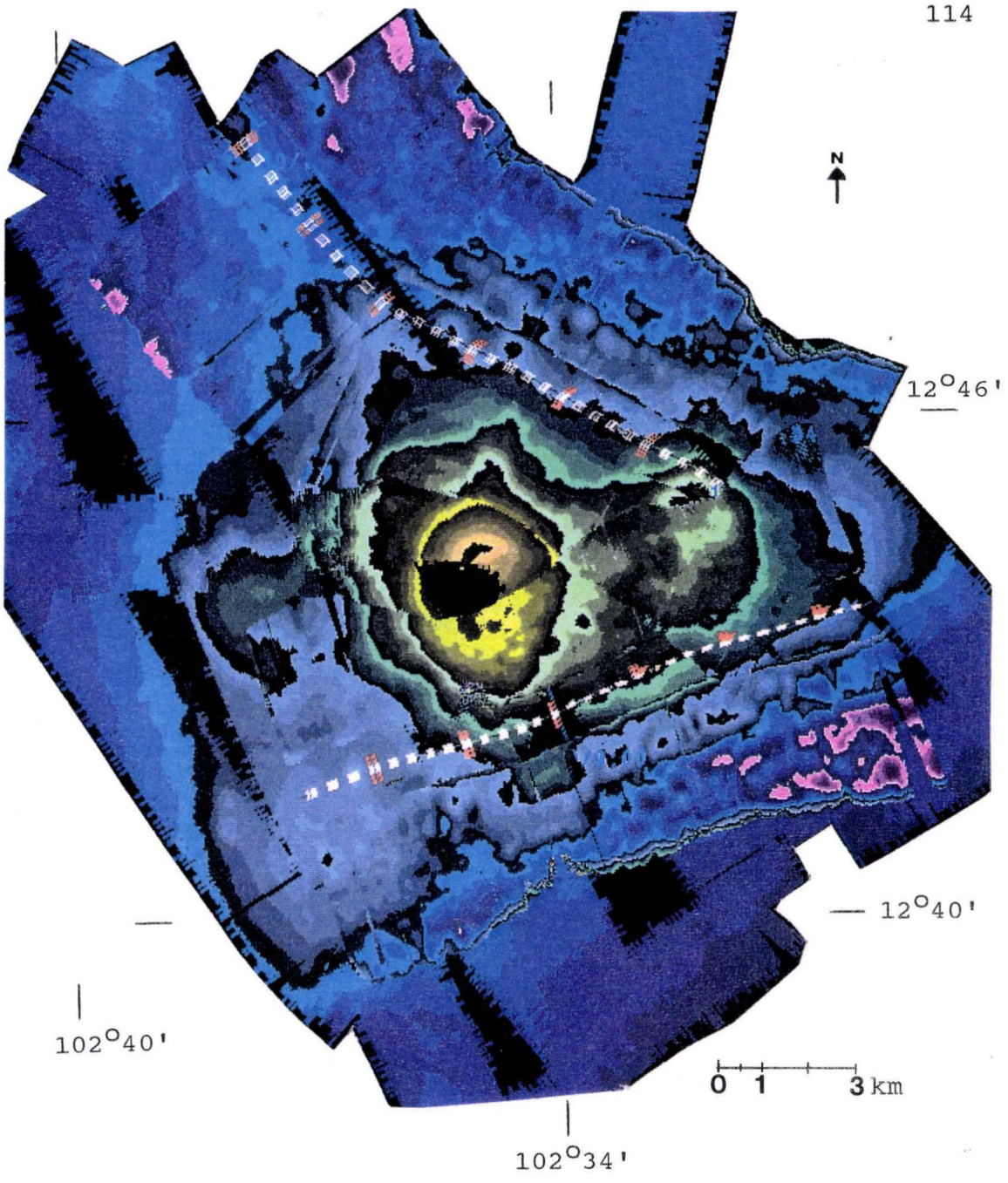

FIGURE 56. Renavigated, coregistered SeaMARC II and SeaBeam bathymetry at 50 m contour intervals. Black signifies areas of no information.

(Figure 46) to the less processed sidescan record actually used for the textural analysis (Figure 57).

With the SeaMARC II sidescan data prepared, a short feasibility study on the ability of SeaMARC II to distinguish among various lithologies was begun. In order to proceed, an assessment of groundtruth data (bottom photographs) was necessary in choosing viable sample locations. I meticulously examined the films and photographs from 5 ANGUS camera tows and 5 ALVIN dives and evaluated them for possible sample area locations. Geologic maps (derived from observations of these same films by Batiza et al. [1989]) along each track (Figures 49, 50, 51) provided a useful guide to pinpointing specific areas for examination. Sixteen sample locations were initially chosen (Figure 43), four of each in the following lithologies: sediment, pillow basalt, hyaloclastite and talus. Criteria for choosing these areas were: homogeneity of lithology, suitably extensive regions, similar bottom slope gradients for each lithologic group and similar look direction, or azimuth at which the area is viewed. "Suitably extensive regions" were determined by assuming a sample box size of approximately 200 pixels (in SeaMARC data), a size sufficiently large to generate useful statistics yet small enough to prevent blurring of any possible texture signature. This size box corresponds to about a 200 m^2 area. Locations along the dive tracks with lithologies extending this distance were chosen. Slope

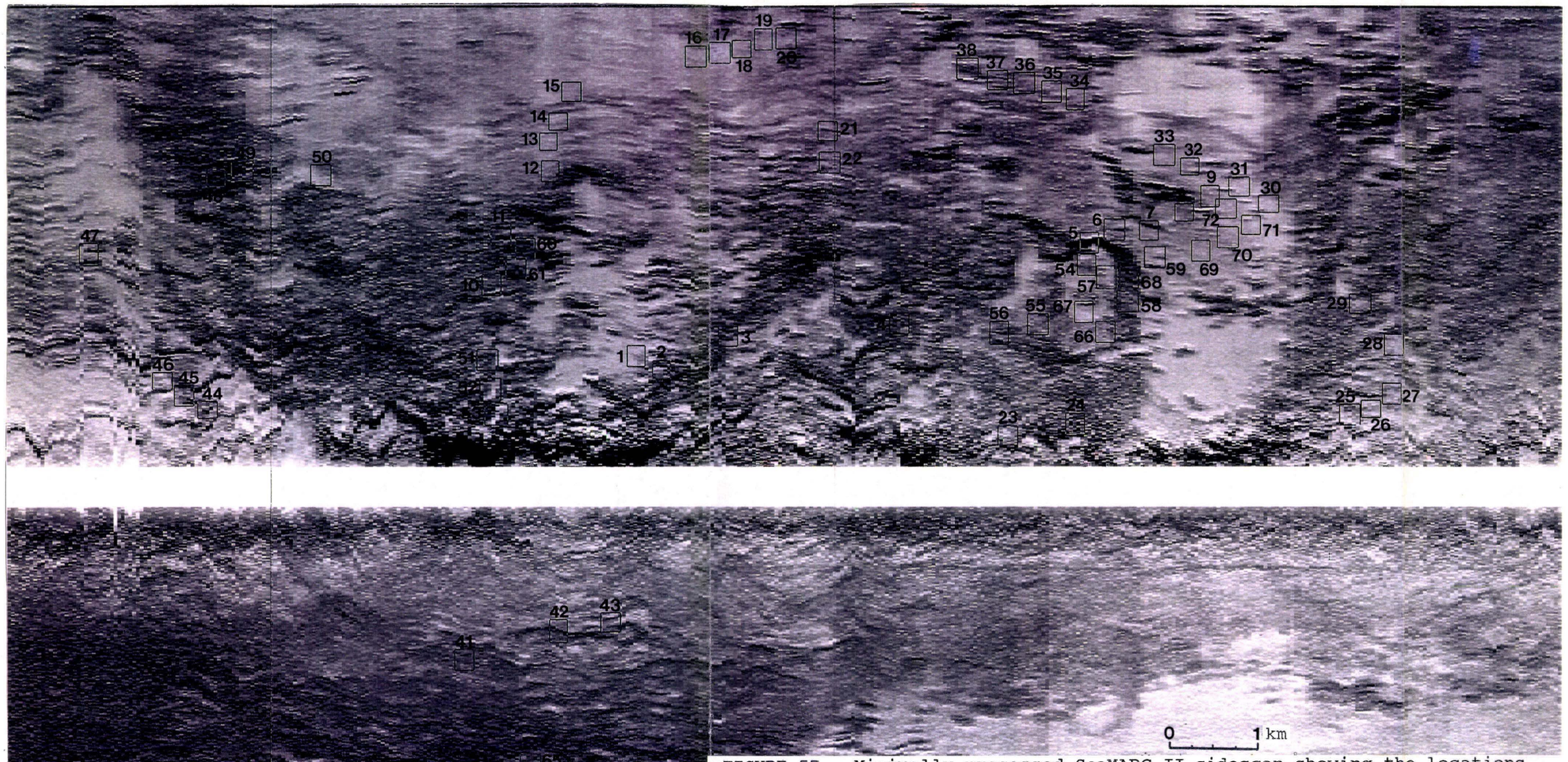

FIGURE 57. Minimally processed SeaMARC II sidescan showing the locations of the refined set of 112 sample boxes. a) The first 72 samples boxes from the bottom swath of the survey are shown here. b) and c) display the samples from the top swath of the survey, viewed from a different look direction. Great pains were taken for the accurate placement of boxes and a uniform size of about 160-200 pixels. Descriptions, first and second-order statistics for each box are shown in Table 1.

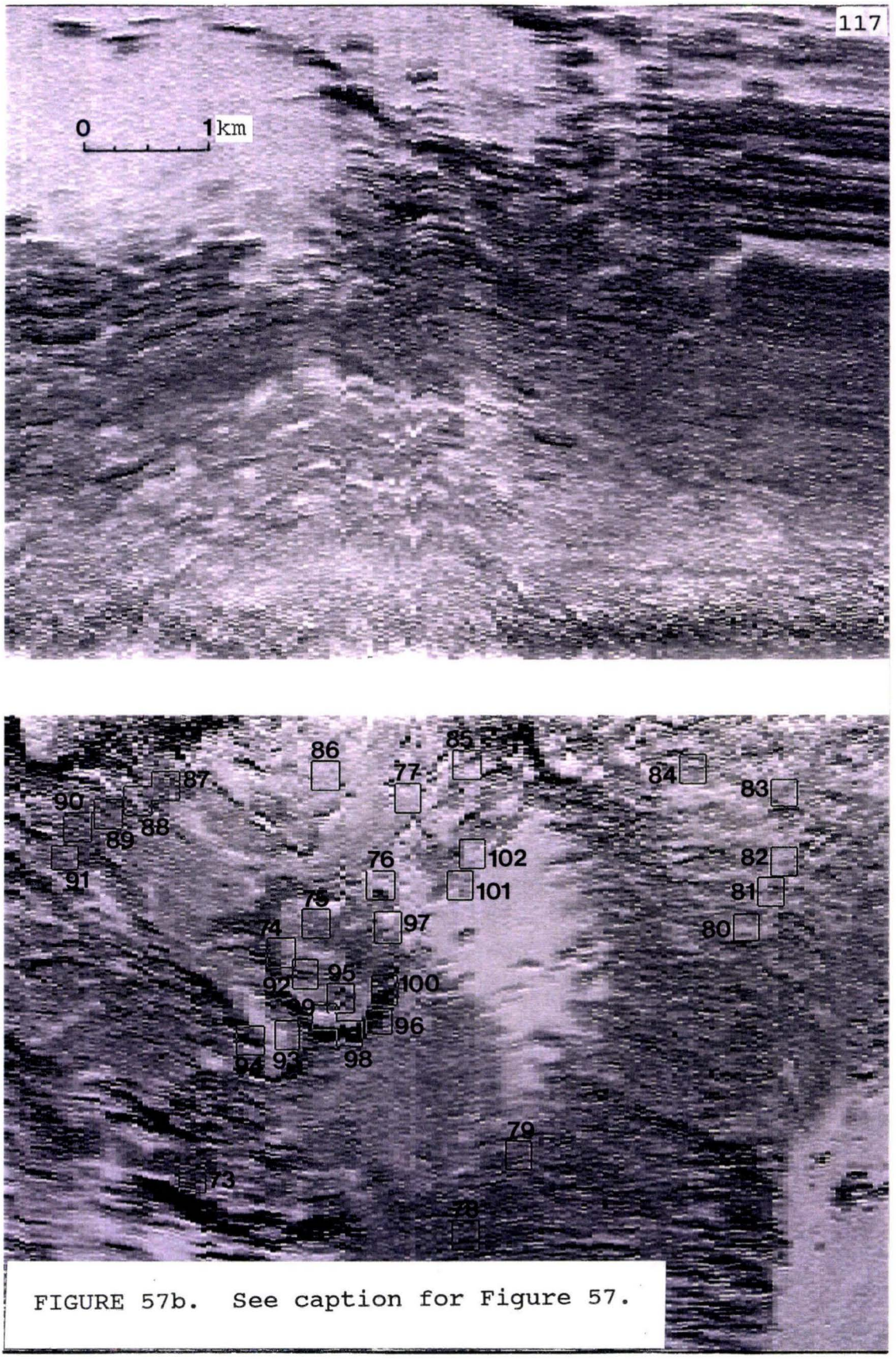

FIGURE 57b. See caption for Figure 57.

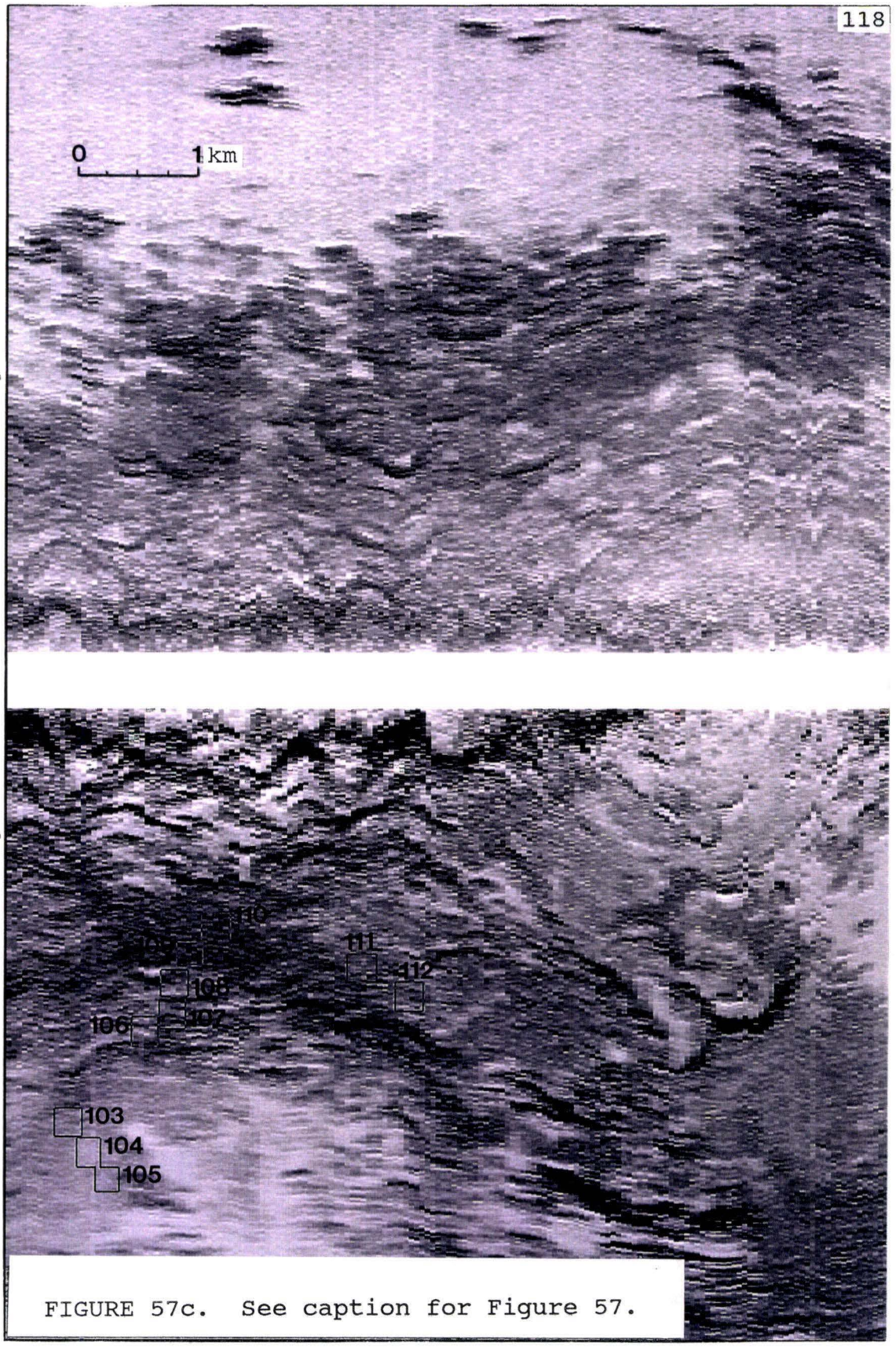

FIGURE 57c. See caption for Figure 57.

gradient measurements were obtained from Figure 58, a slope map derived from the composite SeaBeam/SeaMARC II bathymetric data. Sample boxes were picked using a textural analysis program, developed by Tom Reed at the Hawaii Institute of Geophysics, called "get_tex". This program displays the minimally-processed SeaMARC II sidescan image (mentioned in the SeaMARC II section) and allows boxes to be picked using the mouse. Second-order image statistics for the area within each sample box are then generated by the grey level co-occurrence matrix method discussed in the Texture Features section.

Plots of the means and ranges of each lithology (Figure 59) showed that our estimates of image texture from SeaMARC II are apparently capable of discriminating among several seafloor lithologies. This preliminary study determined that SeaMARC II could distinguish differences in regions that camera data portrayed as pillow basalt, hyaloclastite and sediment/talus. The acoustic similarity between sediment and talus could be due to thin layers of sediment overlying talus. Acoustic penetration of the thin sediment layer would return the characteristics of talus. Another possible explanation is that at the scale of 12 cm (the wavelength of insonification), talus presenting facets 1 to 10 m in major dimension would appear equally as rough/smooth as flat-lying sediments. Signal amplitude from the talus would be greater, but the coherence might be the same as that of a pond of sediment. As texture,

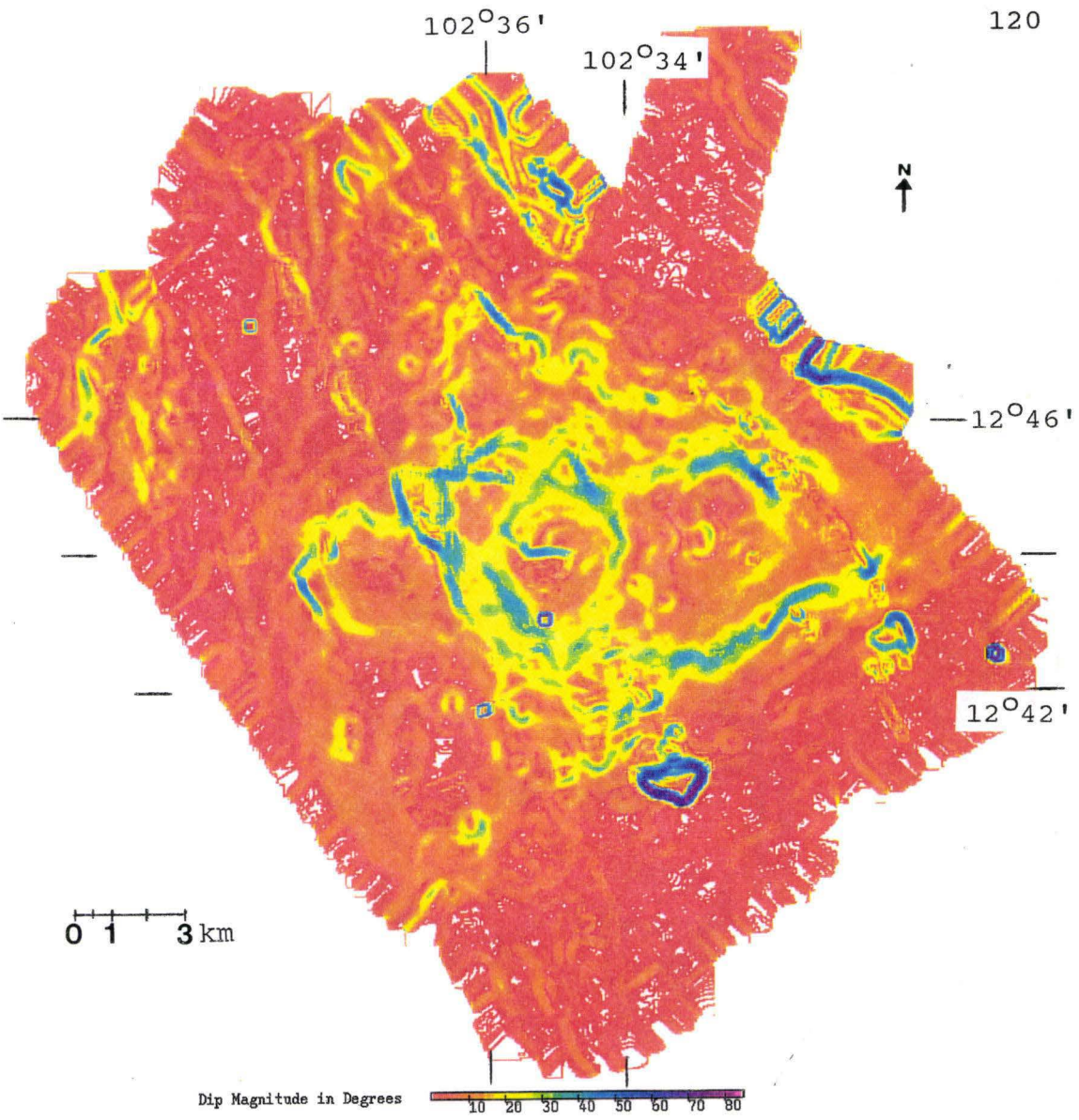

FIGURE 58. Digital slope magnitude map of Seamount 6 derived from the composite SeaBeam/SeaMARC II bathymetric data. Subtle color changes are at 2° intervals of slope angle.

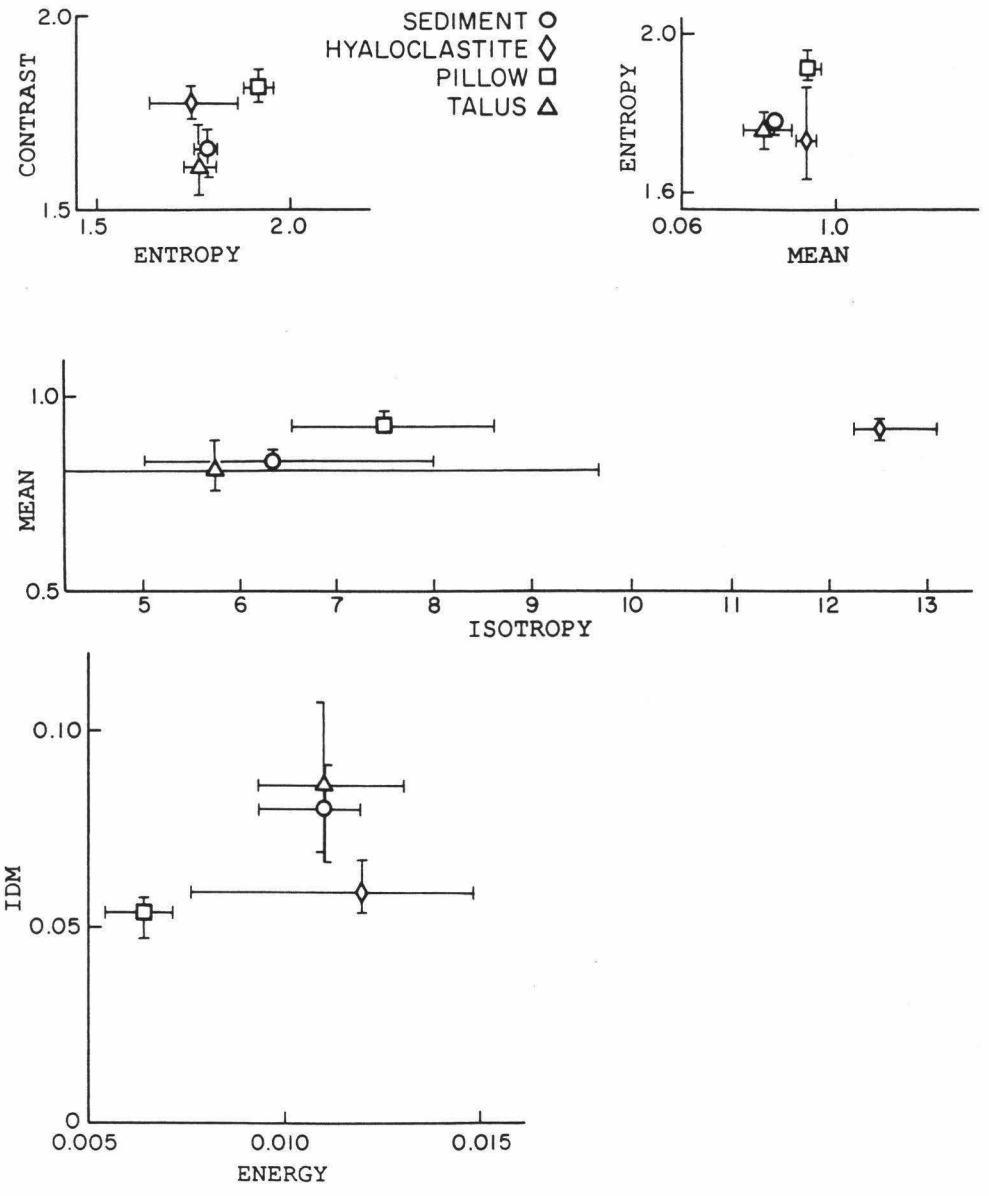

FIGURE 59. Plots of means and ranges of second-order statistics generated from the sample boxes in Figure 43. Plotted values for pillows = the mean of boxes 9, 10, 11, 12; for sediment = mean of boxes 1, 2, 3, 4; for hyaloclastite = mean of boxes 5, 6, 7, 8; for talus = mean of boxes 13, 14, 15, 16.

Note that second-order statistics apparently can clearly distinguish between some lithologies, such as pillows and hyaloclastite.

expressed by our grey level co-occurrence matrix features, is largely independent of image amplitude, these two lithologies might be difficult to separate texturally.

The next step was to test the system with more variable sample areas. 142 locations were chosen, varying in lithology, bottom roughness, bottom slope gradient, and look angle. Due to a turn in our SeaMARC II survey data (Figure 46a), a small portion of Seamount 6 is viewed from two different look directions. 50 of these 142 samples are duplicate locations viewed from a different look direction (look angle will also be different, as this is calculated from water depth and distance from nadir). Roughness was estimated from the films and photographs according to a scale I devised based on geology (Appendix B). Descriptive variables along with first and second-order image statistics, generated by the updated "ss_get" program (which operates the same as "get_tex" but has some added features and was developed by Tom Reed at the Hawaii Institute of Geophysics), for each sample area were evaluated by using clustering routines based on Hartigan's [1975] K-means algorithm. Initial attempts at clustering the data were not terribly encouraging. Distinct classes did not emerge from the data.

Upon further review of the ALVIN and ANGUS films and photographs, I eliminated several sample locations as being ambiguous in lithology, having too low a percentage of the intended lithology, or being too limited in lateral extent.

In addition, it was determined that some sample locations were mislocated. The locations of the refined set of 112 sample boxes are shown in Figure 57. Descriptive variables and first and second-order statistics for each box are summarized in Table 1. Details about each entry in Table 1 are in Appendix C. The next section is a discussion of the results obtained in endeavors at classification of the data from this set of samples.

RESULTS AND DISCUSSION

Supervised and unsupervised classifications of the data from the refined set of 112 samples were attempted. Unsupervised classification took the form of several clustering scenarios changing certain variables. Variables in these permutations include the method of assigning initial centroids (discussed previously in the Classification section), number of samples and number of classes. For a supervised classification, ALVIN and ANGUS dive films and photographs were used to assign each sample area to a specific lithologic class, as discussed in the Classification section.

A supervised classification of the 112 samples resulted in the plots shown in Figure 60. Stars in the plots are the means of the second-order statistics while the error bars represent standard deviation. As can be seen, no

TABLE 1. Sample location descriptors. Long=longitude, Lat=latitude, Mean I=mean intensity, MAD=mean absolute deviation, Std=standard deviation, Var=variance, Skew=skewness, Kurt=kurtosis, Rough=roughness, IDM=inverse difference moment, Corr=correlation. Each entry is explained in Appendix C.

SAMPLE #	LOCATION (key'd to dive)	NADIR LONG (W)	NADIR LAT (N)	DISTANCE FROM NADIR (meters)	SHIP HEADING	LONG (W)	LAT (N)	VOLCANO	GEOLOGY	BOX SIZE (pixels)	MEAN I	MAD	STD	VAR	SKEW	KURT	SLOPE ANGLE (deg) min	SLOPE ANGLE (deg) max	LOOK ANGLE	ROUGH	WATER DEPTH (m)	CONTRAST	IDM	ENTROPY	ENERGY	MEAN	CORR	ISOTROPY	SAME AS BOX
1	1.219.521-532	257.4333	12.7053	1200	249.5	257.4347	12.7159	020	8221000000	160	41.168751	12.266935	14.843510	220.329788	0.388150	-0.123274	20	25	31.1	9	1990	1.9017	0.1625	3.1270	0.0398	1.0144	288.5852	11.2878	
2	1.219.557-605	257.4352	12.7061	1050	249.4	257.4358	12.7155	020	6244000000	128	107.390625	39.930664	49.823215	2482.352783	0.242829	-0.602691	20	25	26.6	8.5	2100	2.4669	0.0527	3.7746	0.0140	1.3519	1662.3832	57.3697	
3	1.219.643-651	257.4392	12.7075	1400	249.6	257.4416	12.7195	020	723D000000	160	99.837502	35.014549	41.740864	1742.299683	0.297584	-0.720093	15	20	33.1	8.5	2150	2.3017	0.0633	3.6914	0.0163	1.2680	889.8846	35.2293	
4	1.219.805-812	257.4507	12.7116	1550	248.8	257.4548	12.7239	020	8229000000	160	99.943748	23.418045	29.283745	857.537720	0.204037	-0.152223	10	15	47.3	8	2260	2.5724	0.0527	3.8130	0.0134	1.3908	2669.1499	77.1658	73
5	1.219.1041-1057	257.4628	12.7159	2450	247.9	257.4762	12.7198	004	001FAA0000	160	120.425003	62.414074	71.494339	5111.440430	0.246238	-1.196675	10	15	49.5	4.5	2220	2.2391	0.0907	3.6035	0.0196	1.2147	835.7804	33.4837	74
6	1.219.1057-1106	257.4648	12.7167	2600	247.7	257.4792	12.7172	004	001F00A300	200	75.639999	21.545202	28.605452	818.271851	1.175922	1.525928	5	10	49.1	3	2210	2.2628	0.1135	3.4920	0.0248	1.1999	1142.1360	31.2297	75
7	1.219.1132-1145	257.4668	12.7175	2550	248.4	257.4778	12.7319	004	00A9000000	180	79.744446	30.647652	40.128586	1610.303467	1.456238	1.163727	5	10	51.3	3	2205	1.9398	0.1236	3.2852	0.0316	1.0683	253.7508	10.3788	76
8	1.219.1151-1220	257.4692	12.7183	2750	251.0	257.4843	12.7217	004	00A9000000	160	73.562500	12.048437	16.408575	269.241364	0.074596	2.593035	5	10	53.2	3	2205	1.9056	0.1360	3.2500	0.0328	1.0505	219.5074	14.3862	77
9	1.219.1151-1220	257.4715	12.7191	2950	251.1	257.4874	12.7253	004	00A9000000	200	57.759998	11.520000	15.311255	234.434540	0.350764	1.410622	5	10	45.9	9	1890	2.3276	0.0714	3.7086	0.0160	1.2643	1173.8854	38.6748	
10	1.220.437-455	257.4240	12.7019	1950	249.7	257.4283	12.7180	020	7221001212	200	102.830002	29.009802	37.541550	1409.368042	0.311298	0.315640	10	15	54.1	9.5	1810	2.4214	0.0585	3.7626	0.0143	1.3194	1460.9445	47.3415	
11	1.220.502-511	257.4247	12.7022	2500	249.4	257.4262	12.7246	030	9211000000	160	124.631248	37.330551	45.996948	2115.719238	0.498488	-0.153601	10	15	62.0	4.5	1700	1.9894	0.1261	3.3139	0.0305	1.0859	325.2623	15.6439	
12	1.220.547-554	257.4274	12.7032	3200	249.0	257.4325	12.7308	040	0051000051	160	79.237503	16.229698	21.988131	483.477844	1.153315	1.597312	10	15	64.1	4	1710	1.4681	0.2115	2.7132	0.0637	0.8492	32.2801	2.8838	105
13	1.220.558-630	257.4284	12.7035	3525	249.0	257.4340	12.7339	040	0021009100	160	51.299999	5.168750	6.773794	45.884285	-0.294398	0.281249	0	5	64.1	4	1710	1.4681	0.2115	2.7132	0.0637	0.8492	32.2801	2.8838	105
14	1.220.558-630	257.4286	12.7036	3750	249.0	257.4346	12.7359	040	0021009100	128	51.359375	11.489258	13.927099	193.964096	0.615807	-0.446164	5	10	65.0	4	1750	1.8076	0.1357	3.1034	0.0391	1.0165	121.4189	10.6061	104
15	1.220.558-630	257.4291	12.7038	4075	248.5	257.4452	12.7296	040	0021009100	180	46.938889	5.758397	7.722249	59.633125	1.153332	1.815637	10	15	66.3	4	1785	1.6208	0.2180	2.7774	0.0631	0.8876	81.1155	7.4640	103
16	1.220.722-736	257.4365	12.7065	4475	249.7	257.4463	12.7435	020	0021008300	200	48.334999	7.852099	10.768126	115.952538	1.424011	2.306805	20	25	66.9	4	1905	1.6344	0.2031	2.8752	0.0564	0.9084	80.9260	4.5772	106
17	1.220.722-736	257.4375	12.7068	4500	249.6	257.4451	12.7454	020	0021008300	200	43.165001	4.113050	5.332914	28.439970	0.761223	1.036565	25	30	66.6	4	1950	1.3472	0.2534	2.5175	0.0812	0.7831	21.8007	2.3537	107
18	1.220.722-736	257.4387	12.7073	4525	251.1	257.4631	12.7169	020	0021008300	128	52.921875	6.527588	8.421567	70.922783	0.559974	0.386139	30	35	66.3	4	1990	1.5260	0.1892	2.7796	0.0579	0.8815	38.8703	5.0182	108
19	1.220.737-755	257.4402	12.7079	4650	250.3	257.4620	12.7302	020	711F410000	160	69.112503	8.943281	11.849150	140.402344	1.090056	1.693576	35	40	65.8	8	2090	1.6837	0.1643	2.9882	0.0451	0.9498	82.0005	5.6732	109
20	1.220.759-807	257.4421	12.7085	4650	250.3	257.4639	12.7308	020	001100A100	200	72.889999	12.943496	16.474068	271.394897	0.650354	0.122942	25	30	64.4	5	2230	1.8480	0.1377	3.2239	0.0339	1.0304	165.9672	9.9309	110
21	1.220.845-900	257.4457	12.7097	3650	250.1	257.4603	12.7324	020	0024880000	144	77.750000	20.954861	26.431993	698.650330	0.800178	0.051740	25	30	59.0	8	2190	2.1225	0.0985	3.4630	0.0245	1.1631	484.5270	26.1297	111
22	1.220.906-915	257.4465	12.7100	3300	250.1	257.4597	12.7305	020	0031780000	200	84.764999	19.233248	32.636468	572.954529	0.328073	-0.456189	20	25	58.5	7.5	2020	2.1515	0.0959	3.5433	0.0213	1.1838	517.3090	28.6585	112
23	1.221.355-400	257.4573	12.7139	325	251.8	257.4584	12.7163	002	0044000063	180	58.333332	25.744438	32.636475	1065.139526	0.476102	-0.080634	10	15	7.7	5	2390	2.2941	0.0630	3.7060	0.0158	1.2617	890.0989	36.7793	78
24	1.221.428-432	257.4618	12.7155	450	247.9	257.4643	12.7162	002	0054000053	160	105.599998	34.872501	43.011501	1849.989380	0.109865	-0.383707	15	20	10.5	5	2420	2.4604	0.0515	3.8177	0.0129	1.3450	1735.3793	66.3219	79
25	1.221.642-702	257.4819	12.7226	550	251.1	257.4849	12.7238	002	14A4000000	160	54.275002	23.894371	29.388083	863.659424	0.557844	-0.166972	5	10	12.2	2	2550	2.2347	0.0952	3.5668	0.0204	1.2081	902.0443	40.3122	80
26	1.221.642-702	257.4833	12.7231	625	251.1	257.4867	12.7244	002	14A4000000	160	39.787498	14.929537	18.567366	344.747040	0.464190	-0.178796	5	10	13.7	2	2570	1.9846	0.1040	3.3645	0.0272	1.1109	229.9609	21.8737	81
27	1.221.642-702	257.4848	12.7235	800	251.1	257.4891	12.7252	002	14A4000000	160	50.275002	15.799063	19.522272	381.119080	0.313986	-0.602769	5	10	17.3	2	2575	2.0320	0.1030	3.4552	0.0237	1.1336	291.3101	19.1463	82
28	1.221.726-738	257.4851	12.7236	1325	251.1	257.4922	12.7264	002	00A4000000	200	43.645000	9.911101	12.978876	168.451218	1.105834	1.692150	10	15	27.2	2.5	2575	1.9400	0.1412	3.2788	0.0315	1.0569	279.6996	10.7236	83
29	1.221.749-804	257.4827	12.7229	1750	251.1	257.4921	12.7266	002	00A4000000	180	76.788887	23.928633	29.490265	869.675720	0.514767	-0.148690	10	15	34.6	2.5	2540	2.1298	0.0816	3.5586	0.0201	1.1848	424.2127	24.0541	84
30	1.221.907-947	257.4756	12.7204	2850	252.1	257.4808	12.7446	003	00A9000000	160	42.337502	9.338911	13.484622	181.835022	1.871640	3.993479	20	25	52.1	2.5	2220	1.8776	0.1784	3.0596	0.0446	1.0035	259.7064	14.4697	85
31	1.221.907-947	257.4735	12.7197	3050	252.1	257.4790	12.7456	003	00A9000000	180	41.688889	7.383706	11.033362	121.735077	1.980081	7.030303	20	25	54.3	2.5	2195	1.8578	0.1769	3.0296	0.0456	0.9903	242.7225	11.3018	
32	1.221.959-1022	257.4698	12.7185	3250	251.1	257.4873	12.7254	004	00AD000000	128	58.632812	17.567139	22.956289	526.991211	0.893462	0.979310	10	15	56.0	2	2190	2.0658	0.1195	3.3689	0.0293	1.1295	394.3520	22.2909	
33	1.221.959-1022	257.4679	12.7178	3375	251.0	257.4864	12.7220	004	00AD000000	200	48.889999	9.475701	11.366347	129.193848	0.582863	-0.378967	10	15	57.0	2	2190	1.6182	0.1863	2.9089	0.0513	0.9139	64.3172	6.3089	86
34	1.221.1044-1120	257.4618	12.7155	4000	247.9	257.4836	12.7219	002	9324000000	160	64.981247	15.753897	19.354511	374.597076	0.762564	-0.139239	25	30	59.0	9	2400	1.9748	0.1199	3.3333	0.0299	1.0941	252.6054	19.0829	87
35	1.221.1044-1120	257.4605	12.7150	4050	250.8	257.4829	12.7173	002	9324000000	160	60.612499	16.472971	19.988670	399.546936	0.048480	-0.617728	25	30	59.3	9	2400	2.0138	0.1144	3.3767	0.0279	1.1154	274.6494	22.8146	88
36	1.221.1044-1120	257.4588	12.7144	4150	251.1	257.4812	12.7232	002	9324000000	200	76.239998	14.128798	18.577888	345.137970	0.486081	0.359402	25	30	60.0	9	2400	1.9395	0.1306	3.3235	0.0293	1.0748	235.0459	12.8740	89
37	1.221.1044-1120	257.4573	12.7139	4200	250.6	257.4798	12.7237	002	9324000000	180	82.650002	22.759989	28.196327	795.032898	0.349718	-0.314329	25	30	60.3	9	2400	2.1146	0.0881	3.5199	0.0218	1.1731	394.7553	25.8559	90
38	1.221.1044-1120	257.4554	12.7132	4350	250.6	257.4787	12.7234	002	9324000000	200	79.614998	27.497353	33.797455	1142.268066	-0.402584	-0.470046	25	30	61.1	9	2400	2.1758	0.0856	3.5856	0.0198	1.2012	506.1248	31.6220	91
39	1.222.740-803	257.4111	12.6973	3950	249.0	257.3905	12.6851	010	00A3000000	176	144.142044	25.239477	31.450954	989.162476	-0.241014	-0.495047	5	10	52.6	2	3020	2.2484	0.0741	3.6383	0.0179	1.2347	742.9330	33.5689	
40	1.222.740-803	257.4138	12.6983	4000	250.6	257.4056	12.6649	010	00A3000000	200	147.369995	25.901106	33.025387	1090.676147	0.060419	0.084599	5	10	52.8	2	3035	2.2029	0.0741	3.6337	0.0179	1.2164	614.9310	23.9797	
41	1.222.1038-1052	257.4228	12.7015	1600	250.6	257.4195	12.6881	010	7B3300000	200	107.014999	13.605893	17.136309	293.653076	0.061055	-0.111774	5	10	30.2	8	2750	1.9754	0.1052	3.4003	0.0259	1.1049	240.0797	12.8780	
42	1.222.1120-1135	257.4282	12.7034	1300	249.0	257.4214	12.6994	010	7B3F000000	176	103.409088	21.921486	27.849655	775.603333	0.874908	0.654610	10	15	26.6	9	2600	2.1766	0.0826	3.5595	0.0205	1.1919	636.2289	26.9378	
43	1.222.1154-1200	257.4315	12.7047	1200	249.9	257.4294	12.6945	010	882F000000	180	84.088890	24.695801	31.153305	970.528442	-0.041279	-0.472193	20	25	24.4	9	2640	2.2581	0.0654	3.6652	0.0170	1.2478	703.2390	34.3649	
44	1.223.400-419	257.4048	12.6949	600	249.9	257.4067	12.6993	010	14A5000000	128	84.210938	30.034180	37.646454	1417.255493	0.369982	-0.418306	5	10	12.1	2	2810	2.3124	0.0621	3.6719	0.0170	1.2713	956.1440	45.3576	
45	1.223.420-429	257.4035	12.6945	750	249.6	257.4048	12.7009	010	14A5000000	160	100.806252	34.482399	43.885712	1925.955811	0.674397	-0.181578	5	10	14.9	2	2820	2.3880	0.0619	3.7346	0.0153	1.3002	1423.8579	42.1219	
46	1.223.429-435	257.4018	12.6939	900	249.6	257.4033	12.7016	010	842F000000	160	56.831249	20.302191	24.960649	623.033997	0.145032	-0.639788	5	10	17.7	8.5	2820	2.2046	0.0812	3.5617	0.0202	1.2048	703.9814	32.7576	
47	1.223.549-601	257.3966	12.6919	2300	247.9	257.4092	12.6956	200	00A5000000	160	89.937500	36.026562	42.377674	1795.867188	0.610516	-0.623715	5	10	50.2	2	2760	2.3659	0.0689	3.6955	0.0165	1.2930	1124.3135	46.4195	
48	1.223.802-812	257.4059	12.6953	3125	249.9	257.4158	12.7184	020	0014970000	160	143.850006	17.636253	21.546556	464.254089	-0.059745	-0.646890	35	40	49.9	9	2630	2.0957	0.0871	3.5210	0.0217	1.1679	369.4101	19.7475	
49	1.223.802-812	257.4075	12.6960	3200	248.9	257.4143	12.7226	020	0014970000	180	130.294449	30.911421	38.027874	1446.119263	0.000966	-0.489546	35	40	51.2	9	2570	2.2384	0.0674	3.7196	0.0156	1.2807	1110.5146	36.5766	
50	1.223.856-925	257.4123	12.6978	3150	250.6	257.4292	12.7052	020	9A2400000	200	53.564999	16.048443	19.545738	382.035889	0.612496	-0.371680	20	25	55.2	10	2190	1.9337	0.1431	3.2386	0.0341	1.0539	271.6344	16.4390	
51	1.223.1103-1108	257.4237	12.7018	1150	250.6	257.4299	12.7045	020	8B390000000	200	91.625000	27.682501	33.927864	1151.099854	-0.269419	-0.596874	10	15	29.7	9	2020	2.2544	0.0682	3.6954	0.0160	1.2456	723.7784	32.1260	
52	1.223.1111-1126	257.4243	12.7020	850	250.6	257.4289	12.7040	020	001FA30000	220	76.468185	28.487530	34.073162	1160.980469	0.011798	-0.827590	15	20	22.0	9	2100	2.3083	0.0674	3.7354	0.0151	1.2683	929.2690	32.7815	
53	1.223.1132-1203	257.4245	12.7021	550	250.6	257.4274	12.7034	020	9314000000	200	92.044998	47.673199	56.238926	3162.816895	0.101089	-0.893610	20	25	13.9	9	2230	2.4740	0.0541	3.8415	0.0125	1.3490	1901.0908	55.6504	
54	2.1387.1625.23-1636.59	257.4628	12.7159	2175	247.9	257.4747	12.7194	004	002F930000	160	71.056252	15.654135	20.576975	423.411865	-0.204494	-0.125173	20	25	43.6	9	2280	1.9411	0.1040	3.3576	0.0271	1.0917	195.2480	12.6829	92
55	2.1387.2111.12-2125.40	257.4596	12.7147	1550	250.8	257.4682	12.7156	004	00AD000000	220	69.084999	14.526699	18.826309	354.429932	0.071312	-0.014309	10	15	33.7	3	2320	1.9785	0.1074	3.4146	0.0252	1.1065	244.9438	14.2439	93
56	2.1387.2127.53-2139.09	257.4573	12.7139	1450	250.6	257.4651	12.7173	004	4A1F6B0000	220	92.472725	24.266939	28.593102	817.565491	0.160409	-0.914467	15	20	31.9	9	2330	2.1684	0.0874	3.6042	0.0190	1.2012	500.9788	26.2370	94
57	2.1388.1606.14-1624.34	257.4641	12.7164	2050	247.7	257.4755	12.7168	004	00AD000011	220	71.622726	19.812275	24.284431	589.733582	0.446823	-0.158372	25	30	41.3	3.5	2330	2.1038	0.0955	3.5540	0.0204	1.1671	408.4131	19.1556	95
58	2.1388.1850.35-1935.37	257.4655	12.7170	1800	248.4	257.4733	12.7272	004	8A390000000	200	92.805000	18.373053	22.463753	504.620209	0.172141	-0.560338	5	10	38.7	8	2250	2.0803	0.0841	3.5144	0.0218	1.1649	325.6463	18.4797	96
59	2.1388.2122.49-2129.38	257.4671	12.7176	2275	248.4	257.4769	12.7305	004	001F9B0000	160	58.306252	22.745058	30.587336	935.585083	1.478553	1.426204	0	5	45.8	9	2215	2.1638	0.1050	3.4852	0.0238	1.1736	632.6423	29.5512	97
60	2.1389.1636.54-1700.25	257.4262	12.7027	2350	249.7	257.4314	12.7221	030	9311000000	200	128.630005	28.253704	36.486427	1331.259399	-0.102515	0.058110	5	10	49.6	10	1810	2.2592	0.0732	3.6844	0.0167	1.2477	714.8123	33.7967	
61	2.1389.1636.54-1700.25	257.4257	12.7025	2125	249.7	257.4304	12.7201	030	9311000000	200	124.480003	32.415199	40.406597	1632.693115	0.335413	-0.443668	5	10	49.1	10	2950	2.0736	0.0892	3.4872	0.0228	1.1547	351.8988	19.7252	
62	2.1390.1922.35-1950	257.4177	12.6997	3400	249.7	257.4083	12.6732	010	A31F000000	180	147.561111	21.016106	27.011723	729.633118	-0.548750	-0.380986	25	30	46.7	10	2950	1.9662	0.1227	3.3233	0.0288	1.0770	297.6921	12.6000	
63	2.1390.2000-2020	257.4218	12.7011	3125	250.4	257.4187	12.6734	010	931F000000	160	163.706253	11.951098	14.485558	209.831390	-0.169813	-0.567220	25	30	46.1	10	2890	2.1720	0.0836	3.5596	0.0203	1.1967	570.1196	23.4780	
64	2.1390.2000-2020	257.4235	12.7017	3000	250.6	257.4173	12.6766	010	931F000000	160	123.306252	21.461098	27.851805	775.723022	0.358041	0.326261	25	30	43.1	2	2890	2.2458	0.0783	3.6367	0.0183	1.2323	744.3237	33.6138	
65	2.1390.2030-2100	257.4264	12.7028	2700	249.4	257.4154	12.6862	010	00A4000000	200	98.605003	28.920803	34.905891	1218.421143	-0.150268	-0.556265	20	25	31.9	8	2330	2.0285	0.1044	3.4465	0.0241	1.1229	334.6567	15.7683	98
66	2.1391.1637.30-1643.25	257.4638	12.7163	1450	247.7	257.4718	12.7166	004	0012920000	200	66.750000	18.652500	23.494841	552.007507	0.475173	-0.271072	20	25	35.2	3	2335	2.0324	0.1476	3.2833	0.0328	1.0837	464.2070	17.0325	99
67	2.1391.1750.06-1754.03	257.4623	12.7157	1650	247.9	257.4713	12.7183	004	00AD000000	200	51.075001	21.304981	30.991001	960.442139	2.069654	3.991691	10	15	42.3	9	2250	2.1971	0.0724	3.6442	0.0175	1.2154	590.4558	27.5122	100
68	2.1391.1809.18-1822.06	257.4655	12.7170	2050	248.4	257.4743	12.7286	004	001F930000	200	124.915001	24.231600	31.240963	975.997803	-0.116514	0.111512	20	25	46.8	3	2205	1.5300	0.1858	2.7745	0.0579	0.8791	41.5201	3.4244	101
69	2.1391.1842.56-1904.08	257.4704	12.7187	2350	251.1	257.4831	12.7237	004	00A9000000	160	45.587502	6.108125	7.582990	57.501732	0.298046	-0.120353	0	5	48.6	3	2205	1.6799	0.1790	2.9251	0.0507	0.9311	96.3269	8.6301	102
70	2.1391.1842.56-1904.08	257.4727	12.7195	2500	250.5	257.4857	12.7275	004	00A9000000	200	47.924999	6.823249	9.161829	83.939102	-0.719931	2.693217	0	5	48.6	3	2200	1.6514	0.2145	2.8145	0.0612	0.9041	94.5004	7.0649	
71	2.1391.1905.27-1911.13	257.4744	12.7200	2625	252.1	257.4792	12.7423	004	8321000000	144	42.451389	7.733603	11.480496	131.801804	1.722009	4.823605	5	10	50.0	9	2200	1.6514	0.2145	2.8145	0.0612	0.9041	94.5004	7.0649	
72	2.1391.1933.06-1947.00	257.4727	12.7195	2800	250.5	257.4872	12.7284	004	00AC000000	180	47.638889	6.987345	9.194827	84.544853	0.199218	0.885304	15	20	51.8	3	2200	1.6784	0.1781	2.9602	0.0480	0.9401	86.7333	8.6712	

TABLE 1. (Continued) Sample location descriptors.

SAMPLE #	LOCATION (key'd to dive)	NADIR LONG (W)	NADIR LAT (N)	DISTANCE FROM NADIR (meters)	SHIP HEADING	LONG (W)	LAT (N)	VOLCANO	GEOLOGY	BOX SIZE (pixels)	MEAN I	MAD	STD	VAR	SKEW	KURT	SLOPE ANGLE (deg) min	SLOPE ANGLE (deg) max	LOOK ANGLE	ROUGH	WATER DEPTH (m)	CONTRAST	IDM	ENTROPY	ENERGY	MEAN	CORR	ISOTROPY	SAME AS BOX
73	1.219.805-812					257.4548	12.7239	020	8229000000	160	118.812500	22.898281	28.658039	821.283203	0.193171	-0.062309	10	15	58.2	7	2260	2.2342	0.0745	3.6338	0.0181	1.2285	730.2701	27.0634	4
74	1.219.1041-1057					257.4762	12.7198	004	001FAA0000	200	92.570000	30.391369	37.273743	1389.332031	0.617360	0.005456	10	15	39.7	8	2260	2.1276	0.0884	3.5384	0.0211	1.1720	492.8726	25.5163	5
75	1.219.1057-1106					257.4792	12.7172	004	001F00A300	160	72.356247	14.033986	17.441854	304.218262	-0.271806	-0.196392	5	10	36.6	4.5	2220	1.9113	0.1144	3.3156	0.0291	1.0717	188.9575	13.6195	6
76	1.219.1132-1145					257.4778	12.7319	004	00A9000000	160	60.293751	32.561253	41.841362	1750.699707	1.390886	0.862560	5	10	31.4	3	2210	2.2121	0.1094	3.4835	0.0242	1.1824	919.9017	23.8780	7
77	1.219.1151-1220					257.4843	12.7217	004	00A9000000	160	34.387501	8.029840	11.363065	129.119247	1.149137	3.361884	5	10	16.4	3	2205	1.9226	0.1659	3.1136	0.0410	1.0172	328.5735	11.8244	8
78	1.221.355-400					257.4584	12.7163	002	0044000063	160	108.081253	17.312344	21.548822	464.351746	0.221171	-0.577801	10	15	59.6	5	2390	2.0294	0.0942	3.4606	0.0236	1.1342	288.9878	17.7512	23
79	1.221.428-432					257.4643	12.7162	002	0054000053	160	89.131248	15.096016	18.724453	350.605164	0.539541	0.184779	15	20	55.0	5	2420	1.9725	0.1052	3.3493	0.0283	1.0948	264.5266	14.7073	24
80	1.221.642-702					257.4849	12.7238	002	14A4000000	180	57.905556	15.340987	18.681898	349.013336	0.270283	-0.436191	5	10	33.3	2	2550	2.0103	0.1117	3.3548	0.0282	1.1057	308.8614	15.3423	25
81	1.221.642-702					257.4867	12.7244	002	14A4000000	160	55.737499	20.344841	25.232624	636.685303	1.045060	0.601802	5	10	28.6	2	2570	2.0233	0.1145	3.4009	0.0267	1.1147	341.2324	16.8390	26
82	1.221.642-702					257.4891	12.7252	002	14A4000000	200	45.490002	11.672696	14.421509	207.979904	1.000619	0.473210	5	10	24.1	2	2575	1.8898	0.1409	3.2805	0.0310	1.0507	194.0792	11.7683	27
83	1.221.726-738					257.4922	12.7264	002	00A4000000	180	49.005554	15.906363	20.053980	402.162109	1.006790	1.491645	10	15	13.1	2.5	2575	2.0152	0.1110	3.3699	0.0269	1.1049	354.1071	12.8333	28
84	1.221.749-804					257.4921	12.7266	002	00A4000000	200	60.099998	20.993999	27.209030	740.331360	0.706682	0.188209	10	15	9.5	2.5	2540	2.1987	0.0789	3.6067	0.0190	1.2079	655.2794	27.0244	29
85	1.221.907-947					257.4808	12.7446	003	00A9000000	160	45.118752	24.463888	32.974621	1087.325562	1.685790	3.876196	20	25	9.6	2.5	2220	2.2715	0.0954	3.5792	0.0203	1.2224	1058.5592	40.3512	30
86	1.221.959-1022					257.4864	12.7220	004	00A0000000	200	30.809999	8.377196	11.768018	138.486252	2.134522	9.049828	10	15	12.2	2	2190	1.7409	0.1748	2.9727	0.0479	0.9529	135.8604	8.6585	33
87	1.221.1044-1120					257.4836	12.7219	002	9324000000	200	86.639999	22.872822	28.388552	805.909912	0.026529	-0.078516	25	30	13.5	9	2400	2.1815	0.0698	3.6238	0.0181	1.2130	514.9497	25.5203	34
88	1.221.1044-1120					257.4829	12.7173	002	9324000000	200	84.864998	28.230165	35.076614	1230.368774	0.513504	-0.321535	25	30	15.2	9	2400	2.2794	0.0653	3.7098	0.0158	1.2567	824.4460	33.9837	35
89	1.221.1044-1120					257.4812	12.7232	002	9324000000	160	95.693748	22.452427	27.975500	782.628601	0.092128	-0.427363	25	30	17.9	9	2400	2.1504	0.0867	3.5835	0.0195	1.1899	506.1347	28.5902	36
90	1.221.1044-1120					257.4798	12.7237	002	9324000000	200	101.589996	20.975899	25.875460	669.539368	0.098668	-0.312961	25	30	20.0	9	2400	2.1830	0.0773	3.6149	0.0185	1.2067	568.5759	26.2195	37
91	1.221.1044-1120					257.4787	12.7234	002	9324000000	128	86.476562	17.071045	21.726267	472.030670	0.180573	-0.396861	25	30	25.1	9	2400	2.0713	0.0837	3.4676	0.0233	1.1569	334.4762	19.3030	38
92	2.1387.1625.23-1636.59					257.4747	12.7194	004	002F930000	160	84.062500	26.228125	33.885769	1148.245239	0.985770	0.547571	20	25	42.0	9	2280	2.1823	0.0948	3.5519	0.0209	1.1941	630.9191	29.4390	54
93	2.1387.2111.12-2125.40					257.4682	12.7156	004	00AD000000	160	60.056252	14.677740	17.624401	310.619537	-0.083388	-0.739384	10	15	47.1	3	2320	1.9838	0.1156	3.3217	0.0294	1.0881	316.7719	19.0146	55
94	2.1387.2127.53-2139.09					257.4651	12.7173	004	4A1F6B0000	200	109.885002	38.764622	45.889767	2105.870850	0.308121	-0.917037	15	20	47.6	9	2330	2.3696	0.0690	3.7465	0.0151	1.2912	1277.7864	41.7439	56
95	2.1388.1606.14-1624.34					257.4755	12.7168	004	00AD000011	200	94.400002	26.018000	34.893524	1217.557983	1.152697	1.709847	25	30	46.6	3.5	2330	2.2941	0.0844	3.6397	0.0185	1.2407	1124.6758	38.6057	57
96	2.1388.1850.35-1935.37					257.4733	12.7272	004	8A39000000	128	150.148438	42.905396	51.453056	2647.416992	0.058548	-0.825161	5	10	46.8	8	2250	2.3618	0.0639	3.6797	0.0167	1.2942	1113.8665	48.5636	58
97	2.1388.2122.49-2129.38					257.4769	12.7305	004	001F9B0000	220	51.222729	22.710644	27.320356	746.401855	0.384544	-0.427382	0	5	36.7	9	2215	2.0888	0.0953	3.5340	0.0213	1.1542	415.7609	19.2815	59
98	2.1391.1637.30-1643.25					257.4718	12.7166	004	0012920000	144	152.138885	72.639290	78.165924	6109.912109	-0.124435	-1.636618	20	25	47.0	8	2330	2.5865	0.0682	3.8196	0.0133	1.3972	3122.0752	81.1243	66
99	2.1391.1750.06-1754.03					257.4713	12.7183	004	00AD000000	144	73.381943	35.922605	47.299088	2237.203613	1.317853	2.127681	10	15	45.5	3	2335	2.4668	0.0594	3.7406	0.0153	1.3322	1917.2034	56.0054	67
100	2.1391.1809.18-1822.06					257.4743	12.7286	004	001F930000	160	136.950006	33.410610	39.317154	1545.838623	-0.158305	-0.839542	20	25	43.7	9	2250	2.3403	0.0679	3.7157	0.0157	1.2822	1115.4456	44.7219	68
101	2.1391.1842.56-1904.08					257.4831	12.7237	004	00A9000000	160	48.381248	11.487810	14.964052	223.922852	0.432443	-0.062961	0	5	31.0	3	2205	1.8677	0.1327	3.2495	0.0315	1.0429	175.0756	12.2000	69
102	2.1391.1842.56-1904.08					257.4857	12.7275	004	00A9000000	160	43.200001	12.654983	15.685905	246.047638	0.676713	-0.379911	0	5	43.6	3	2205	1.9016	0.1398	3.2359	0.0336	1.0461	227.7186	13.9463	70
103	1.220.558-630					257.4452	12.7296	040	0021009100	200	68.970003	9.403500	11.856051	140.565948	0.194645	-0.301105	10	15	61.4	4	1785	1.8500	0.1269	3.2195	0.0334	1.0338	157.4713	13.1423	15
104	1.220.558-630					257.4346	12.7359	040	0021009100	160	49.037498	5.046402	6.241360	38.954578	0.726598	0.171511	5	10	63.4	4	1750	1.4404	0.2234	2.6908	0.0644	0.8359	29.3011	2.8390	14
105	1.220.558-630					257.4340	12.7339	040	0021009100	128	54.742188	5.637329	7.280913	53.011696	0.365762	0.547380	0	5	65.5	4	1710	1.6370	0.1777	2.8485	0.0554	0.9157	78.7104	6.3212	13
106	1.220.722-736					257.4463	12.7435	020	0021008300	200	89.720001	25.077593	30.547787	933.167236	0.235331	-0.436400	20	25	53.2	4	1905	2.1976	0.0795	3.6253	0.0183	1.2128	588.7798	25.3415	16
107	1.220.722-736					257.4451	12.7454	020	0021008300	160	112.512497	26.963440	31.826769	1012.943176	0.336052	-0.779986	25	30	50.9	4	1950	2.2517	0.0723	3.6196	0.0189	1.2420	687.3008	36.1512	17
108	1.220.722-736					257.4631	12.7169	020	0021008300	180	100.427780	29.905552	36.361172	1322.134766	-0.006830	-0.694043	30	35	47.9	4	1990	2.2378	0.0769	3.6434	0.0179	1.2297	720.8217	25.7613	18
109	1.220.737-755					257.4620	12.7302	020	711F410000	128	142.304688	15.493530	18.816807	354.072205	-0.303205	-0.558013	35	40	43.0	8	2090	2.0413	0.0948	3.4383	0.0242	1.1369	312.9533	18.1394	19
110	1.220.759-807					257.4639	12.7308	020	001100A100	200	141.664993	14.581745	18.678795	348.897369	-0.317466	0.008753	25	30	38.1	5	2230	2.0246	0.0952	3.4525	0.0239	1.1297	292.3171	16.0894	20
111	1.220.845-900					257.4603	12.7324	020	0034780000	180	101.166664	16.207399	21.185135	448.809937	0.209243	0.452251	25	30	46.9	8	2190	2.0548	0.1048	3.4846	0.0227	1.1403	352.7409	15.1712	21
112	1.220.906-915					257.4597	12.7305	020	0041680000	200	94.095001	20.059750	25.907185	671.182190	0.435064	0.572141	20	25	48.7	7.5	2020	2.1143	0.0875	3.5426	0.0210	1.1708	433.6318	19.6463	22

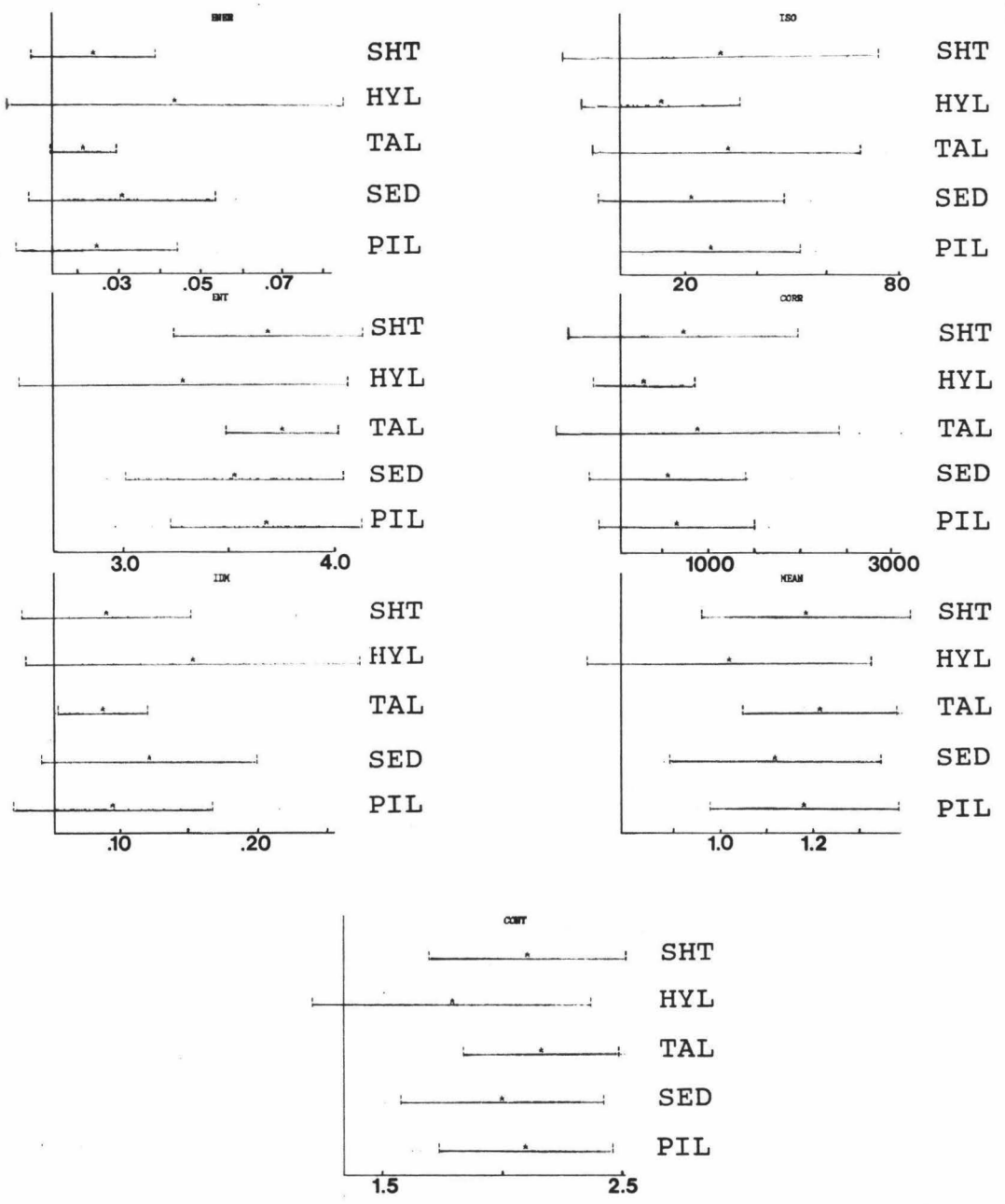

FIGURE 60. Plots of second-order texture statistics for a supervised classification of all 112 samples. PIL is pillow, SED is sediment, TAL is talus, HYL is hyaloclastite, and SHT is sheet flow. *'s show the mean for each class and |'s are standard deviation. Notice that no distinct groups separate out.

distinct groups are evident. Eliminating samples 73-112, representing a different look direction, produced the plots in Figure 61. Apparently, look direction doesn't matter, the results are the same: the means of the 5 classes determined by bottom photos are not statistically distinct.

Since the supervised classification failed to produce distinct groups, clustering was attempted to determine if the data would form natural groupings. Following is a recap of the results from several clustering attempts. Initially, all 112 samples were clustered using both initial centroid assignment methods and specifying 5-10 classes. Figure 62 shows results for 5 classes using the cyclic pattern method of initial centroid assignment. Note that for the most part, the standard deviations overlap one another. However, there is some separation. Class 5 stands out in contrast and mean. Class 1 stands out in mean, energy and entropy. Class 5 consists of 7 members and has a composition of 43% pillow, 29% talus, 14% sheet flow and 14% sediment. Class 1 has 16 members: 44% hyaloclastite, 44% sediment and 12% pillow. The remaining 3 classes have 27 members or more and are variable in composition.

Figure 63 shows the results from the same set of samples using the mean weighted method of initial cluster assignment. Cluster membership changes to a certain extent, but patterns are similar. Class 5 is a tighter cluster here, consisting of 2 talus samples. It is

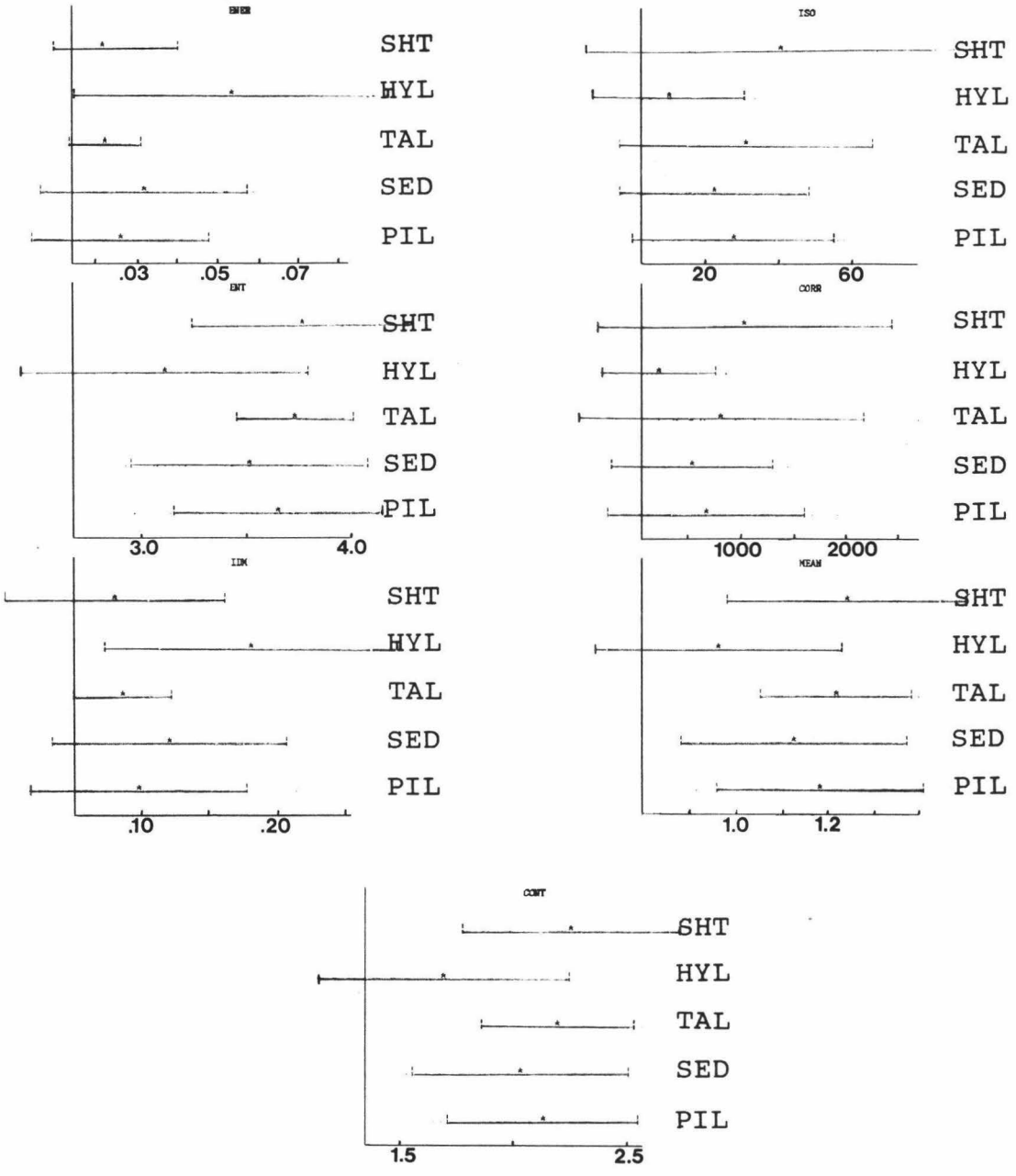

FIGURE 61. Plots of second-order texture statistics for a supervised classification of just the first 72 samples. Symbols and classes are the same as in Figure 60.

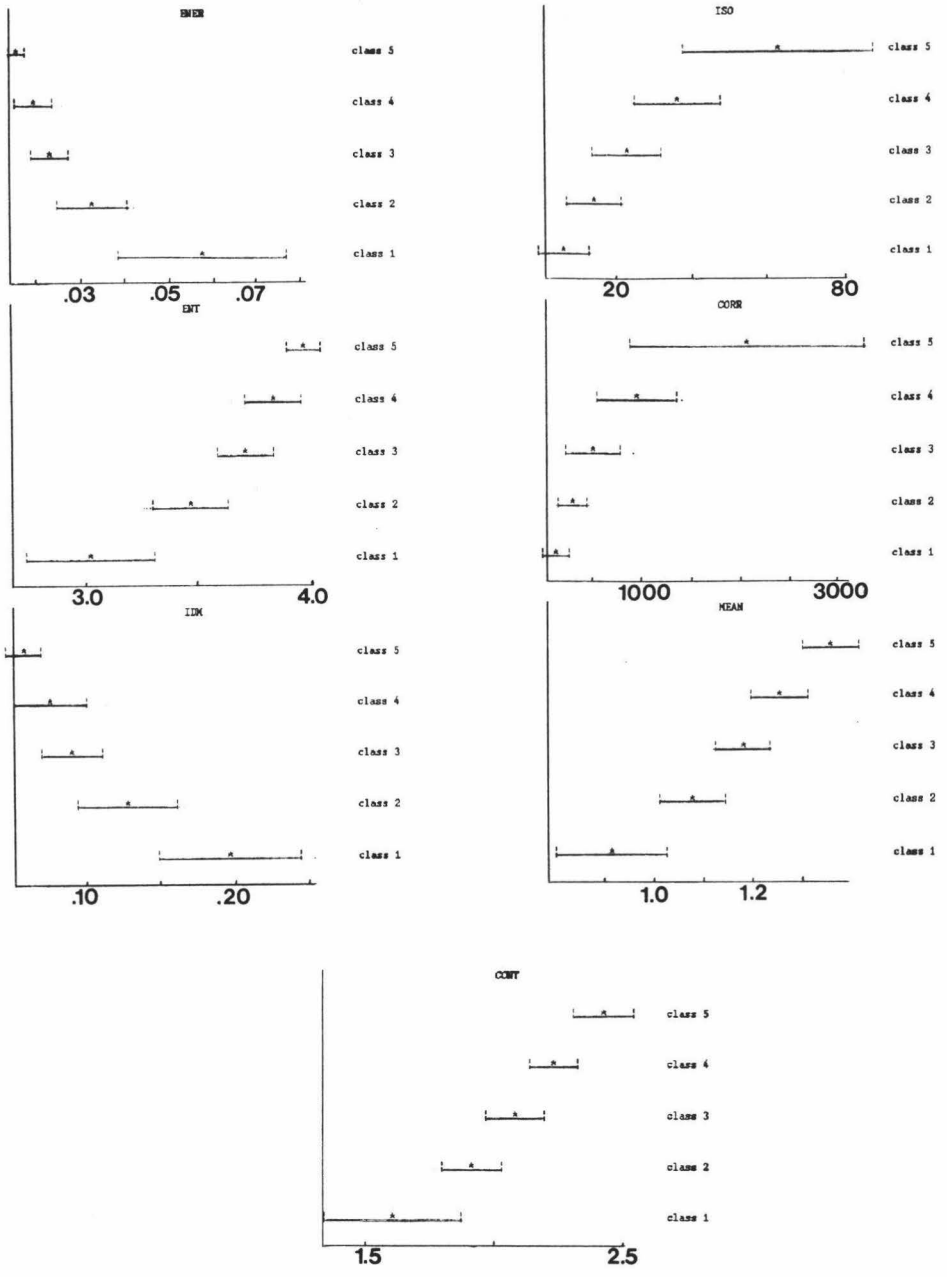

FIGURE 62. Plots of second-order texture statistics for clustering done with 112 samples, cyclic pattern method of initial centroid assignment and 5 classes specified. Symbols are the same as in Figure 60.

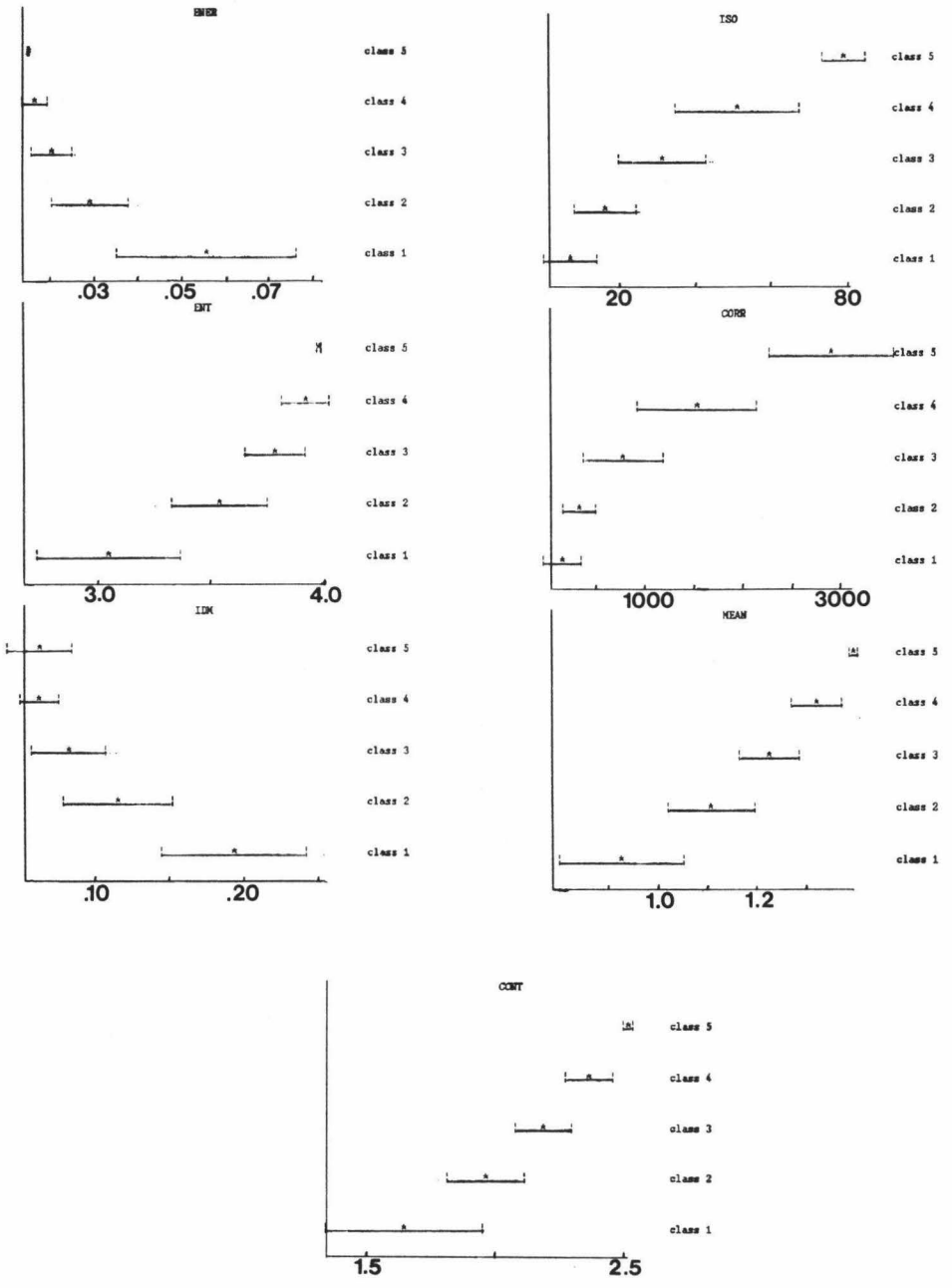

FIGURE 63. Plots of second-order texture statistics for clustering done with 112 samples, mean weighted method and 5 classes specified. Symbols are the same as in Figure 60.

distinct in contrast, isotropy, correlation and mean. Class 4, with 9 members (44% pillow, 33% sediment, 12% talus and 11% sheet flow), stands out in contrast and mean. Class 1 in this clustering is essentially the same as class 1 in the previous clustering: 44% sediment, 38% hyaloclastite, 18% pillow and has 18 members. This class stands out in mean, energy, entropy and IDM. The other 2 classes have 41 and 42 members and are essentially random in composition.

Though there are slight differences in the way these 2 methods of initial centroid assignment cluster, the trends we see are basically the same. Significantly pure groups of the 5 lithologies do not cluster naturally. Groups consist mainly of mixes of a) sediment and hyaloclastite and b) pillow and talus. Many sediment samples cluster in groups composed mainly of pillow plus talus. These particular samples are mimicking pillow/talus and are not being recognized as sediment, probably due to one or both of the reasons discussed earlier in the Methods section.

As more and more classes are added, cluster membership changes in specifics, but basic trends remain the same. Sediment and hyaloclastite continue to cluster together as does pillow and talus. Purity of classes does improve, because the large mixed classes are being split into smaller ones. Eventually, every cluster could be pure, but consisting only of a single member each, if 112 classes are specified. When the results from greater number of classes

are plotted, however, their separability does not significantly improve. As shown in Figure 64, clustered using 8 classes and the cyclic pattern method of initial centroid assignment, class 5 is the only one that stands reasonably well on its own. It is composed of equal parts pillow and talus (33% each) and equal parts sheet flow and sediment (17% each). Looking at the members of the other clusters, we have class 1 with 70% hyaloclastite, 20% sediment and 10% pillow, and class 7 with 66% sediment, 11% hyaloclastite and 13% pillow. The plots of classes 1 and 7 do not completely separate from each other, but viewed as one they are distinct in mean, energy, entropy and IDM.

Similarities are seen using the mean weighted method of initial centroid assignment with 8 classes specified (Figure 65). Classes 6 and 8 stand out in contrast, isotropy, correlation and mean. Class 6 is 50% pillow, 25% sheet flow and 25% sediment and has 4 members. Class 8 has 2 talus members. Class 1 is 50% hyaloclastite and 36% sediment (14 members); while class 7 has 15 members composed of 66% sediment and 20% hyaloclastite. Class 1 is distinguishable in every statistic, overlapping class 7 only in energy and IDM.

No pure clusters of more than 2 members emerge until 20 classes are specified using the cyclic pattern method of initial centroid assignment. Class 18 in Figure 66 is made up of 3 hyaloclastitie members. Class 4 is 68% hyaloclastite and 16% sediment. These classes, while not

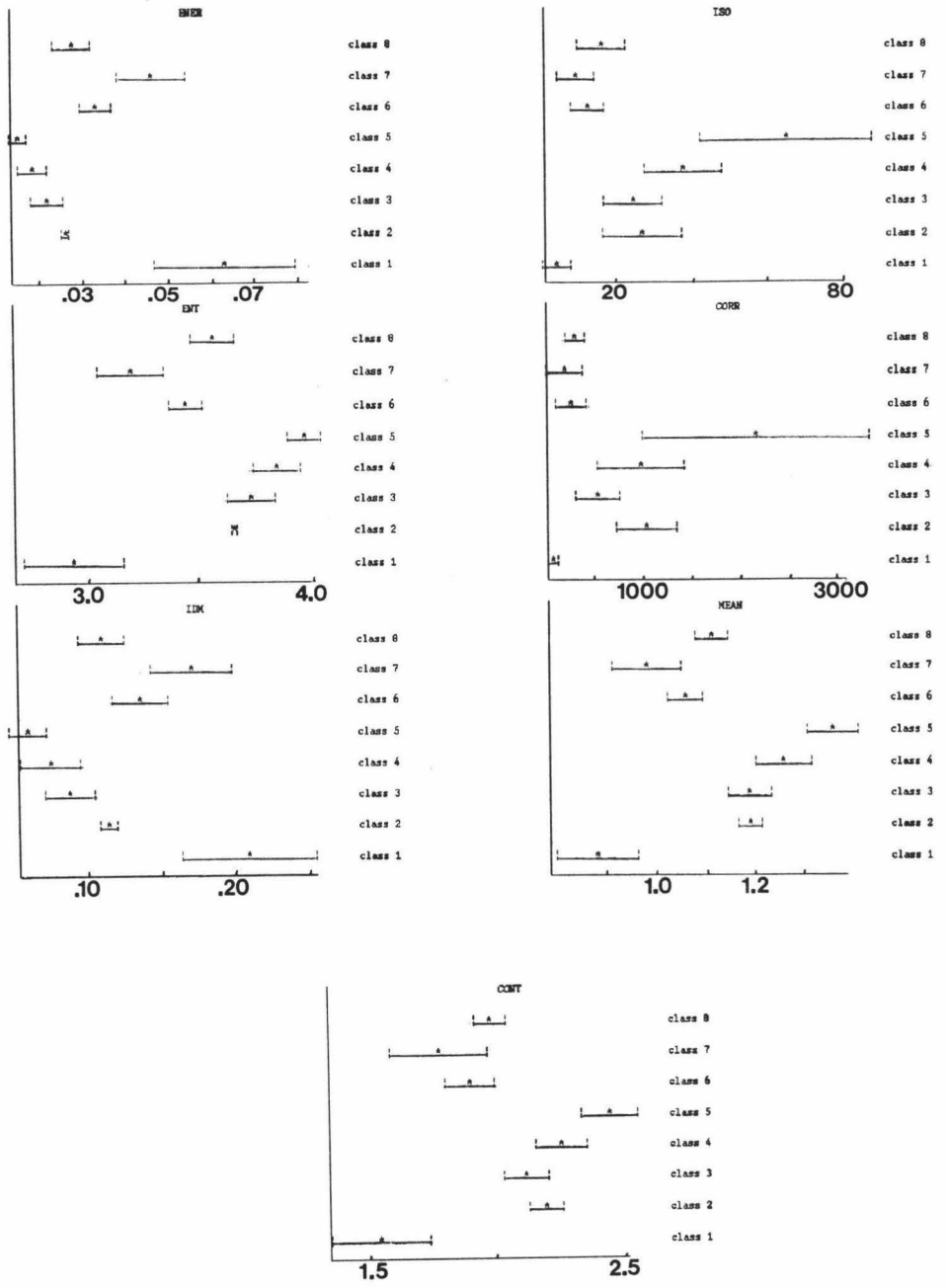

FIGURE 64. Plots of second-order texture statistics for clustering done with 112 samples, cyclic pattern method and 8 classes specified. Symbols are the same as in Figure 60.

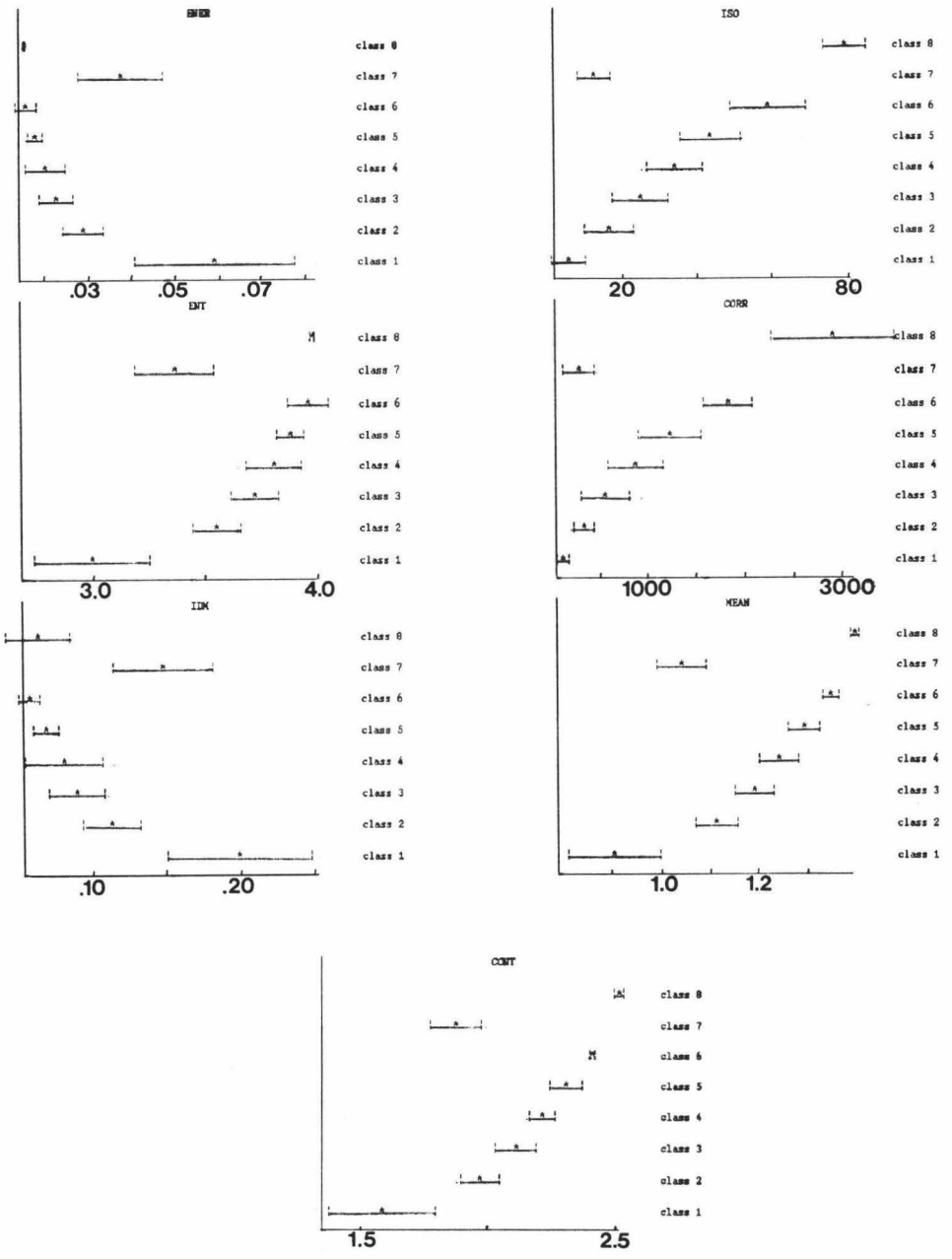

FIGURE 65. Plots of second-order texture statistics for clustering done with 112 samples, the mean weighted method of initial centroid assignment and 8 classes specified. Symbols are the same as in Figure 60.

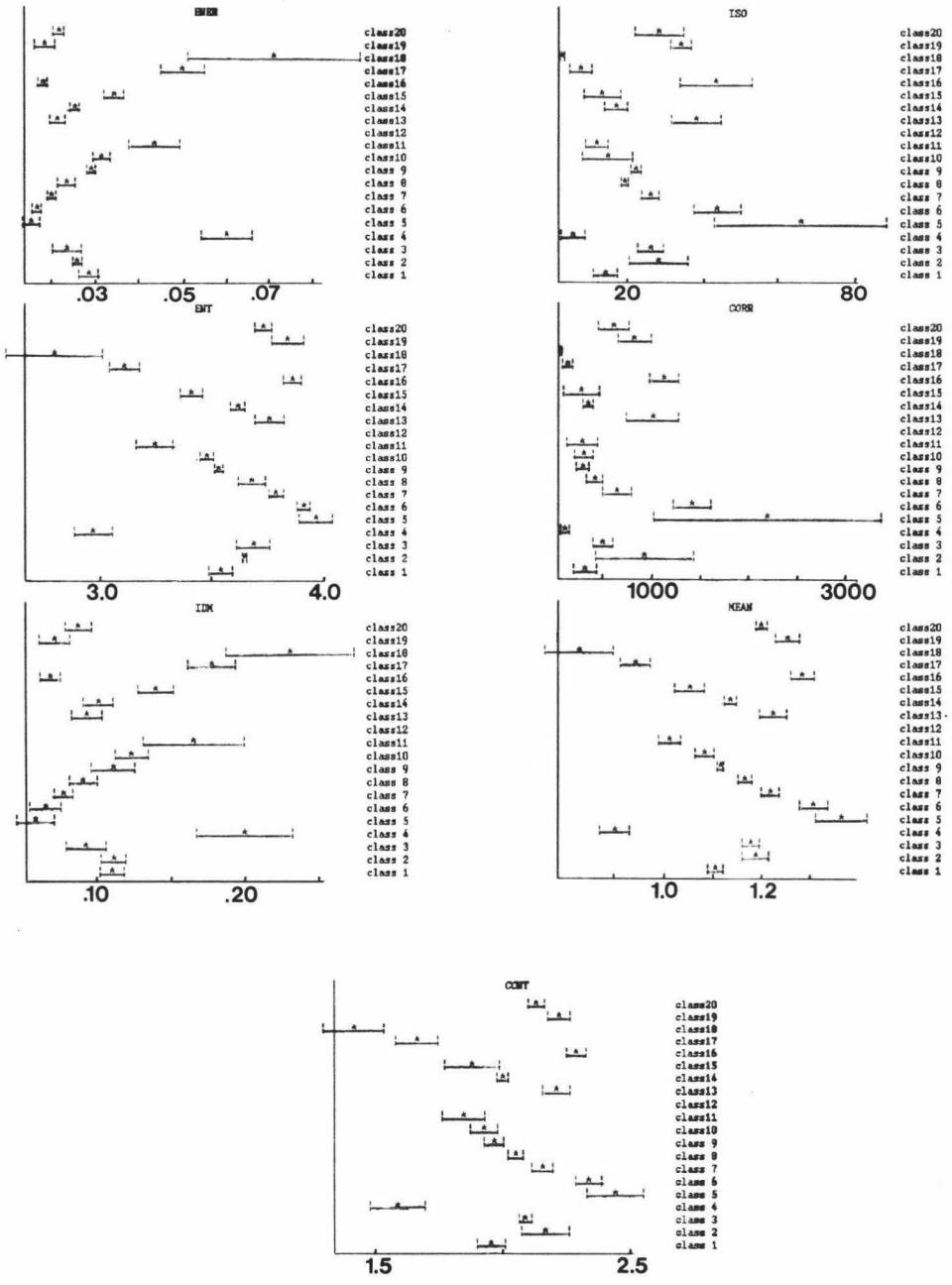

FIGURE 66. Plots of second-order texture statistics for clustering done with 112 samples, the cyclic pattern method and 20 classes specified. Symbols are the same as in Figure 60.

distinguishable individually (as class 18 in contrast and mean), are distinct collectively, except in IDM.

Attempting to ascertain if samples 73-112 (from the second look direction) were clouding the statistics, I eliminated them from the clustering routine. The remaining 72 samples were put through the same treatment as before. The only significant difference this produced was to make the clusters smaller. Clustering trends remain the same, creating sediment/hyaloclastite and pillow/talus groups. As an example, see Figure 67, representing the cyclic pattern method of initial centroid assignment with 5 classes specified. In Figure 67, class 2 is distinct in contrast, isotropy, correlation and mean. It is made up of 45% hyaloclastite, 36% sediment and the rest pillow. It is most closely related to class 1, consisting of 60% sediment, 20% hyaloclastite and 20% pillow. Classes 3, 4 and 5 are predominantly pillow/talus mixes.

Next, I went back to the 112 samples and eliminated all that were not composed of at least 80% of the intended geology in an attempt to ascertain if "cleaner" samples would improve the purity of the clusters. This completely removed the sheet flow samples. The remaining 97 samples (4 lithologies) were clustered into 5 classes, thus allowing for a "misfit" class. Assuming that the largest cluster with a potpourri of geology is the aforementioned misfit cluster, it would be class 4 with 36 members (Figure 68). Class 1 is equal amounts of pillow and talus with

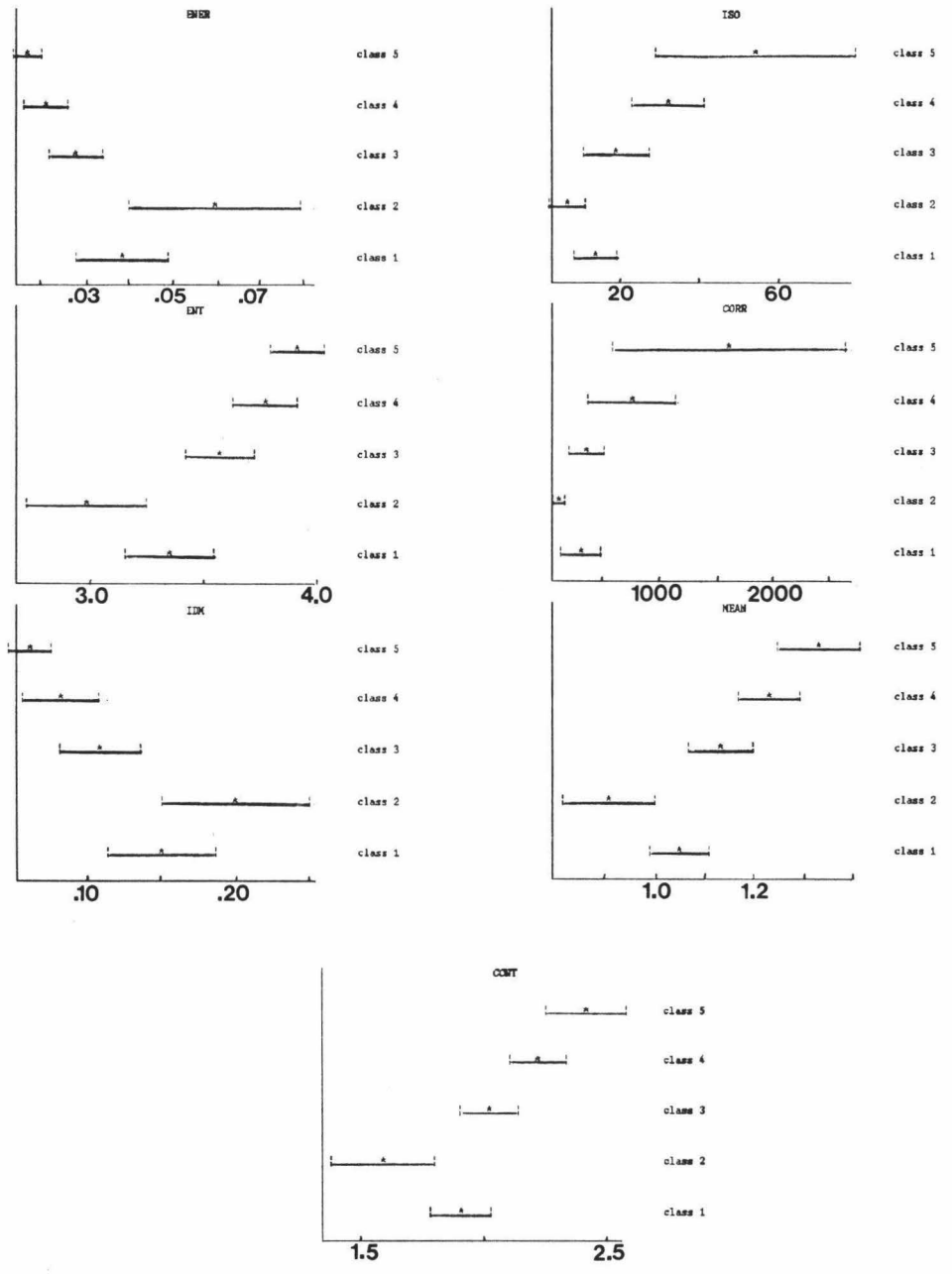

FIGURE 67. Plots of second-order texture statistics for clustering done with 72 samples, cyclic pattern method and 5 classes specified. Symbols are the same as in Figure 60.

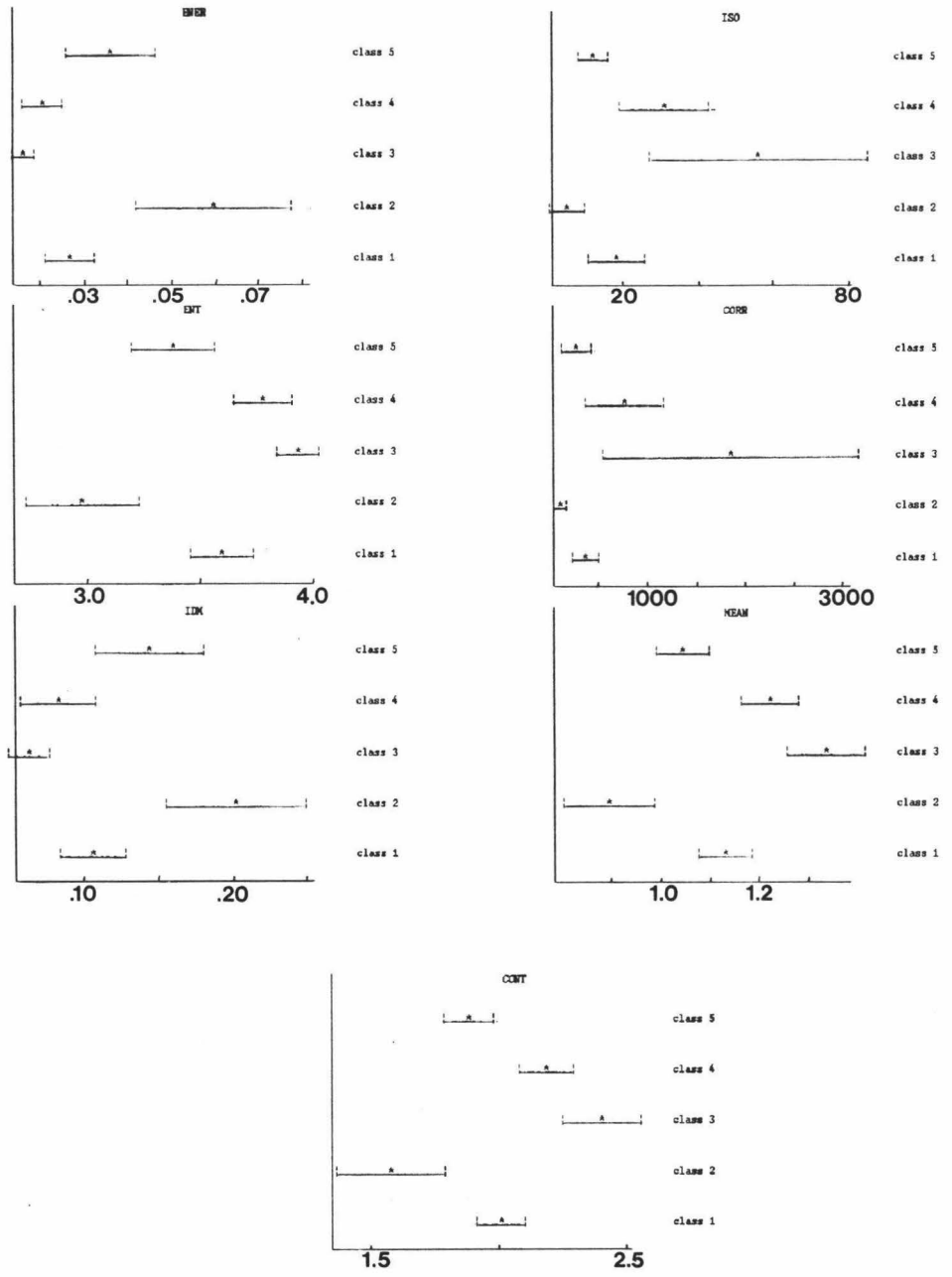

FIGURE 68. Plots of second-order texture statistics for clustering done with 97 samples representing 80% pure lithology, the cyclic pattern method and 5 classes specified. Symbols are the same as in Figure 60.

sediment. Class 2 is predominantly hyaloclastitie (54%) with 38% sediment. Class 3, like class 1, has an equal mix of pillow and talus again with sediment. Class 5 is mostly sediment (56%) with 22% hyaloclastite.

Class 2, mainly hyaloclastite, is the only one to stand out (Figure 68) in entropy, mean and contrast. It overlaps class 5, which is predominantly sediment, in the other statistics. Classes 1 and 3 have essentially the same composition, but are distinct from each other in the plots of their statistics.

The same pattern is seen until 9 classes are specified. At this point, a cluster of 86% sediment emerges having 7 members. Unfortunately, its plot is not distinct (class 7 in Figure 69). It overlaps most consistently with class 1 (70% hyaloclastite and 20% sediment).

At 15 classes, a cluster of 3 hyaloclastites (class 6 in Figure 70) and one of 4 sediments (class 10) are the first pure clusters to emerge. The hyaloclastite group (class 6) can be distinguished from the sediment class (10) in all statistics except correlation. Only the hyaloclastite group is distinct from all others, in contrast and mean.

This leads to the conclusion that hyaloclastite and sediment, as well as pillow and talus, are texturally similar. Eventually, with enough classes specified, some hyaloclastite and sediment samples do separate into different clusters, but are not necessarily distinguishable

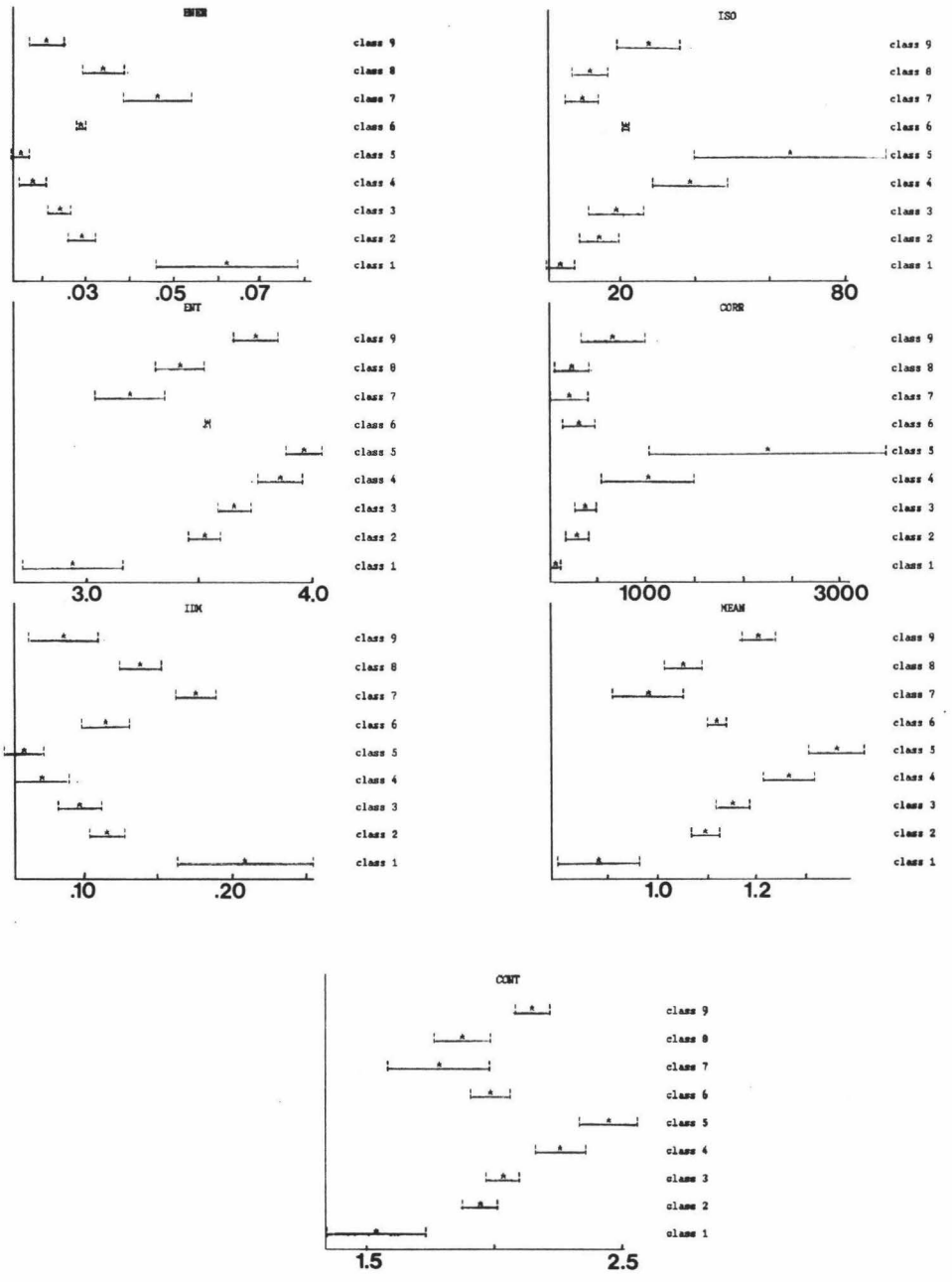

FIGURE 69. Plots of second-order texture statistics for clustering done with 97 samples representing 80% pure lithology, the cyclic pattern method and 9 classes specified. Symbols are the same as in Figure 60.

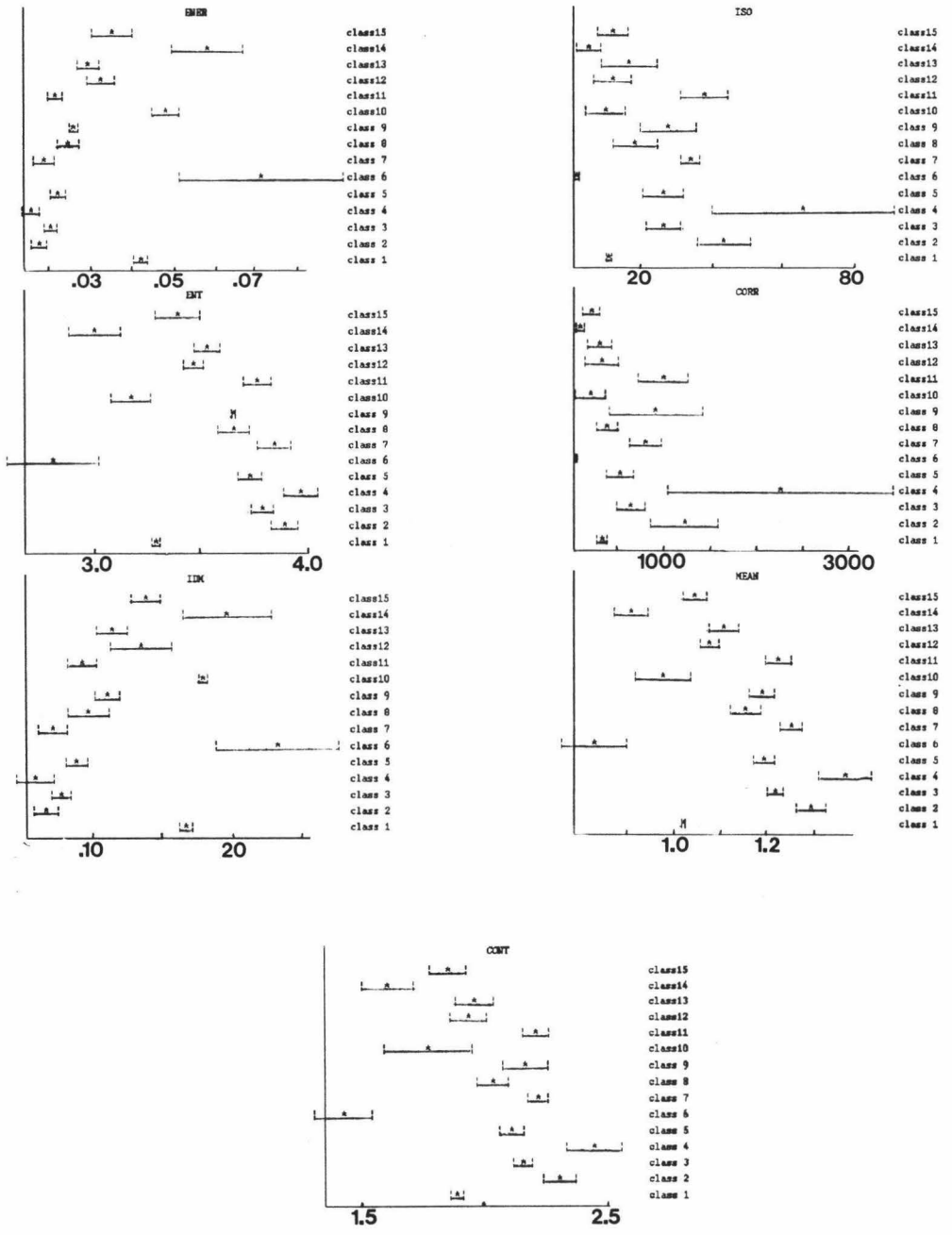

FIGURE 70. Plots of second-order texture statistics for clustering done with 97 samples representing 80% pure lithology, the cyclic pattern method and 15 classes specified. Symbols are the same as in Figure 60.

from each other. However, only hyaloclastite is distinct from all other groups, in some cases.

Not to lose sight of our original purpose, to assess the affect of lithology, roughness, slope angle and look angle on texture signature, I performed the following experiment. First, since the measure of roughness, in this study, is determined by a scale based on the lithology rather than a quantitative measurement, it can be discarded from this discussion. I grouped the 97 samples (80% pure) into the two look directions (Figure 71). These 2 groups were separated into 4 sub-groups of slope angles: $0\text{-}10^{o}$, $10\text{-}20^{o}$, $20\text{-}30^{o}$, $30\text{-}40^{o}$. Each of these 4 groups was further subdivided into look angle ranges: $0\text{-}10^{o}$, $10\text{-}20^{o}$, $20\text{-}30^{o}$, $30\text{-}40^{o}$, $40\text{-}50^{o}$, $50\text{-}60^{o}$, $60\text{-}70^{o}$. Lithologies in each of the look angle groups is rather arbitrary. However, slope angles of $0\text{-}20^{o}$ are predominantly sediment and hyaloclastite (71% combined), while angles of $20\text{-}40^{o}$ are mostly pillow and talus (70% combined).

This scheme produced 19 groups with at least 1 member apiece for the look direction on the bottom swath of the survey, and 18 groups for the look direction represented by the top swath. The means and standard deviation for each statistic are shown in Figure 72 and 73, respectively. No distinct separation is in evidence.

One further grouping scheme (Figure 74) has the 97 80% pure samples again divided first into the 2 look directions. These 2 groups were subdivided into the 4

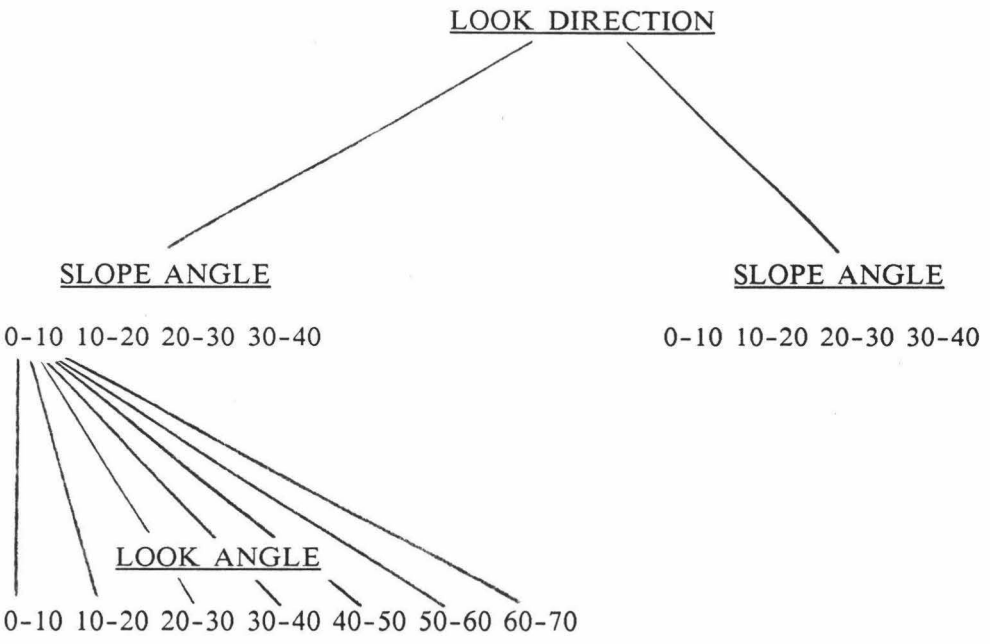

FIGURE 71. Diagram showing a grouping scheme employed to assess the effects of look direction, look angle, slope angle on the classification of the data. The samples were divided into the two look directions. These two groups were then divided into one of 4 slope angle ranges. Each of these groups was further subdivided into one of 7 look angle ranges.

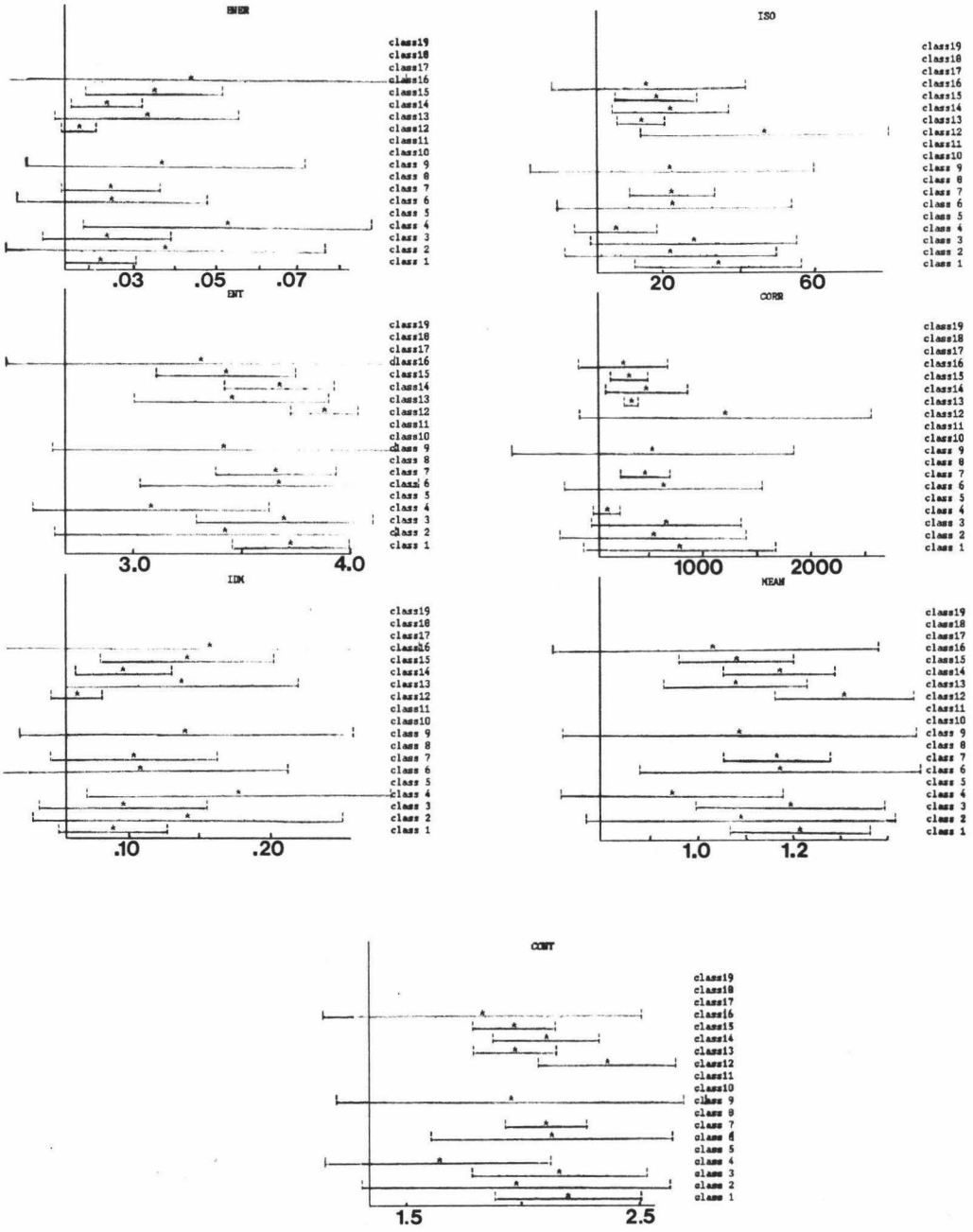

FIGURE 72. Plots of second-order texture statistics showing the results of the grouping scheme in Figure 71. These plots display data from the look direction represented by the southern swath of the SeaMARC II survey (Figure 57a). Symbols are the same as in Figure 60.

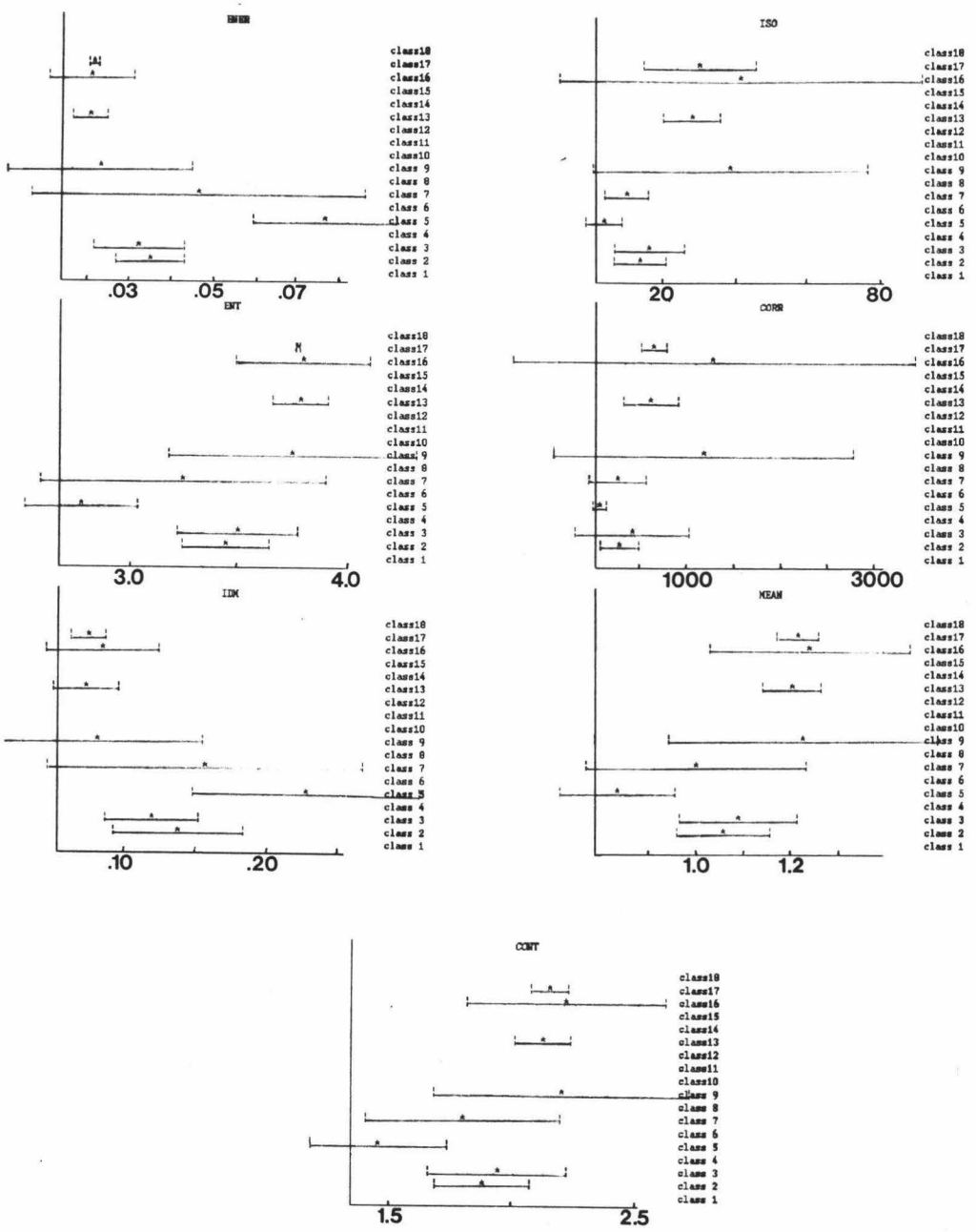

FIGURE 73. Plots of second-order texture statistics showing the results of the grouping scheme in Figure 71. These plots display data from the look direction represented by the northern swath of the SeaMARC II survey (Figures 57b and c). Symbols are the same as in Figure 60.

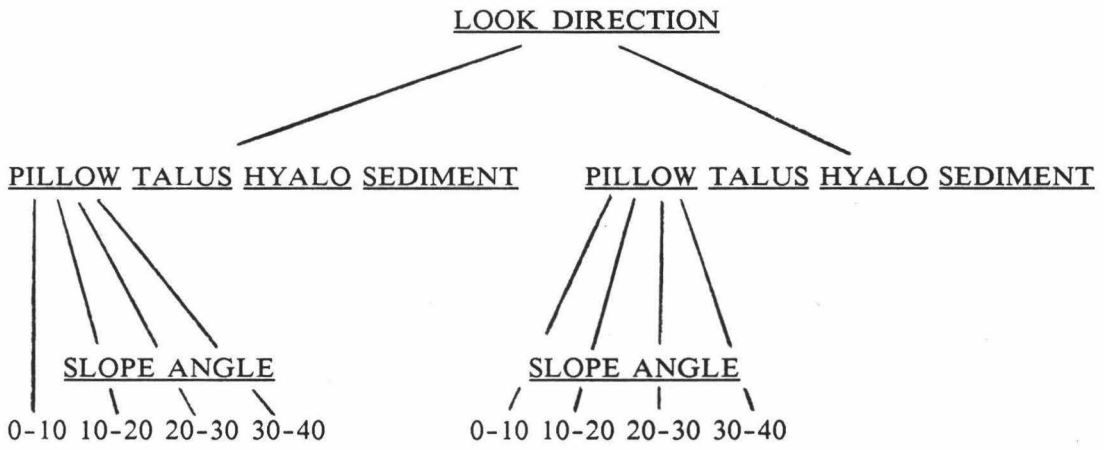

FIGURE 74. Diagram showing a second grouping scheme similar to that in Figure 71. This scheme divides the samples into the two look directions. These two groups are then divided into one of the 4 lithologic groups, then further subdivided into one of the 4 slope angle ranges.

lithologies: pillow, talus, hyaloclastite and sediment. These 4 groups are further subdivided into 4 slope angle ranges: 0-10°, 10-20°, 20-30°, 30-40°. Look direction 1 with 62 samples has 14 subsets (Figure 75), while look direction 2 with 35 samples has 12 (Figure 76). Again, no distinct groups emerge. Using this method of analysis, the conclusion is that look direction, look angle and slope angle have no recognizable affect on the second-order texture statistics.

A question arose at the conclusion of this study which challenged the value of our results. Particularly, do the texture statistics derived from the SeaMARC II sidescan image tell us anything different from what the eye can detect from the same image? The results of this study show that mixed groups of hyaloclastite/sediment and pillow/talus are distinguishable by SeaMARC II based on estimates of texture statistics. By simply looking at a SeaMARC II sidescan image, large patches of rock and sediment can be distinguished from each other. As explained in the SeaMARC II section, rough surfaces, such as those composed of rock, generally appear as dark areas on a SeaMARC sidescan image; while smooth surfaces, such as sediment, appear light.

In order to answer the question stated above, I examined each sample box on the SeaMARC II sidescan (Figure 57) from the set of 97 80% pure samples. I assembled the samples for each lithology which were located in large, homogeneous

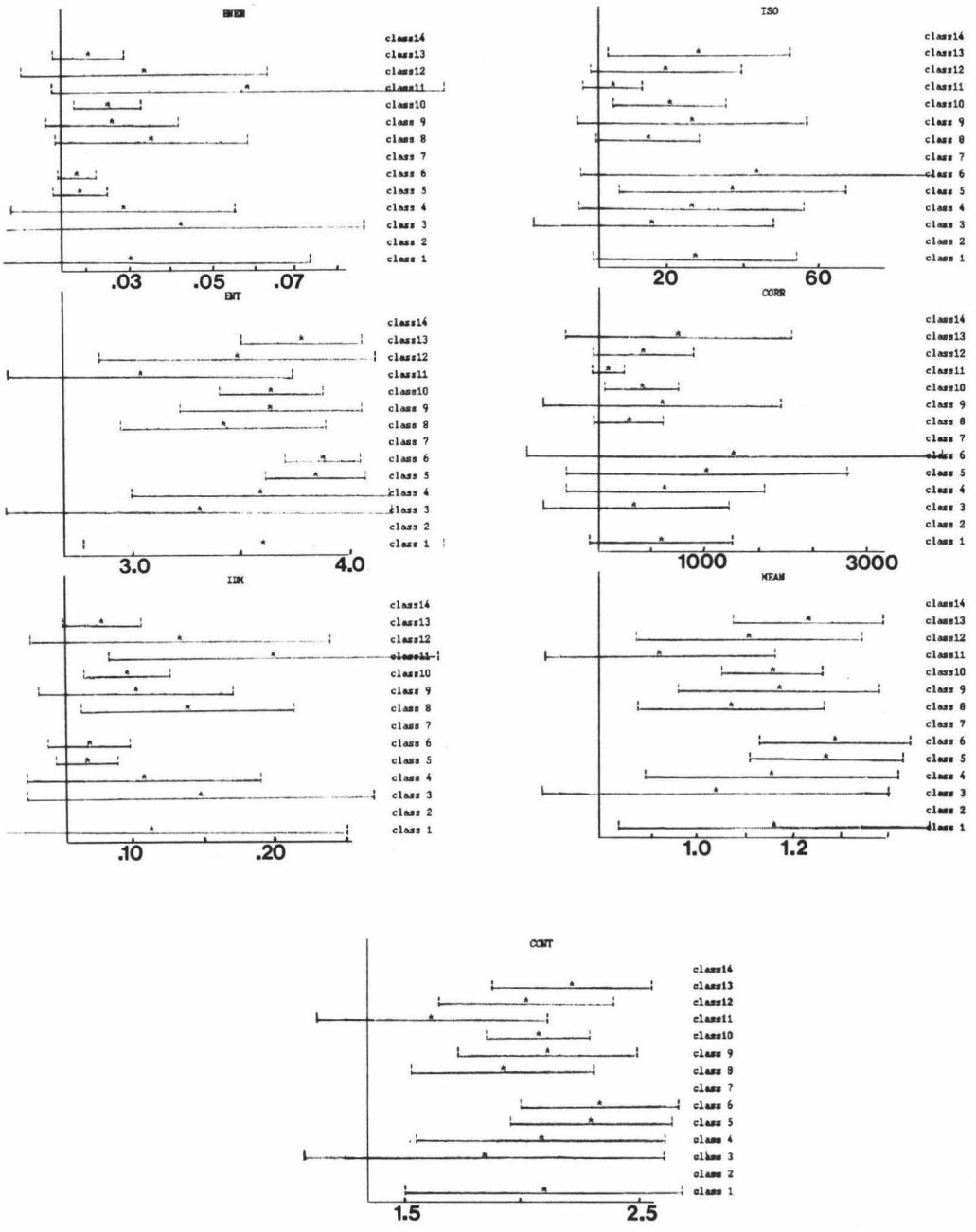

FIGURE 75. Plots of second-order texture statistics showing the results from the grouping scheme in Figure 74. These plots display data from the look direction represented by the southern swath of the SeaMARC II survey (Figure 57a). Symbols are the same as in Figure 60. Note some groups were empty, so no plot exists.

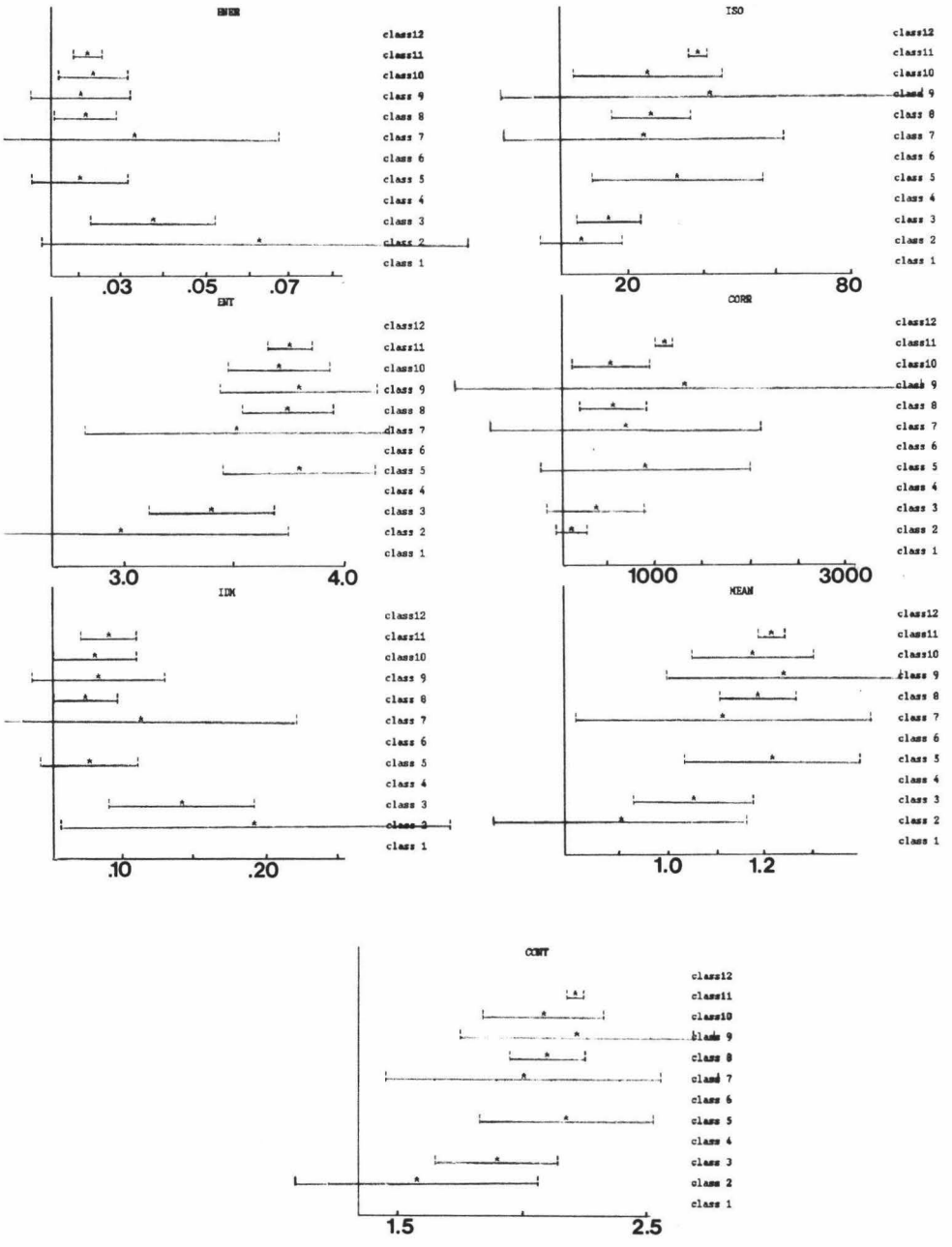

FIGURE 76. Plots of second-order texture statistics showing the results from the grouping scheme in Figure 74. These plots display data from the look direction represented by the top swath of the SeaMARC II survey (Figures 57b and c). Symbols are the same as in Figure 60.

patches, according to my observations. Since mean intensity is really what the eye detects in a homogeneous area, I plotted the mean and standard deviation of the mean intensities for the samples in each lithologic group (pillow, sediment, talus, hyaloclastite) (Figure 77). As shown in Figure 77, the means for each lithologic group are unique; however, the standard deviations for each group overlap a great deal. Therefore, mean intensity cannot, by itself, define distinct groups of lithology, whereas some second-order texture statistics can. It is interesting to note in Figure 77 the similarity in means and standard deviations for hyaloclastite/sediment and pillow/talus. These were the two mixed groups that could, largely, be separated by their texture statistics.

CONCLUSIONS

In conclusion, SeaMARC II can distinguish hyaloclastite/sediment from pillow/talus acoustically. Second-order statistics for each of these mixed groups are distinct regardless of look direction, look angle and slope angle. Hyaloclastite is the only lithology that is completely distinct from the other lithologies in this study.

Several possible explanations for the lack of any striking distinctions between classes exist. The first is

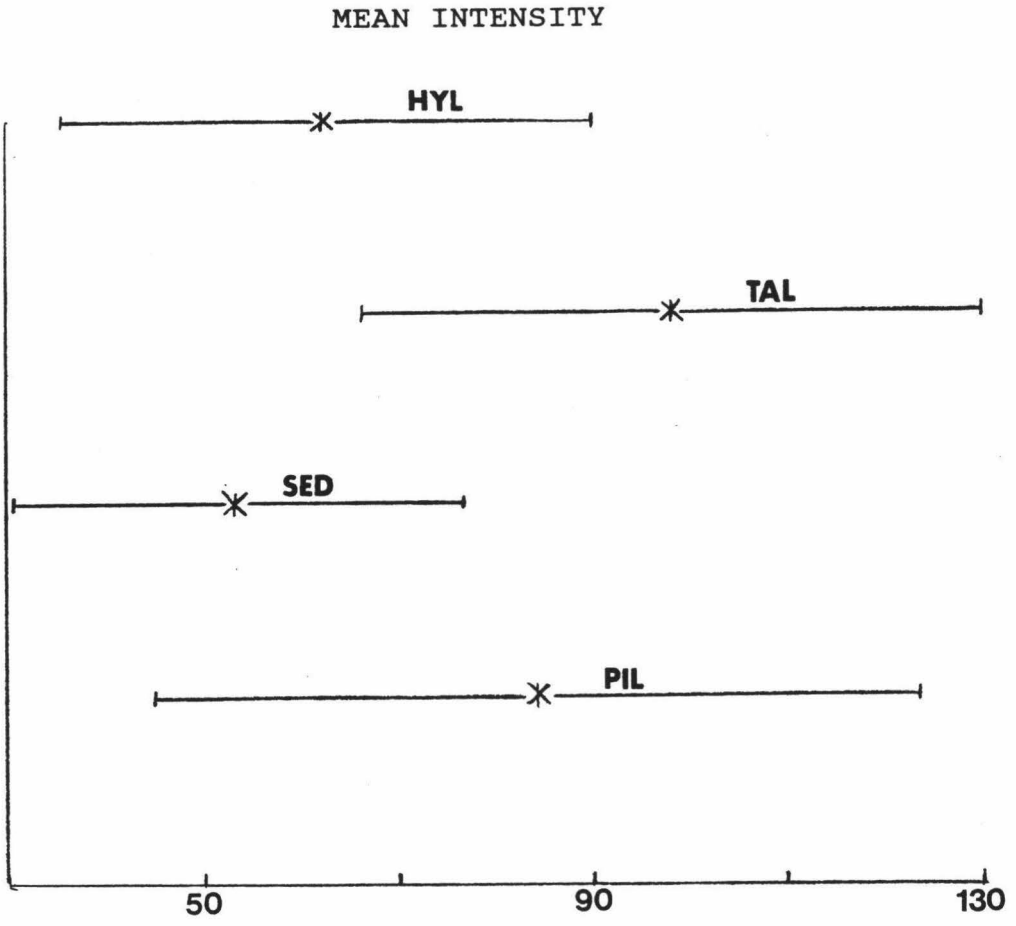

FIGURE 77. Plot of mean (*'s) and standard deviation (bars) of mean intensity for each lithologic group, using the set of 97 80% pure samples. HYL is hyaloclastite; TAL is talus; SED is sediment and PIL is pillow. Note that the means are unique, but standard deviations overlap a great deal. The first-order statistic of mean intensity does not help in distinguishing the lithologic groups.

that the feature vectors (the second-order statistics) utilized in this study are not sufficient to capture the information in the data. Secondly, we may have missed our intended geology and are not sampling what we think we are sampling. A third explanation is that the lithologies are not, in fact, acoustically distinct. The fact that hyaloclastite/sediment and pillow/talus classification combinations are common seems to indicate that this is the case, in as far as hyaloclastite and pillow lava are not acoustically distinct from sediment and talus, respectively; yet the combinations are distinct from each other. And finally, the ground truth leaves much to be desired, in that the bottom photographs provide such a limited view of what the geology is to either side of the dive track that they are not sufficient to estimate the homogeneity of a patch of seafloor.

APPENDIX A. Texture features

The texture feature vectors used in this study are extracted from a grey level difference co-occurrence matrix, as explained in the text (Texture Features), according to the following formulas. These equations are as taken from Reed and Hussong [1989] unless otherwise indicated.

CONTRAST

This feature measures image contrast. Image contrast is related to the range of grey levels in an image. The greater this range is, the greater the contrast [Schowengerdt, 1983]. It is calculated by

$$= \sum_{n=0}^{Ng-1} n^2 \left\{ \sum_{i=1}^{Ng} \sum_{\substack{j=1 \\ |i-j|=n}}^{Ng} S(i,j) \right\} / R$$

where Ng is the number of distinct grey levels in the image and R is the number of neighboring pixel pairs. An example of how contrast varies between two simple images can be seen in Figure 78.

INVERSE DIFFERENCE MOMENT (IDM)

This feature measures local homogeneity. In a homogeneous image (box 15, Figure 57a), there are few

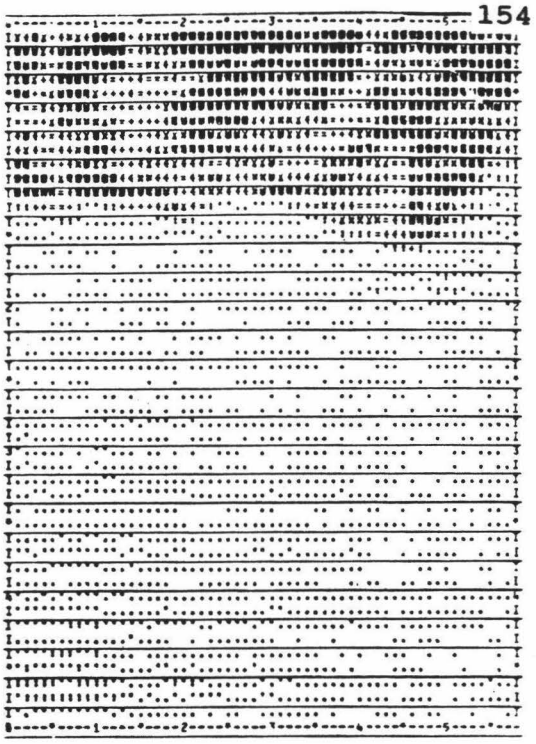

Grassland				Water Body		
Angle	ASM	Contrast	Correlation	ASM	Contrast	Correlation
0°	.0128	3.048	.8075	.1016	2.153	.7254
45°	.0080	4.011	.6366	.0771	3.057	.4768
90°	.0077	4.014	.5987	.0762	3.113	.4646
135°	.0064	4.709	.4610	.0741	3.129	.4650
Avg.	.0087	3.945	.6259	.0822	2.863	.5327

(a) (b)

FIGURE 78. Figure showing two different land-use category images and a comparison of some of their texture features: ASM (angular second moment) or the same as Energy, Contrast and Correlation [from Haralick et al., 1973]. a) An image of grassland, representing a heterogeneous image with a wide range of grey levels. b) An image of a body of water, representing a homogenous image.

dominant grey level transitions. As a result, the co-occurrence matrix for such an image will have small entries. Therefore, IDM values for homogeneous areas will be larger than in non-homogeneous areas. Compare IDM values in Table 1 for boxes 15 (0.2180) and 11 (0.0585), a heterogeneous area, in Figure 57a. The calculation is

$$= \sum_{i=1}^{Ng} \sum_{j=1}^{Ng} S(i,j) \; / \; ((1 + (i-j)^2) * R)$$

where Ng is the number of distinct grey levels in the image and R is the number of neighboring pixel pairs.

ENTROPY

Entropy is a measure of image structure and complexity. This value is largest when all the pixel pairs occur with equal frequency, as they would in a perfectly random image. The value decreases as image structure increases [Reed, 1987]. It is calculated by the expression

$$=- \sum_{i=1}^{Ng} \sum_{j=1}^{Ng} (S(i,j) \; / \; R) * \log (S(i,j) \; / \; R)$$

where Ng is the number of distinct grey levels and R is the number of neighboring pixel pairs.

ENERGY

This is a measure of image energy or coarseness. The coarser an image, or more heterogeneous it is, the smaller the energy value will be. In Figure 78b, there are not many dominant grey level transitions, so the co-occurrence matrix will have few large magnitude entries. In Figure 78a, the matrix will have a large number of small entries. Since the energy feature is a square of the sums of the entries, the energy value will be smaller for coarser images [Haralick et al., 1973]. Energy is

$$= \sum_{i=1}^{Ng} \sum_{j=1}^{Ng} (S(i,j) / R)^2$$

MEAN

This simply is the sum average of the entries in the grey level difference co-occurrence matrix. Values are higher for images with greater differences in grey levels. Mean is

$$= \sum_{i=0}^{Ng-1} i * (S(i,j) / R)$$

where Ng is the number of grey levels and R is the number of neighboring pixel pairs.

CORRELATION

A measure of linearity of an image and is highest in images with linear dependencies, as shown in Figure 78. The formula is

$$= \frac{\sum_{i=1}^{Ng} \sum_{j=1}^{Ng} (ij)\ S(i,j) / R - \mu_x\ \mu_y}{\sigma_x \quad \sigma_y}$$

where Ng is the number of distinct grey levels, R is the number of neighboring pixel pairs and μ_x, μ_y, σ_x, σ_y are the means and standard deviations for row and column sums, respectively.

ISOTROPY

This is a measure of the isotropy of the image; isotropy being directional uniformity of properties. This is calculated as the sum of the differences of the grey level difference co-occurrence matrices for angles of $\theta = 0^o$ and 90^o [Reed and Hussong, 1989] (Figure 55).

APPENDIX B. Keys to codes and scales

KEY TO VOLCANO CODE

The volcano code consists of 3 characters, only one of which is a non-zero number. The placement of the non-zero indicates the region of the Seamount 6 where the sample area is located.

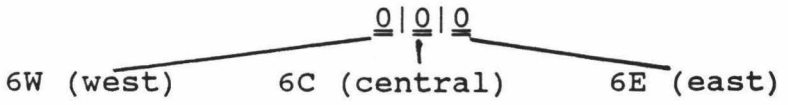

The non-zero numbers refer to where the sample area is located on the specified edifice:

0 not present
1 base
2 flank
3 near summit
4 summit

For example, box 1 (Figure 57a) is located on the flank of Seamount 6C, the central edifice. Therefore, its volcano code is 020. Similarly, box 5 has the volcano code 004 (Table 1), placing it on the summit of Seamount 6E, the easternmost edifice.

KEY TO THE GEOLOGY DESCRIPTORS

Each geology descriptor consists of 10 characters, or 5 pairs of characters. Each character pair refers to a particular lithology, as shown below.

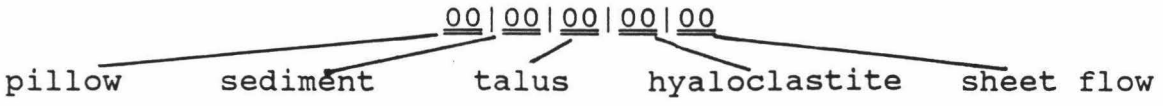

The first number of each character pair refers to the percentage of the specified lithology present: 0=not present, 1=1-10%, 2=11-20%, 3=21-30%, 4=31-40%, 5=41-50%, 6=51-60%, 7=61-70%, 8=71-80%, 9=81-90%, A=91-100%.

The second number of the pair provides a more detailed description of that particular lithology:

PILLOW	SEDIMENT
0 not present	0 not present
1 well sorted	1 rippled
2 moderately well-sorted	2 mounded, pocked/cratered
3 poorly sorted	3 bioturbated
4 encrusted	4 lag deposits/cobbles
5 slightly dusted	5 3 and 4
6 1 and 4	6 2 and 3
7 2 and 4	7 1 and 2
8 3 and 4	8 1 and 3
9 1 and 5	9 1 and 4

A 2 and 5

B 3 and 5

A 1 and 5

B 1 and 6

C 1, 2, 3, 4

D 2 and 4

E 2 and 5

F as coating/trace amount

TALUS

same descriptors as for pillows

HYALOCLASTITE

0 not present

1 slabby/crusty

2 nodular/hackly

3 1 with some nodes/rubbly

4 1 and 2 mix

SHEET FLOW

0 not present

1 slabby

2 nodular/hackly

3 ropey/hummocky

4 lobes

5 1 and 2

6 1 and 4

7 2 and 4

As an example, the code 8221000000 describes a sample location with 71-80% moderately well-sorted pillows and 11-20% rippled sediment. Similarly, the descriptor 00A9000000

refers to an area of 100% sediment which is rippled and has lag deposits and cobbles.

KEY TO ROUGHNESS SCALE

This scale is an attempt to quantify roughness. It is based not on quantifying the roughness of the terrane by, for example, digitizing photos, but rather on an estimate of relative roughness assuming a scale. It is based on the lithologies observed in the bottom photographs. Roughness decreases down-scale.

10 very rough, large-looking pillow/talus

9 mixed pillow, talus (not well-sorted), sediment (small percentage)

8 well-sorted talus

7 well-sorted pillows

6 egg-like pillow nodules

5 pahoehoe/sheet flow

4 hyaloclastite crust w/larger scale features

3 sediment w/ripples, mounded sediment, hyaloclastite crust

2 sediment w/lag deposits, worm holes

1 smooth sediment

APPENDIX C. Key to Table 1

Sample # corresponds to the numbered boxes on the SeaMARC II images in Figure 57.

Location (key'd to dive) is encoded in order to locate the sample area along the dive track. The first number (1 or 2) refers to an ALVIN dive or an ANGUS camera track, respectively. The second number (after the first decimal point) is the dive number. The third number (after the second decimal point) is a range, indicating the times along the dive tracks (to the best estimation) corresponding to the sample areas.

Nadir Long and Nadir Lat refer to the longitude and latitude of the sample areas, located along the nadir of the SeaMARC II swaths. These values are used to calculate actual longitude and latitude.

Distance From Nadir is the distance measured, perpendicular to the SeaMARC II ship track, from the nadir to the center of the sample area. (This was measured directly from the SeaMARC II images using a Gerber Scale.) This value is also used in the calculation of the actual longitude and latitude of the sample areas.

Ship Heading indicates the azimuth of the ship's course during the SeaMARC II survey. This value is used to calculate the actual longitude and latitude.

Longitude is calculated from the expression:

|((D*sin(C+90))/180300)| +A if the sample area is on the starboard side of the ship track, and

A- |((D*sin(C-90))/180300)| if on the port side.

Where A is nadir long, D is distance from nadir, C is ship heading and 180300 is a conversion factor for longitude (m/deg).

Latitude is calculated from the expression:

|((D*cos(C+90))/111120)| +B if on the starboard side, and

B- |((D*cos(C-90))/111120)| if on the port side.

Where the notation is the same as above and B is nadir lat, and 111120 is a conversion factor for latitude (m/deg).

Volcano is encoded in order to indicate precisely where on Seamount 6 each sample area is located. The encoding is explained in the Key to Volcano Code section of Appendix B.

Geology is an encoded description of lithologies present in the sample areas. The encoding is explained in the Key to Geology Descriptors section of Appendix B.

Box Size shows the size, in pixels, of each sample area. Efforts where taken to keep box size as equal as possible.

Mean I is the mean intensity statistic computed from the grey level difference matrices generated by the textural analysis computer program, ss_get.

MAD is the mean absolute deviation from the same matrix.

STD is the standard deviation.

VAR is the variance.

SKEW is the skewness.

KURT is the kurtosis.

Slope Angle is the best estimation of the range of bathymetric slope within each sample area, as taken from the slope map in Figure 58.

Look Angle is the angle, perpendicular to the ship track, from nadir out to the center of the sample area. It was calculated according to the expression: $\tan^{-1}$(distance from nadir/water depth).

Rough attempts to quantify the roughness of the sample area according to a scale which is explained in the Key to Roughness Scale section of Appendix B.

Water Depth for each sample area was determined from the SeaBeam bathymetric map.

Contrast, IDM (Inverse Difference Moment), Entropy, Energy, Mean, Corr (Correlation), and Isotropy are the seven textural variables generated by the ss_get program using the grey level differences. These are explained in Appendix A.

Same as Box indicates which sample areas have a corresponding pair which was viewed at a different look direction.

REFERENCES

Batiza, R. [1977] Age, volume, compositional and spatial relations of small isolated oceanic central volcanoes. Marine Geology 24: 169-183.

Batiza, R. [1982] Abundances, distribution and sizes of volcanoes in the Pacific Ocean and implications for the origin of non-hotspot volcanoes. Earth and Planetary Science Letters 60: 195-206.

Batiza, R. [1989] Seamounts and seamount chains of the eastern Pacific. In Winterer, E.L., D.M. Hussong and R.W. Decker, eds., The Eastern Pacific Ocean and Hawaii: Boulder, Colorado, Geological Society of America, The Geology of North America, v. N: 289-306.

Batiza, R. and D. Vanko [1983] Volcanic development of small oceanic central volcanoes on the flanks of the East Pacific Rise inferred from narrow-beam echo-sounder surveys. Marine Geology 54: 53-90.

Batiza, R. and D. Vanko [1984] Petrology of young Pacific seamounts. Journal of Geophysical Research 89: 11235-11260.

Batiza, R. and D. Vanko [1985] Petrologic evolution of large failed rifts in the eastern Pacific; Petrology of volcanic and plutonic rocks from the Mathematician Ridge area and the Guadalupe trough. Journal of Petrology 26: 564-602.

Batiza, R., D.J. Fornari, D.A. Vanko and P. Lonsdale [1984] Craters, calderas, and hyaloclastites on young Pacific seamounts. Journal of Geophysical Research 89: 8371-8390.

Batiza, R., P.J. Fox, P.R. Vogt, S.C. Cande, N.R. Grindlay, W.G. Melson and T. O'Hearn [1989a] Morphology, abundance, and chemistry of near-ridge seamounts in the vicinity of the Mid-Atlantic Ridge ~26°S. Journal of Geology 97: 209-220.

Batiza, R., T.L. Smith and Y. Niu [1989b] Geological and petrologic evolution of seamounts near the EPR based on submersible and camera study. Marine Geophysical Researches 11: 169-236.

Bergersen, D.D. [1991] A synopsis of SeaMARC II side-scan processing techniques. Submitted to Oceans '91.

Blackinton, J.G., D.M. Hussong and J. Kosalos [1983] First results from a combination side scan sonar and seafloor mapping system (SeaMARC II). Offshore Technology Conference 4478, v. 1: 307-311.

Bonatti, E. and H. Tazieff [1970] Exposed guyots from the Afar Rift, Ethiopia. Science 168: 1087-1089.

Bryan, W.B. and J.G. Moore [1977] Compositional variations of young basalts in the Mid-Atlantic Ridge rift valley near latitude 36°49'N. Geological Society of America Bulletin 88: 556-570.

Christensen, M.N. and C.M. Gilbert [1964] Basaltic cone suggests constructional origin of some guyots. Science 143: 240-242.

Clague, D.A. and R.D. Jarrard [1973] Tertiary Pacific plate motion deduced from the Hawaiian-Emperor chain. Geological Society of America Bulletin 84: 1135-1154.

Crough, S.T. [1978] Thermal origin of mid-plate hot-spot swells. Geophysical Journal of the Royal Astronomical Society 55: 451-469.

Crough, S.T. [1983] Hotspot swells. Annual Review of Earth and Planetary Sciences 11: 165-193.

Davies, T.A. and A.S. Laughton [1972] Sedimentary processes in the North Atlantic. In Laughton, A.S., W.A. Berggren and others, eds., Initial Reports of the Deep Sea Drilling Project 12: Washington, D.C., U.S. Government Printing Office: 905-934.

Davies, T.A. and T.R. Worsley [1981] Paleoenvironmental implications of oceanic carbonate sedimentation rates. In Douglas, R. and E. Winterer, eds., SEPM Special Publication 32: 169-179.

Davis, J.C. [1986] Statistics and Data Analysis in Geology. Wiley and Sons, New York: 646 pp.

Detrick, R.S. and S.T. Crough [1978] Island subsidence, hot spots, and lithospheric thinning. Journal of Geophysical Research 83: 1236-1244.

Emery, K.O., J.J. Tracey, Jr. and H.S. Ladd [1954] Geology of Bikini and nearby atolls. U.S. Geologic Survey Professional Paper 260-A: 1-262.

Epp, D. and N.C. Smoot [1989] Distribution of seamounts in the North Atlantic. Nature 337: 254-257.

Fisher, R.V. and H.-U. Schmincke [1984] Pyroclastic Rocks. Springer-Verlag, New York: 472pp.

Fiske, R.S. and E.D. Jackson [1972] Orientation and growth of Hawaiian volcanic rifts: the effect of regional structure and gravitational stress. Proceedings of the Royal Society of London, series A 329: 299-326.

Fornari, D.J., R. Batiza and J.F. Allan [1987] Irregularly shaped seamounts near the East Pacific Rise: implication for seamount origin and Rise axis processes. In Keating, B.H., P. Fryer, R. Batiza and G.W. Boehlert, eds., Seamounts, Islands and Atolls, AGU Geophysical Monograph 43: 35-47.

Fornari, D.J., M.R. Perfit, J.F. Allan and R. Batiza [1988] Small-scale heterogeneities in depleted mantle sources: near-ridge seamount lava geochemistry and implications for mid-ocean-ridge magmatic processes. Nature 331: 511-513.

Fornari, D.J., W.B.F. Ryan and P.J. Fox [1984] The evolution of craters and calderas on young seamounts: insights from SeaMARC I and SeaBeam sonar surveys of a small seamount group near the axis of the East Pacific Rise at ~ 10°N. Journal of Geophysical Research 89, B13: 11,069-11,083.

Fryer, P. and G.J. Fryer [1987] Origins of nonvolcanic seamounts in a forearc environment. In Keating, B.H., P. Fryer, R. Batiza and G.W. Boehlert, eds., Seamounts, Islands and Atolls, AGU Geophysical Monograph 43: 35-47.

Gagalowicz, A. [1980] Visual discrimination of stochastic texture fields based upon second order statistics. In Proc. 5th Int. Joint Conf. Pattern Recognition, Miami Beach, Florida: 786-789.

Gardner, J.V., M.E. Field, H. Lee, B.E. Edwards, D.G. Masson, N. Kenyon and R.B. Kidd [1991] Ground-truthing 6.5-kHz side scan sonographs; what are we really imaging? Journal of Geophysical Research 96: 5955-5974.

Genin, A., P.K. Dayton, P.F. Lonsdale and F.N. Spiess [1986] Corals on seamount peaks provide evidence of current acceleration over deep-sea topography. Nature 322:59-61.

Grigg, R.W. [1982] Darwin point: a threshold for atoll formation. Coral Reefs 1:29-34.

Grigg, R.W. and D. Epp [1989] Critical depth for the survival of coral islands: effects on the Hawaiian Archipelago. Science 243: 638-641.

Haralick, R.M., K. Shanmugam and I. Dinstein [1973] Textural features for image classification. IEEE Trans, Systems, Man, and Cybernetics, SMC-3, Nov.: 610-621.

Hartigan, J.A. [1975] Clustering Algorithms. Wiley-Interscience, New York: 351 pp.

Hekinian, R., M. Fevrier, F. Avedik, P. Cambon, J.L. Charlou, H.D. Needham, J. Raillard, J. Boulegue, L. Merlivat, A. Moinet, S. Manganini and J. Lange [1983] East Pacific Rise near 13°N; Geology of new hydrothermal fields. Science 219: 1321-1324.

Hutchison, I. [1985] The effects of sedimentation and compaction on oceanic heat flow. Geophysical Journal of the Royal Astronomical Society 82: 439-459.

Jackson, D.R., D.P. Winebrenner and A. Ishimaru [1986] Application of the composite-roughness model to high-frequency bottom backscattering. Jour. Acoust. Soc. Am. 79: 1410-1422.

Johnson, H.P. and M. Helferty [1990] The geological interpretation of side-scan sonar. Reviews of Geophys. 28: 357-380.

Julesz, B. [1962] Visual pattern discrimination. IRE Trans. Inform. Theory IT-8: 84-92.

Julesz, B. et al. [1973] Inability of humans to discriminate between visual textures that agree in second order statistics-Revisited. Perception 2: 391-405.

Kear, D. [1964] Volcanic alignments north and west of New Zealand's central volcanic region. New Zealand Journal of Geology and Geophysics 7: 24-44.

Kennett, J.P. [1982] Marine geology. Prentice Hall, New Jersey: 813pp.

Kent, P.E. [1966] The transport mechanism in catastrophic rock falls. Journal of Geology 74: 79-83.

Ladd, H.S. and S.O. Schlanger [1960] Drilling operations on Eniwetok Atoll. U.S. Geological Survey Professional Paper 260-Y: 863-905.

Laws, K.I. [1980] Textured image segmentation. Ph.D. dissertation, Dept. of Eng., Univ. of South. Calif., Los Angeles: 176 pp.

Levin, L.A. and C.A. Nittrouer [1987] Textural characteristics of sediments on deep seamounts in the Eastern Pacific Ocean between 10°N and 30°N. In Keating, B.H., P. Fryer, R. Batiza and G.W. Boehlert, eds., Seamounts, Islands and Atolls, AGU Geophysical Monograph 43: 187-203.

Lonsdale, P. [1972] Sedimentation and erosion on Horizon Guyot. Geological Society of America Bulletin 83: 289-316.

Lonsdale, P. [1977] Abyssal pahoehoe with lava coils at the Galapagos Rift. Geology 5: 147-152.

Lonsdale, P. [1978] A pair of young cratered volcanoes on the East Pacific Rise. Journal of Geology 87:157-173.

Lonsdale, P. [1983] Laccoliths (?) and small volcanoes on the flank of the EPR. Geology 11: 706-709.

Lonsdale, P. [1985] Nontransform offsets of the Pacific-Cocos plate boundary and their traces on the rise flank. Geological Society of America Bulletin 96: 313-327.

Lonsdale, P. and R. Batiza [1980] Submersible study of hyaloclastite and lava flows on young seamounts at the mouth of the Gulf of California. Geological Society of America Bulletin 91: 545-554.

Lonsdale, P. and F.N. Spiess [1979] A pair of young cratered volcanoes on the East Pacific Rise. Journal of Geology 87: 157-173.

Lonsdale, P., W.R. Normark and W.A. Newman [1972] Sedimentation and erosion on Horizon Guyot. Geological Society of America Bulletin 83: 289-316.

Malahoff, A. [1987] Geology of the summit of Loihi submarine volcano. U.S.G.S. Prof. Paper 1350, v.1: 133-144.

Malahoff, A., G.M. McMurtry, J.C. Wiltshire and H.-W. Yeh [1982] Geology and chemistry of hydrothermal deposits from active submarine volcano Loihi, Hawaii. Nature 298: 234-239.

Mayer, L.A. [1979] The origin of fine-scale acoustic stratigraphy in deep-sea carbonates. Journal of Geophysical Research 84: 6177-6184.

McBirney, A.R. [1963] Factors governing the nature of submarine volcanism. Bulletin of Volcanology 26: 455-469.

McKenzie, D.P., A.B. Watts, B.E. Parsons and M. Roufosse [1980] Planform of mantle convection beneath the Pacific Ocean. Nature 288: 442-446.

McNutt, M.K. [1984] Lithospheric flexure and thermal anomalies. Journal of Geophysical Research 89: 11,180-11,194.

McNutt, M. [1987] Temperature beneath midplate swells: the inverse problem. In Keating, B.H., P. Fryer, R. Batiza and G.W. Boehlert, eds., Seamounts, Islands and Atolls, AGU Geophysical Monograph 43: 123-132.

McNutt, M. and H.W. Menard [1978] Lithospheric flexure and uplifted atolls. Journal of Geophysical Research 83: 1206-1212.

Menard, H.W. [1956] Archipelagic aprons. American Association of Petroleum Geologists Bulletin 40: 2195-2210.

Menard, H.W. [1964] Marine geology of the Pacific. New York, McGraw-Hill Book Co., Inc.: 271p.

Menard, H.W. [1969] Growth of drifting volcanoes. Journal of Geophysical Research 74: 4827-4837.

Menard, H.W. [1983] Insular erosion, isostasy, and subsidence. Science 220: 913-918.

Menard, H.W. [1984] Origin of guyots: the Beagle to Seabeam. Journal of Geophysical Research 89: 11,117-11,123.

Moore, J.G., D.A. Clague, R.T. Holcomb, P.W. Lipman, W.R. Normark and M.E. Torresan [1989] Prodigious submarine landslides on the Hawaiian Ridge. Journal of Geophysical Research 94: 17,465-17,484.

Nakamura, K. [1977] Volcanoes as possible indicators of tectonic stress orientation-principle and proposal. Journal of Volcanology and Geothermal Research 2: 1-16.

Parsons, B. and S. Daly [1983] The relationship between surface topography, gravity anomalies, and the temperature structure of convection. Journal of Geophysical Research 83: 1129-1144.

Parsons, B. and D. McKenzie [1978] Mantle convection and the thermal structure of the plates. Journal of Geophysical Research 83: 4485-4496.

Phillips, J.D. and H.S. Fleming [1978] Multi-beam sonar study of the Mid-Atlantic Ridge rift valley, 36^{o}-37^{o}N. Geological Society of America, Map Chart Series MC-19: 24p.

Pratt, W.K. [1978] Digital Image Processing. John Wiley, New York: 614 pp.

Reed, T.B.R. [1987] Digital image-processing and analysis techniques for SeaMARC II side-scan sonar imagery. Ph. D. Dissertation, Univ. of Hawaii at Manoa, Honolulu.

Reed, T.B.R. and D. Hussong [1989] Digital image processing techniques for enhancement and classification of SeaMARC II side scan sonar imagery. Jour. Geophys. Res. 94: 7469-7490.

Renard, V. and J.P. Allenou [1979] SEA BEAM multi-beam echo sounding in "Jean Charcot". Description, evaluation and first results. Int. Hydrog. Rev. 56: 35-67.

Robinson, E.M. and B. Parsons [1988] The effect of a shallow low-viscosity zone on the formation of midplate swells. Journal of Geophysical Research 93: 3144-3156.

Rona, P.A. [1973] Relations between rates of sediment accumulation on continental shelves, sea-floor spreading, and eustacy inferred from the Central North Atlantic. Geological Society of America Bulletin 84: 2851-2872.

Rotondo, G. [1980] A reconstruction of linear island chain positions in the Pacific: a case study using the Hawaiian-Emperor chain. M.S. thesis, University of Hawaii, Honolulu, 58p.

Ryan, M.P., R.Y. Koyanagi and R.S. Fiske [1981] Modeling the three-dimensional structure of magma transport systems: application to Kilauea volcano, Hawaii. Journal of Geophysical Research 86: 7111-7129.

Schowengerdt, R.A. [1983] Techniques for Image Processing and Classification in Remote Sensing. Academic Press, New York: 249 pp.

Sclater, J.G., R.N. Anderson and M.L. Bell [1971] The elevation of ridges and evolution of the central eastern Pacific. Journal of Geophysical Research 76: 7888-7915.

Shor, A. [1990] SeaMARC II seafloor mapping system: seven years of Pacific research. Pacific Rim Congress, Australian Inst. of Mining and Metallurgy 3: 49-59.

Simkin, T. [1972] Origin of some flat-topped volcanoes and guyots. In Shagam, R., R.B. Hargraves and others, eds., Studies in earth and space sciences, Geological Society of America Memoir 132: 183-193.

Simkin, T. and R. Batiza [1984] Flattish summits, calderas and circumferential vents: a morphogenetic comparison of young EPR seamounts and Galapagos volcanoes. Eos Transactions, American Geophysical Union 65:1080.

Smith, D.K. [1988] Shape analysis of Pacific seamounts. Earth and Planetary Science Letters 90: 457-466.

Smith, T.L. and R. Batiza [1989] New field and laboratory evidence for the origin of hyaloclastite flows on seamount summits. Bulletin of Volcanology 51: 96-114.

Stanley, D.J. and P.T. Taylor [1977] Sediment transport down a seamount flank by a combined current and gravity process. Marine Geology 23: 77-88.

Stanton, T.K. [1984] Sonar estimates of seafloor microroughness. Jour. Acoust. Soc. Am. 75: 809-818.

Swallow, J.C. [1971] The Aries current measurement in the western North Atlantic. Philosophical Transactions Series A, 270: 451-460.

Taylor, P.T., D.J. Stanley, T. Simkin and W. Jahn [1975] Gilliss Seamount: detailed bathymetry and modification by bottom currents. Marine Geology 19: 139-157.

Taylor, P.T., C.A. Wood and T.J. O'Hearn [1980] Morphological investigations of submarine volcanism: Henderson Seamount. Geology 8: 390-395.

Tyce, R.C. [1986] Deep seafloor mapping systems-a review. MTS Jour. 20: 4-16.

Tyce, R.C., L.A. Mayer and F.N. Spiess [1980] Near-bottom seismic profile: high lateral variability, anomalous amplitudes, and estimates of attenuation. J. Acoust. Soc. Am. 68: 1391-1402.

Udintsev, G.B., G.U. Agapova, N.I. Larina and N.A. Marova [1976] Seamounts in the Pacific Ocean. In Aoki, H. and S. Iizuka, eds., Volcanoes and tectonosphere: Tokyo, Tokai University Press: 7-33.

Vogt, P.R. [1974a] Volcano spacing, fractures and thickness of the lithosphere. Earth and Planetary Science Letters 21: 235-252.

Vogt, P.R. [1974b] Volcano height and plate thickness. Earth and Planetary Science Letters 23: 337-348.

Vogt, P.R. and N.C. Smoot [1984] The Geisha Guyots: multibeam bathymetry and morphometric interpretation. Journal of Geophysical Research 89: 11,085-11,107.

Von Herzen, R.P., M.J. Cordery, R.S. Detrick and Changle Fang [1989] Heat flow and the thermal origin of hot spot swells: the Hawaiian swell revisited. Journal of Geophysical Research 94: 13,783-13,799.

Von Herzen, R.P., R.S. Detrick, S.T. Crough, D. Epp and U. Fehn [1982] Thermal origin of the Hawaiian swell: heat flow evidence and thermal models. Journal of Geophysical Research 87: 6711-6723.

Walcott, R.I. [1970] Flexure of the lithosphere at Hawaii. Tectonophysics 9: 435-446.

Walker, G.P.L. [1973] Lengths of lava flows. Philosophical Transactions of the Royal Society of London Series A, 274: 107-118.

Walker, J.A., P.J.C. Ryall, M. Zentill, I.L. Gibbson and J. Dostal [1984] The origin of compositional variation in basalts recovered by submersible drill from Mount Glooscap, Mid-Atlantic Ridge at 36°25'N. Canadian Journal of Earth Science 21: 934-948.

Warren, B.A. [1971] Antarctic deep water contribution to the world ocean. In Quam, L.O., ed., Research in the Antarctic: Washington, D.C., American Association for the Advancement of Science, publication 93: 630-643.

Watts, A.B. [1976] Gravity and bathymetry in the central Pacific Ocean. Journal of Geophysical Research 81: 1533-1553.

Watts, A.B. [1978] An analysis of isostasy in the world's oceans, 1, Hawaiian-Emperor Seamount chain. Journal of Geophysical Research 83: 5989-6004.

Watts, A.B. and J.R. Cochran [1974] Gravity anomalies and flexure of the lithosphere along the Hawaiian-Emperor seamount chain. Geophysical Journal of the Royal Astronomical Society 38: 119-141.

Watts, A.B. and N.M. Ribe [1984] On geoid heights and flexure of the lithosphere at seamounts. Journal of Geophysical Research 89: 11,152-11,170.

Watts, A.B., J.H. Bodine and N.M. Ribe [1980] Observations of flexure and the geological evolution of the Pacific Ocean basin. Nature 283: 532-537.

Winterer, E.L. and C.V. Metzler [1984] Origin and subsidence of guyots in Mid-Pacific Mountains. Journal of Geophysical Research 89: 9969-9979.

Wishner, K., L. Levin, M. Gowing and L. Mullineaux [1990] Involvement of the oxygen minimum in benthic zonation on a deep seamount. Nature 346: 57-59.